OPG's DEEP GEOLOGIC
REPOSITORY
FOR LOW & INTERMEDIATE LEVEL WASTE

Long-Term Geomechanical Stability Analysis

March 2011

Prepared by: Itasca Consulting Group, Inc.

NWMO DGR-TR-2011-17

ITASCA
Consulting Group, Inc.

OPG's DEEP GEOLOGIC
REPOSITORY
FOR LOW & INTERMEDIATE LEVEL WASTE

Long-Term Geomechanical Stability Analysis

March 2011

Prepared by: Itasca Consulting Group, Inc.

NWMO DGR-TR-2011-17

THIS PAGE HAS BEEN LEFT BLANK INTENTIONALLY

Document History

Title:	Long-Term Geomechanical Stability Analysis		
Report Number:	NWMO DGR-TR-2011-17		
Revision:	R000	**Date:**	March 2011
AECOM Canada Ltd.			
Prepared by:	B. Damjanac (Itasca Consulting Group, Inc.)		
Reviewed by:	M. Diederichs (Queen's University)		
Approved by:	R.E.J. Leech		
Nuclear Waste Management Organization			
Reviewed by:	T. Lam		
Accepted by:	M. Jensen		

THIS PAGE HAS BEEN LEFT BLANK INTENTIONALLY

EXECUTIVE SUMMARY

The Nuclear Waste Management Organization (NWMO), on behalf of Ontario Power Generation (OPG), is managing the development of a Deep Geologic Repository (DGR) for Low and Intermediate Level waste (L&ILW) at the Bruce nuclear site, located in the Municipality of Kincardine, Ontario. As part of the site characterization activities, Itasca Consulting Group, Inc. (ITASCA) has been contracted to perform geomechanical modelling analyses that evaluate the rock mass integrity and long-term stability of the proposed DGR over a timeframe of 1 Ma (1,000,000 years). The analyses include assessments of DGR cavern, pillar and shaft stability, and the evolution of damage and deformation of the surrounding rock mass in response to excavation activities and the long-term dynamic geological conditions expected at the site. This report presents the results of deformation, damage and stability analyses due to long-term rock strength degradation, gas and pore pressure changes, seismic ground shaking and glacial loading/unloading cycles.

Relevant data on material properties and in situ stress conditions used in the analyses are based primarily on the mechanical properties determined from laboratory testing of core samples retrieved from deep exploratory boreholes DGR-1, DGR-2, DGR-3 and DGR-4 drilled around the proposed repository footprint at the Bruce nuclear site. A conservative approach to modelling with laboratory-derived data required that sensitivity analyses be performed to investigate the effect of varying selected parameters on long-term repository performance. The results of these analyses also are presented.

The DGR will be excavated within Ordovician-aged argillaceous limestone of the 28 m thick Cobourg Formation. The floor of the 7 m high cavern will be at a norminal depth of 680 m below ground surface. The limestone unit is overlain by more than 200 m of Upper Ordovician shale-dominated cap rock. The shafts will transect this cap and the overlying approximately 450 m thick interlayered Silurian and Devonian carbonates and evaporites. The shafts will be sealed and backfilled at the end of the operational period.

The primary concern regarding long-term performance of the limestone cavern is its degradation over time. In particular, it is important to determine if the evolving caved region will propagate into the shale cap rock above the limestone repository. A discrete element model was used to simulate micro-cracking, time-dependent behaviour of the limestone and its potential degradation and unravelling around the emplacement caverns. Independent continuum analyses were used to investigate the sensitivity of the predictions with regard to assumptions about the long-term rock strength. The effect of potential pillar collapse after multiple glacial cycles on the stability of the shale cap rock is analyzed in a three-dimensional (3D) continuum model.

The following are important results of the long-term cavern performance analysis.

- Time-dependent strength degradation under conservative in situ stress conditions and assuming long-term limestone strength of only 31.5 MPa, 28% of unconfined compressive strength (UCS), which certainly underestimates the long-term strength, results in only 2 m deep damage to the cavern wall and 6 m depth of unstable rock in the cavern roof. If the long-term rock strength is assumed conservatively to be 45 MPa (40% UCS), no breakouts are predicted with yielding along bedding planes in the cavern roof and floor limited to a depth of approximately 2 m.
- Multiple glacial events and associated loading/unloading cycles are expected to eventually cause cavern collapse and pillar failure. However, even for a conservative assumption of

the Cobourg limestone long-term strength, the caverns are expected to stay open for at least 100,000 years. A realistic assumption of the long-term strength of Cobourg limestone at 72 MPa (65% UCS) predicts that the pillars and the caverns will not collapse after 1 Ma.

- Under the assumption of the lower bound long term strength (45 MPa), rubble that accumulates inside the caverns as a result of collapses during multiple loading/unloading cycles will eventually arrest further propagation of the caved region due to volume increase. A steady state is reached when glacial cycles cause no further expansion of the damaged or caved regions. Importantly, the models predict that the steady state is reached prior to propagation of the caving related damage into the Blue Mountain shale, the lowest unit of the shale cap rock. Therefore, all damage remains contained within the Cobourg Formation under all loading conditions.
- The effect of multiple seismic loading events on cavern stability, at both 10^{-6} and 10^{-5} probabilities of annual exceedance, is relatively small. Seismic ground shaking results in some additional unravelling of already fractured rock around cavern openings, but no new damage to the rock mass is predicted irrespective of the magnitude of the seismic events.
- Gas and pore pressure variations within the caverns do not have significant effect on damage around the caverns or the breakout depth. Under the extreme case with a maximum gas pressure of 15MPa, bedding-parallel fractures may propagate up to 5 m beyond the cavern walls. However, the gas pressures in all analyzed cases will not generate hydraulic fractures that can result in gas release into the biosphere.
- The deformation of the cap rock due to potential complete pillar collapse, assuming a lower-bound long-term strength of 45 MPa (40% UCS) for the Cobourg limestone, will cause no or insignificant damage in the cap shales, including the Blue Mountain shale. Thus, the repository-induced damage remains contained within the Cobourg limestone under all loading conditions.

The long-term stability of the shafts will not be an issue, because they will be backfilled at the end of the operational period. The primary concern for the shaft analysis is the time and space evolution of rock permeability along the shaft, due to long-term deformation and damage to the rock mass. Understanding permeability variation is critical for evaluating the potential for transport of gases and fluids between the repository and the bio-sphere. The shaft stability and damage to the surrounding rock mass were analyzed using a 3D continuum model for different long-term loading conditions for critical shaft seals.

The following are the important results of the shaft analysis.

- The depth of failure for all load combinations after 1 Ma exceeds (by maximum of 28%) the shaft radius only in the case of the very weak Cabot Head Formation near the base of the Silurian. Elsewhere along the shaft, the maximum depth of failure is typically in the range of 60% to 70% of the radius or less.
- Time-dependent strength degradation typically causes an increase of 25% to 50% in damage zone radius around the shaft seals.
- Seismic shaking and glacial loading are practically inconsequential for damage zone evolution and shaft performance over time.

The single most important parameter used in these numerical analyses is the long-term strength of the rock mass. Several model iterations are used to bound the range of possible outcomes, because one cannot directly measure the rock mass strength around a cavern over 1 Ma. As mentioned above, if the projected long-term rock strength is 65% UCS, a value commonly used for brittle materials, essentially no damage to the DGR and to the overlying shale cap rocks is predicted regardless of the loading conditions. If a conservative estimate of 40% UCS is employed for long-term rock strength (i.e., the onset of cracking in brittle materials), the DGR caverns are expected to collapse after approximately 100,000 years. In all cases, the overlying shale cap rocks will remain intact regardless of the imposed loading conditions. The EDZ, with potentially increased permeability, is predicted to be typically 70% or less of the shaft radius along almost the entire shaft length.

ACKNOWLEDGEMENTS

This report encompasses the work of numerous individuals within Itasca Consulting Group Inc. and in particular the contributions of Branko Damjanac and Andrew Corkum are acknowledged for their significant contribution. Participants from other organizations have played an important role in directing and reviewing this report. We are particularly grateful to the Geomechanics Peer Review committee comprised of Mark Diederichs (Queens University), Tom Lam (NWMO), Dougal McCreath (Laurentian University) and Derek Martin (University of Alberta) for their guidance and expertise in numerical analysis and modelling.

Finally, we would like to thank Robert Leech and his team at AECOM for their logistical and technical support.

TABLE OF CONTENTS

Page

APPENDIX A: FLAC3D RESULTS FOR BULKHEAD B1

APPENDIX B: SUPPLEMENTAL FLAC3D RESULTS FOR CONCRETE BULKHEAD IN BLUE MOUNTAIN SHALE

APPENDIX C: FLAC3D RESULTS FOR ASPHALT SEAL S2

APPENDIX D: SUPPLEMENTAL FLAC3D RESULTS FOR BULKHEAD IN QUEENSTON AND MANITOULIN FORMATIONS

APPENDIX E: SUPPLEMENTAL FLAC3D RESULTS FOR WATERSTOP BULKHEAD

APPENDIX F: SUPPLEMENTAL FLAC3D RESULTS FOR BULKHEAD IN SALINA C FORMATION

LIST OF TABLES

LIST OF FIGURES

THIS PAGE HAS BEEN LEFT BLANK INTENTIONALLY

1. INTRODUCTION

1.1 Background

Nuclear Waste Management Organization (NWMO), on behalf of Ontario Power Generation (OPG), is managing the development of a Deep Geologic Repository (DGR) for Low and Intermediate Level Waste (L&ILW) at the Bruce nuclear site, located in the municipality of Kincardine. This site-specific long-term geomechanical stability analysis study is a part of the DGR site characterization activities. This study aims to evaluate the rock mass integrity and long-term stability of the proposed DGR over a timeframe of 1 Ma (1,000,000 years). The analyses include assessments of DGR cavern, pillar and shaft stability, and the evolution of damage and deformation of the surrounding rock mass in response to excavation activities and the long-term dynamic geological conditions expected at the site.

The present concept for the proposed deep geologic repository includes two shafts that extend into the Sherman Fall and Kirkfield formations. Currently, it is expected that the host rock will be the low permeability limestone of the Cobourg Formation at this depth.

The site-specific geomechanical modelling studies will be used to evaluate whether the proposed layout and geometry satisfy stability and safety requirements, given the geological conditions at the site. The analyses were focused primarily on the emplacement panels and the caverns, which represent the most extensive development in the repository, and on the shafts, which represent potential pathways for release of radionuclides into the bio-sphere. The effects of different loading conditions expected during a timeframe of 1 Ma on repository performance were analyzed, including the overall stability of the caverns and the shaft, damage and deformation of the surrounding rock mass and evolution of excavation damaged zone (EDZ). The analysis utilizes relevant data on material properties and in situ stress conditions, mostly based on laboratory tests carried out on the samples taken from the site boreholes. Considering the uncertainty of some of the data in geomechanical modelling, sensitivity analyses with respect to selected parameters were conducted to investigate the effect of their variability, within reasonable ranges, on repository performance.

1.2 Project and Modelling Approach Overview

The DGR would consist of surface infrastructure for the receipt of waste packages and transfer underground via a 6.5 m finished diameter main shaft to the repository horizon at a nominal 680 metres below ground surface (mBGS) (Figure 1.1). The shaft collars have been set at a nominal 186 m above sea level. A ventilation supply system, including heaters (for winter operations), will supply air at a controlled range of temperatures to ensure that freezing does not occur in the downcast shaft, underground conditions are suitable for workers, and atmosphere is maintained in a reasonably steady and dry state to limit corrosion of structures and waste packages. The 5.0 m finished diameter ventilation shaft will be an upcast shaft with main exhaust fans on surface to pull the spent air out of the repository.

The reference capacity of the repository is nominally 200,000 m^3 of “as-disposed” waste, and will be developed fully during initial construction, so that once waste emplacement operations commence, no mining activities, other than inspection and maintenance of rock support, concrete linings, roadbeds and ventilation systems, will need to occur.

The underground layout of the repository shown in Figure 1.2, has the two vertical shafts as an islanded arrangement with a shaft services area, in which offices, a workshop, wash bay, refuge stations, lunch rooms and geotechnical laboratory are provided. A main access tunnel is driven from the main shaft station to the east, passing the ventilation shaft and then proceeding towards the emplacement room panels. The overall underground arrangement enables all underground infrastructures to be kept in close proximity to the shaft, while keeping the emplacement areas away from normally occupied and high-activity areas.

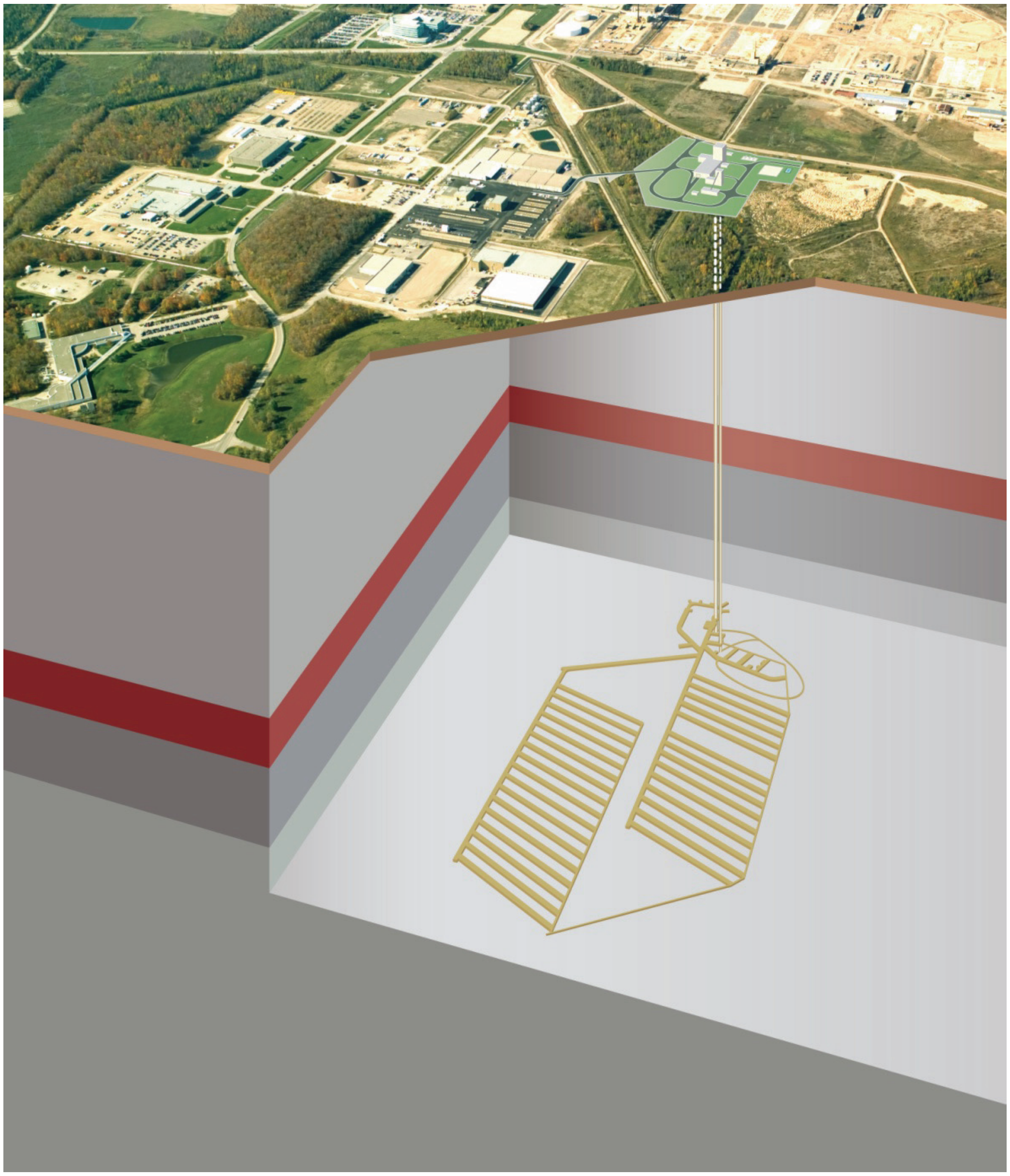

Note: Figure is from OPG (2011)

Figure 1.1: Schematic View of the DGR

All the emplacement rooms are aligned with the assumed direction of the major principle horizontal stresses of the rock mass in the Cobourg Formation (i.e., east-north-east) to maximize roof stability in the emplacement rooms during the period in which the repository could remain open. Any reference to the Cobourg limestone or Formation in this report includes the calcareous shale and limestone of the Collingwood member and the lower Cobourg limestone member, unless otherwise noted. There will be two panels of emplacement rooms. The main access tunnel running from the main shaft continues straight into the “Panel 1” access tunnel, while a branch tunnel to the south leads to the “Panel 2” access tunnel.

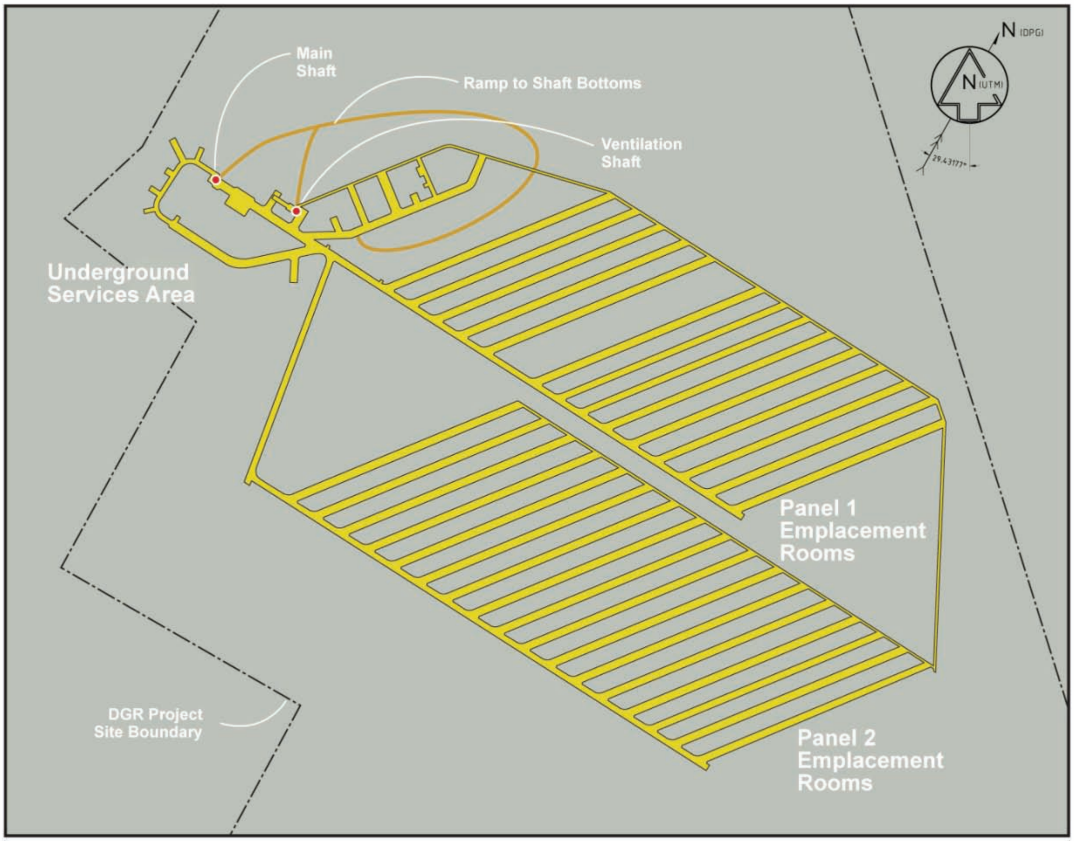

Note: Figure modified from OPG (2011)

Figure 1.2: DGR Underground Layout

The long-term stability analyses documented herein were focused primarily on the emplacement panels and caverns, and on the shafts. The effects of different loading conditions expected during a timeframe of 1 Ma on repository performance were analyzed, including the overall stability of the caverns and the shaft, damage and deformation of the surrounding rock mass and evolution of EDZ. The following is the list (also illustrated in Figure 1.3) of the loads and conditions relevant for stability and performance of the repository, which were considered as an individual event or in combination with other scenarios in the analysis.

- In situ stresses. Rock mass (the Cobourg Formation) is at significant in situ stress at the repository depth. Excavation of the repository will cause perturbation to the in situ stress state and stress concentrations around the excavations that will cause deformation and, potentially, damage and failure of the rock mass.

- Time-dependent strength degradation of the stressed rock mass. There is evidence that strength of the rocks subjected to certain stress levels and exposed to atmosphere gradually degrades with time. Time-dependent strength degradation of the rock mass can cause time-dependent evolution of damage and failure of the rock mass.
- Water and gas pore pressure and pressure inside the caverns. The rock mass at the DGR is saturated with water heads roughly corresponding to the water level in Lake Huron. Pore pressures affect deformation and damage of rocks. During operation of the repository, the gases generated inside the emplacement rooms as a result of waste degradation will impose the pressure on the cavern wall, and if sufficiently large, may even cause hydraulic fracturing of the rock and escape of gas from the caverns into the biosphere.
- Glacial loading. The ice sheet developed over southern Ontario during previous glacial episodes. It is expected that the repository will be subjected to multiple glacial events during 1 Ma. The ice sheet that can be up to 3 km thick will impose additional loading on the repository, and will cause additional deformation, damage and potential failure of the caverns and pillars.
- Seismic shaking. Over the period of 1 Ma the repository will be subjected to multiple seismic events, some with a very small probability of recurrence and relatively strong intensity.

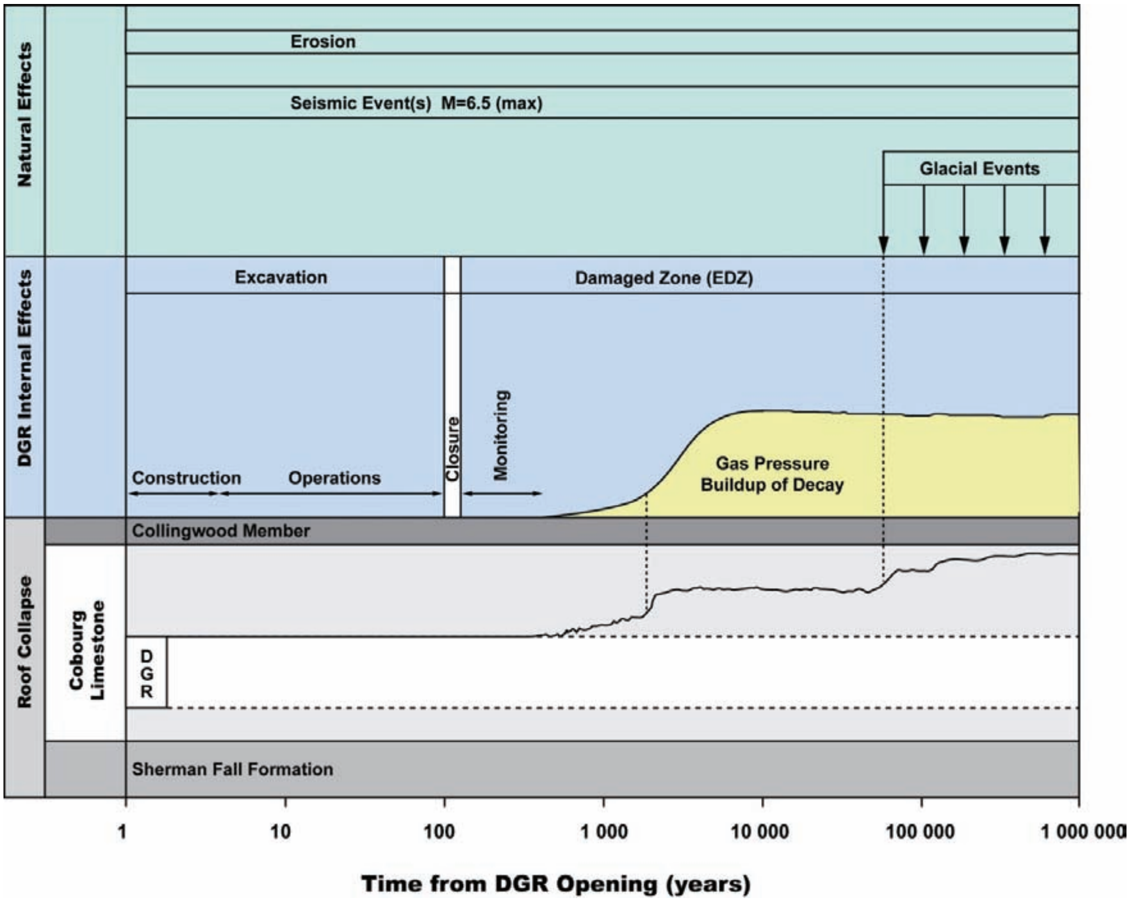

Figure 1.3: Evolution of the Repository with Time

The effect of probable and conservative combinations of loads and states on performance and stability of the repository are analyzed numerically. The finite-difference numerical codes allow explicit representation of the analyzed geometry and loads. Two different approaches were used to represent mechanical behaviour of the rock. In the cavern stability analysis, the rock mass typically is represented as an assembly of polygonal (Voronoi) blocks, which is calibrated to mechanical behaviour measured (observed) in laboratories. The purpose and advantage of this approach is simulation of damage, fracturing and potential disintegration of the rock mass (i.e., rockfall and collapse). The other continuum approach is used mainly in cases in which disintegration of the rock mass is not expected.

The analyses were conducted on different length scales. Stability of the caverns and the pillars between the caverns is analyzed in the pillar (cavern) scale models, which include a single pillar and cavern. However, consequences of the potential pillar collapse throughout the repository on stability of the overlying cap rock are analyzed in the panel (repository) scale models, which include the entire repository.

1.3 Report Outline

The following is the outline of this report.

- Chapter 2 lists software used in the analyses and discusses expectations and limitations of the numerical modelling.
- The results of the site geomechanical characterization are summarized and the model parameters for the cavern and shaft analyses are derived in Chapter 3.
- Chapter 4 provides discussion of different loading scenarios and conditions that can affect long-term performance of the repository and their representation in the analyses.
- Chapter 5 presents the results of the long-term cavern stability analysis considering different loading scenario occurring concurrently. These are pillar-scale analyses.
- The panel-scale parametric analysis of the effect of the long-term rock strength on stability of the repository during multiple glacial episodes and the analysis of potential pillar collapse on integrity of the cap shales is documented in Chapter 6.
- Chapter 7 presents the results of the long-term shaft analysis considering different loading scenarios occurring concurrently. Multiple bulkheads and sections along the shaft are analyzed and discussed in this chapter. Evolution of EDZ along the shaft is predicted.
- Chapter 8 provides overall conclusions on the long-term stability analyses.

Detailed plots of results of number of shaft seals analyses are provided in Appendices A through F.

2. NUMERICAL MODELLING EXPECTATIONS AND LIMITATIONS

The analyses carried out for this study make extensive use of numerical modelling software as the basis for design recommendations. The numerical finite-difference method codes FLAC3D Versions 3.10.474 32-bit (ITASCA 2005) and V.4.00.35 64-bit (ITASCA 2009), FLAC Version 6.00.393 (ITASCA 2008) and UDEC Version 4.01.203 (ITASCA 2006) were used for the analyses to derive most of the results discussed in this report. Although these modelling techniques are well established in engineering research and practice and capable of providing valuable insight into geomechanics problems, it is acknowledged that they entail a number of simplifying assumptions with the prime objective of capturing the dominant mode of behaviour, with respect to the long-term development of a zone of damage/yielding around the caverns and the shaft. The critical assumptions with respect to the models are described where appropriate throughout this report.

Simulation of the cavern and shaft excavations under the in situ conditions can be carried out only in an approximate manner. However, because the model reflects the physical information from a well-conceived site characterization program, it can be used in the process of performance assessment in a general sense (i.e., suggesting the extent of damaged zone around the cavern and shaft excavations and backfill/seals). It is in this context that the current model analyses were conducted and should be evaluated. Considering that the objective of the analyses is to predict the repository performance for 1 Ma, which includes considerable uncertainty, the ranges of input parameters were analyzed in order to investigate sensitivity of the predictions and provide bounds to expected responses. Whenever possible, the model outputs are judged by comparison with observations. Although sensitivity studies provide perspective and can be a useful tool in modelling geotechnical conditions, the need for such perspective must be balanced with the modelling objective, site-condition uncertainty and the amount of conservatism included in the model in general. For this project, relatively conservative assumptions regarding geotechnical conditions were made, and sensitivity studies focused on the long-term loading conditions (e.g., seismic loading, pore pressure).

3. GEOMECHANICAL DATA AND MATERIAL PARAMETERS

The geology of the Bruce nuclear site, with stratigraphy illustrated in Figure 3.1, consists predominantly of the near horizontally layered sequence of dolostone, shale and limestone. The repository is proposed to be located at a nominal 680 mBGS, in the competent, low porosity limestone of the Cobourg Formation. The stratigraphy was determined based on six DGR site investigation boreholes (DGR-1 to DGR-6) (INTERA[1] 2011). The mechanical properties used for long-term stability analyses were based mainly on laboratory testing of rock samples taken from the investigation boreholes (Gorski et al. 2009a, 2009b, 2010a, 2010b).

The laboratory testing has been carried out on a number of samples from the representative units from the geological profile. However, the largest number of tests was carried out on the samples from the Cobourg Formation, in which the repository will be located. The tests include (Gorski et al. 2009a, 2009b, 2010a, 2010b): 1) P- and S-wave velocity measurements, 2) uniaxial compressive strength (UCS) and triaxial compressive strength testing, 3) acoustic emission monitoring during the UCS test, which was used to determine crack initiation, CI, and crack damage, CD, thresholds, 4) Brazilian tensile strength test, 5) bedding plane direct shear strength tests, 6) long-term strength degradation testing and 7) cross anisotropic deformation tests.

A summary of the relevant testing data in the units of interest (i.e., the units that are representative or can significantly affect performance of the emplacement caverns and the shafts) is presented in this chapter. The testing data are interpreted to derive input parameters for the models, particularly with respect to the scale of interest compared to the scale of the tested samples. Considering different models used, and different geological units of interest for the pillar-scale cavern analyses and the shaft and panel-scale analyses, the material input parameters are discussed separately. The material input data for the pillar-scale cavern analyses are discussed in Section 3.1; the material properties for the shaft and panel-scale analyses are discussed in Section 3.2.

The properties used for the cavern and shaft analyses were derived from the test data available at time the analyses were conducted. The references to all source data and the derivation of the properties as used in the analyses are provided in this report. In some instances, the properties used in the analyses are different from those documented in the geosynthesis report. There are three reasons for those differences, including: 1) the additional data that were used in the geosynthesis report were available after the analyses were completed, 2) specific assumptions used in the analyses (e.g., consideration of the weak Sherman Fall as a separate unit) and 3) the need to highlight kinematic failure mechanisms in the model by using extreme values (such as unreasonably low strength). It is explained in the text where the properties are discussed, that the differences are either insignificant or deliberate (as in 3), so as to provide conservative results from the analysis.

3.1 Geological Units and Their Representation in Pillar-Scale Cavern Analysis

Four different geological units listed in the sequence from the bottom to the top, are included in the numerical model of the pillar-scale cavern stability, including: 1) Sherman Fall limestone, 2) the interface region between the Cobourg and Sherman Fall limestones, referred to in this report as the weak Sherman Fall limestone, 3) Cobourg limestone and 4) Blue Mountain shale.

---

[1] Currently known as Geofirma Engineering Ltd.

The Sherman Fall limestone and the Blue Mountain shale are approximated as continuum Mohr-Coulomb materials with equivalent rock-mass material properties. Continuum approximation for these units is considered adequate, because they are relatively far from the emplacement caverns and are expected to behave elastically over 1 Ma. In the region around the caverns, where significant inelastic deformation, including damage, fracturing and formation of loose blocks, is expected, the Cobourg limestone and weak Sherman Fall limestone are represented using the Voronoi block approach (Section 3.1.3 and Damjanac et al. 2007). Because the bedding planes in the Cobourg Limestone and Sherman Fall limestone are represented explicitly at 0.75 m spacing, the Voronoi block assembly represents the intact rock between the bedding planes.

3.1.1 Results of Geomechanical Tests

3.1.1.1 Intact Rock Testing

The average density of the samples taken from DGR-1, DGR-2, DGR-3 and DGR-4 (measured on 144 samples (Gorski et al. 2009a, Tables A-1 and A-2; Gorski et al. 2010a, Tables A-1 and A-2) is 2,670 kg/m^3 with standard deviation of 62 kg/m^3. Conservatively, a rock mass density of 2,700 kg/m^3 was assumed for all units throughout the profile.

The strength and stiffness of the rock mass units in the model are determined from the unconfined strength test results obtained from DGR-2 (Gorski et al. 2009a, Table A-6), DGR-3 (Gorski et al. 2010a, Table A-5) and DGR-4 (Gorski et al. 2010a, Table A-6). Table A-5 in Gorski et al. (2009a) contains the results of the tests on samples taken from DGR-1. Those samples are not relevant for cavern stability, because they are taken at considerable lower depth above from the emplacement caverns.

The tests were carried out on the small-scale samples (75 mm in diameter) taken from different depths. The properties of different units obtained by averaging the representative test results are listed in Table 3.1. The largest number of samples is from the Cobourg limestone, because it is the unit where the repository will be located.

Table 3.1: Average Unconfined Strength Test Results for the Model Units

	UCS[1] (MPa)	E (GPa)	ν	CD[2] (MPa)	CI[3] (MPa)	CD/UCS	CI/UCS	Number of Tests
Blue Mountain Shale	21.7	5.18	0.103	18.10	8.21	0.87	0.38	3
Cobourg Limestone	111.3	36.72	0.31	93.99	44.97	0.84	0.41	50
weak Sherman Fall Limestone	35.8	10.75	0.083	22.21	8.03	0.65	0.24	2
Sherman Fall Limestone	55.6	26.61	0.31	43.81	22.51	0.71	0.39	6

Notes: 1. Unconfined compressive strength (UCS); 2. CD is the crack damage stress; 3. CI is the crack initiation stress.

In addition to unconfined tests, 6 triaxial tests were carried on the Cobourg limestone samples from DGR-3 and eight tests on Cobourg limestone samples from DGR-4 (Gorski et al. 2010a, Tables 7 and 8). The test results in $\sigma_1 - \sigma_3$ space with linear (Mohr-Coulomb) fit are shown in Figure 3.2. The Mohr-Coulomb fit indicates an unconfined compressive strength (UCS) of 113.4 MPa and a friction angle of 41°.

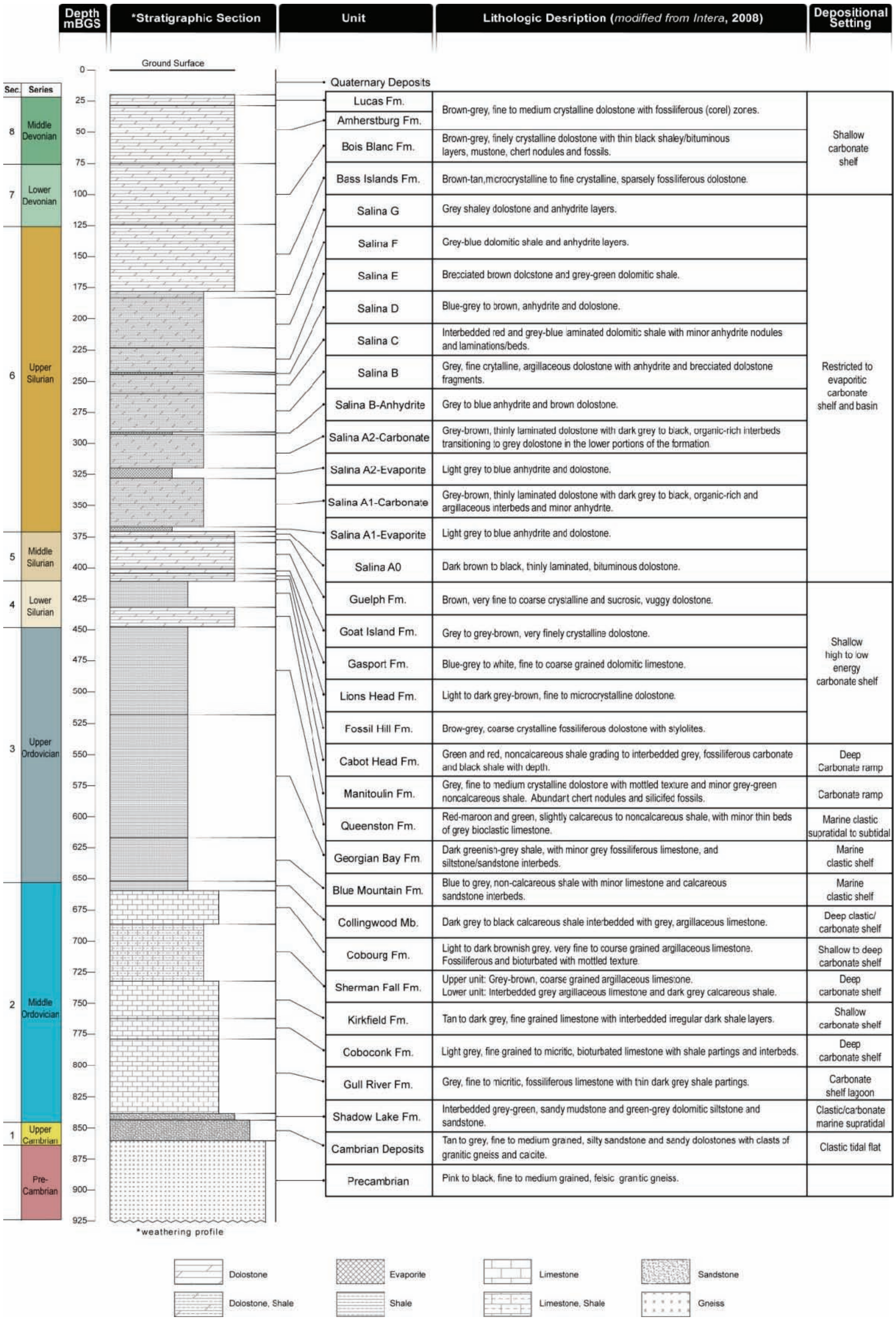

Unit	Lithologic Desription (*modified from Intera*, 2008)	Depositional Setting
Quaternary Deposits		
Lucas Fm. Amherstburg Fm.	Brown-grey, fine to medium crystalline dolostone with fossiliferous (corel) zones.	Shallow carbonate shelf
Bois Blanc Fm.	Brown-grey, finely crystalline dolostone with thin black shaley/bituminous layers, mustone, chert nodules and fossils.	
Bass Islands Fm.	Brown-tan,microcrystalline to fine crystalline, sparsely fossiliferous dolostone.	
Salina G	Grey shaley dolostone and anhydrite layers.	Restricted to evaporitic carbonate shelf and basin
Salina F	Grey-blue dolomitic shale and anhydrite layers.	
Salina E	Brecciated brown dolostone and grey-green dolomitic shale.	
Salina D	Blue-grey to brown, anhydrite and dolostone.	
Salina C	Interbedded red and grey-blue laminated dolomitic shale with minor anhydrite nodules and laminations/beds.	
Salina B	Grey, fine crytalline, argillaceous dolostone with anhydrite and brecciated dolostone fragments.	
Salina B-Anhydrite	Grey to blue anhydrite and brown dolostone.	
Salina A2-Carbonate	Grey-brown, thinly laminated dolostone with dark grey to black, organic-rich interbeds transitioning to grey dolostone in the lower portions of the formation.	
Salina A2-Evaporite	Light grey to blue anhydrite and dolostone.	
Salina A1-Carbonate	Grey-brown, thinly laminated dolostone with dark grey to black, organic-rich and argillaceous interbeds and minor anhydrite.	
Salina A1-Evaporite	Light grey to blue anhydrite and dolostone.	
Salina A0	Dark brown to black, thinly laminated, bituminous dolostone.	
Guelph Fm.	Brown, very fine to coarse crystalline and sucrosic, vuggy dolostone.	Shallow high to low energy carbonate shelf
Goat Island Fm.	Grey to grey-brown, very finely crystalline dolostone.	
Gasport Fm.	Blue-grey to white, fine to coarse grained dolomitic limestone.	
Lions Head Fm.	Light to dark grey-brown, fine to microcrystalline dolostone.	
Fossil Hill Fm.	Brow-grey, coarse crystalline fossiliferous dolostone with stylolites.	
Cabot Head Fm.	Green and red, noncalcareous shale grading to interbedded grey, fossiliferous carbonate and black shale with depth.	Deep Carbonate ramp
Manitoulin Fm.	Grey, fine to medium crystalline dolostone with mottled texture and minor grey-green noncalcareous shale. Abundant chert nodules and silicifed fossils.	Carbonate ramp
Queenston Fm.	Red-maroon and green, slightly calcareous to noncalcareous shale, with minor thin beds of grey bioclastic limestone.	Marine clastic supratidal to subtidal
Georgian Bay Fm.	Dark greenish-grey shale, with minor grey fossiliferous limestone, and siltstone/sandstone interbeds.	Marine clastic shelf
Blue Mountain Fm.	Blue to grey, non-calcareous shale with minor limestone and calcareous sandstone interbeds.	Marine clastic shelf
Collingwood Mb.	Dark grey to black calcareous shale interbedded with grey, argillaceous limestone.	Deep clastic/ carbonate shelf
Cobourg Fm.	Light to dark brownish grey, very fine to course grained argillaceous limestone. Fossiliferous and bioturbated with mottled texture.	Shallow to deep carbonate shelf
Sherman Fall Fm.	Upper unit: Grey-brown, coarse grained argillaceous limestone. Lower unit: Interbedded grey argillaceous limestone and dark grey calcareous shale.	Deep carbonate shelf
Kirkfield Fm.	Tan to dark grey, fine grained limestone with interbedded irregular dark shale layers.	Shallow carbonate shelf
Coboconk Fm.	Light grey, fine grained to micritic, bioturbated limestone with shale partings and interbeds.	Deep carbonate shelf
Gull River Fm.	Grey, fine to micritic, fossiliferous limestone with thin dark grey shale partings.	Carbonate shelf lagoon
Shadow Lake Fm.	Interbedded grey-green, sandy mudstone and green-grey dolomitic siltstone and sandstone.	Clastic/carbonate marine supratidal
Cambrian Deposits	Tan to grey, fine to medium grained, silty sandstone and sandy dolostones with clasts of granitic gneiss and calcite.	Clastic tidal flat
Precambrian	Pink to black, fine to medium grained, felsic granitic gneiss.	

Note: Figure is from NWMO and AECOM (2011).

Figure 3.1: Geological Stratigraphy from DGR Site Investigation Boreholes

THIS PAGE HAS BEEN LEFT BLANK INTENTIONALLY

The Cobourg intact strength in the numerical analyses was set to the lower UCS value of 111.3 MPa (from averaging the UCS test results in Table 3.1), and the friction angle is 41°.

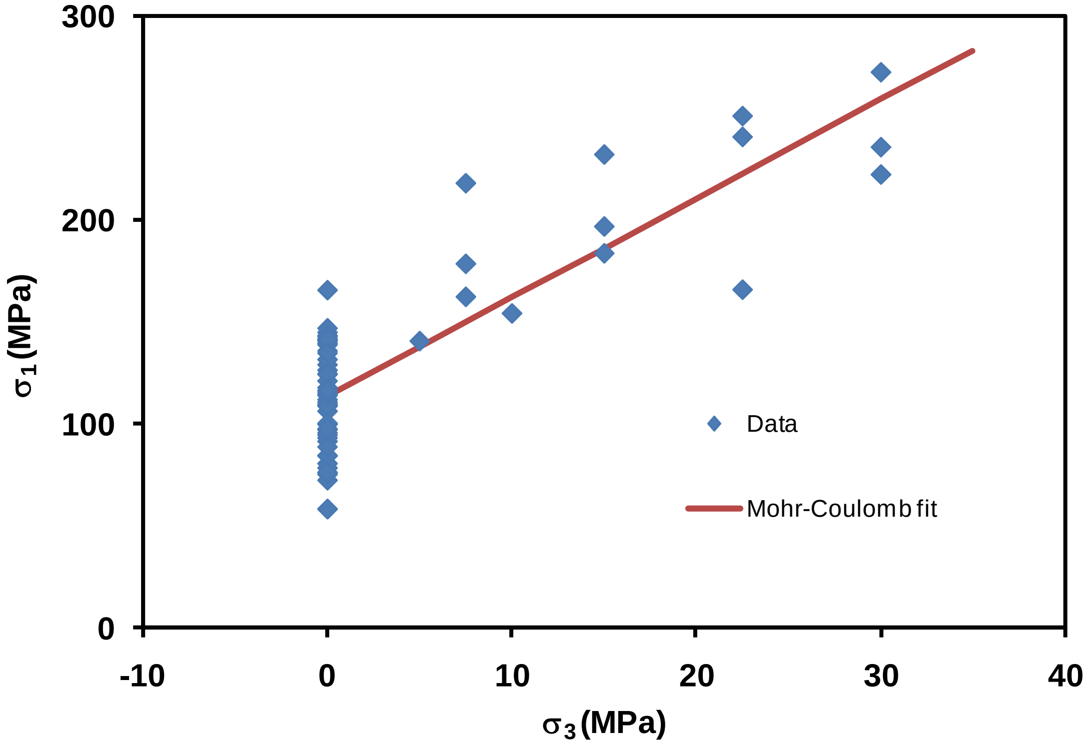

Figure 3.2: Uniaxial and Triaxial Test Data for Cobourg Limestone and Mohr-Coulomb Fit

3.1.1.2 Bedding-Plane Testing

Direct shear tests were conducted on specimens containing the shaly bedding planes. The mechanical behaviour of shaly bedding planes in the Cobourg Formation is of particular interest in this analysis, because the bedding planes in the Cobourg Formation are represented explicitly in the model as weak planes. There were 13 direct shear tests on the bedding planes in Cobourg Formation on samples taken from DGR-2, DGR-3 and DGR-4 (Gorski et al. 2010a, Table 11 and Appendix F). The direct shear tests typically were carried out at four different confining stresses for each sample. The test for the initial confinement measures the intact shear strength of the bedding plane. The subsequent tests on the same specimen and increasing confining stresses measure the residual strength of a bedding plane, because the bedding plane was sheared in the initial test. Consequently, the tests provide only one point on the peak shear-strength line, which is insufficient to estimate both peak cohesion and friction angle. However, the residual friction angle can be determined from the results at increased confining stresses after the sample has been sheared initially. The friction angle is determined by fitting a straight line through the experimental data and the origin in the $\tau-\sigma_n$ plot. Such a fit implies that the residual cohesion of the bedding planes is zero. The examples of the test data and linear fits to that data are shown in Figure 3.3. Although the best fit results in non-zero cohesion, the fit with fixed intercept at zero, which is the physically expected result, represents the data very well.

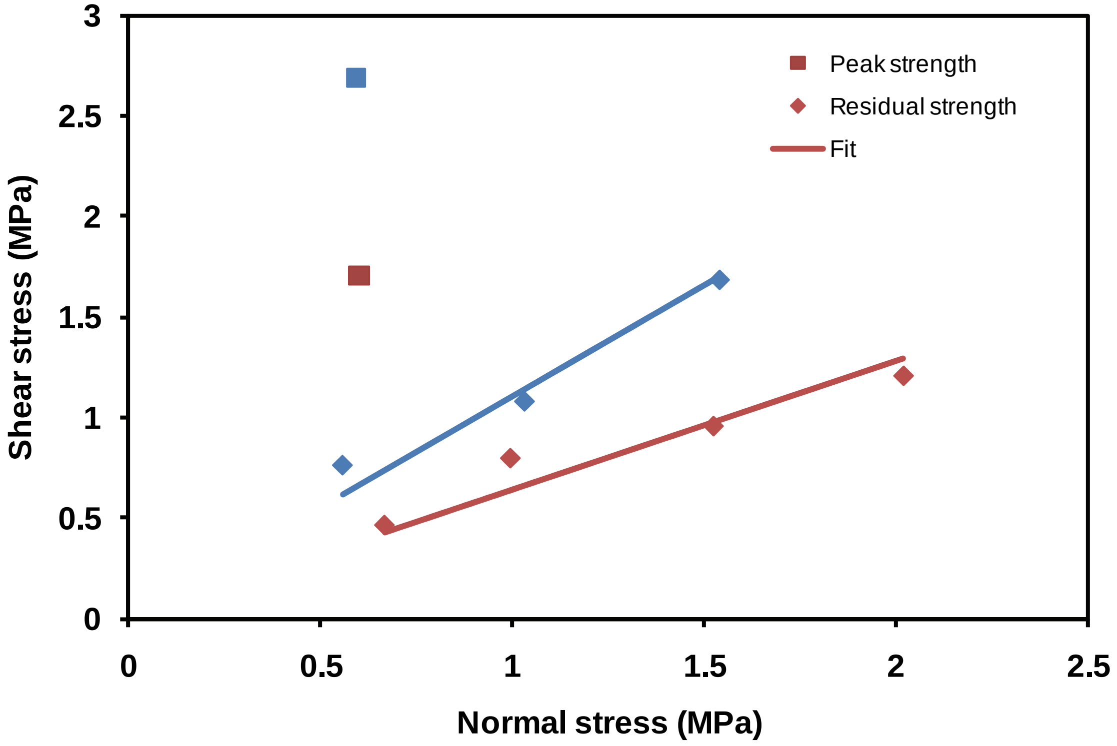

Figure 3.3: Direct Shear Test Data and Linear Fit Though the Origin for Samples DGR-3 667.98 (red) and DGR-4 683.72 (blue)

The average residual friction coefficient between the 13 direct shear tests is 0.79, which corresponds to a friction angle of 38.3°. If it is assumed that shearing of the bedding plane affects its cohesive strength only (i.e., because the joint roughness in bedding planes is typically low, it can be assumed that the peak and residual friction angles are the same), the intact cohesion, c_p , can be determined from the Coulomb slip law and experimentally measured relations between the peak shear strength, τ_p , and the confining stress, σ_n :

$$c_p = \tau_p - \sigma_n \tan\phi \qquad (1)$$

The average cohesion calculated from 13 tests of peak shear strength of the bedding planes is 3.31 MPa. If the bedding-plane tensile strength is taken as 1/5 of cohesion, it is 0.66 MPa. The selected bedding-plane strength data are listed in Table 3.2.

Table 3.2: Bedding Plane Strength Data

Peak Cohesion (MPa)	Peak Friction Angle (°)	Residual Cohesion (MPa)	Residual Friction Angle (°)	Tensile Strength (MPa)
3.31	38.3	0	38.3	0.66

3.1.1.3 Bedding Plane Stiffness

The bedding-plane normal stiffness is calculated from the condition that the stiffness normal to the bedding planes of the Cobourg limestone rock mass, E_m , is 30 GPa (as determined based on the geological strength index, GSI, of 75 and using empirical relation from Hoek and Deiderichs 2006). In the case of layered media, with uniform bedding-plane spacing d , the rock mass stiffness can be expressed in terms of intact rock stiffness, E, joint normal stiffness, k_n , as follows:

$$\frac{1}{E_m} = \frac{1}{E} + \frac{1}{k_n d} \tag{2}$$

or,

$$E_m = \frac{E k_n d}{k_n d + E} \tag{3}$$

From the previous expression, the bedding plane normal stiffness is:

$$k_n = \frac{E_m}{d\left(1 - \frac{E_m}{E}\right)} \tag{4}$$

For E_m=30 GPa, the intact Cobourg Young's modulus, E=36.72 GPa (Table 3.1), and an assumed bedding-plane spacing of 0.75 m, the joint normal stiffness is calculated to be k_n=219 GPa/m. Barton (2007, Section 16.4 therein) states that the ratio of static joint normal-to-shear stiffness for most of the tested cases is in the range between 11 and 15. For the cavern stability analysis, the joint shear stiffness, k_s , is assumed to be 1/15 of the joint normal stiffness.

3.1.2 Material Models and Parameters

The Blue Mountain shale and Sherman Fall limestone are represented in the pillar-scale cavern analyses as Mohr-Coulomb continuum materials. The mechanical properties used in this constitutive model are two rock-mass elastic properties (e.g., Young's modulus and Poisson's ratio) and rock-mass strength properties (e.g., cohesion, friction angle, tensile strength). The mechanical properties obtained from laboratory tests on small samples, discussed in Section 3.1.1.1, have to be reduced to be representative of the rock-mass mechanical behaviour to account for scale effects and the effect of rock mass jointing. A standard approach in rock engineering to calculate rock mass properties uses the GSI and Hoek-Brown failure criterion. The methodology implemented in the software program RocLab, Version 1.0 (ROCSCIENCE 2007), is used here to calculate rock-mass mechanical properties for the Blue Mountain shale and Sherman Fall limestone. The GSI, based on borehole data, was estimated for the Blue Mountain shale and the Sherman Fall limestone to be 70 and 65, respectively. The results of the rock-mass strength and deformability analysis are shown in Figure 3.4 and Figure 3.5. Values for m_i were selected as typical average values recommended for shale and limestone in RocLab (ROCSCIENCE 2007).

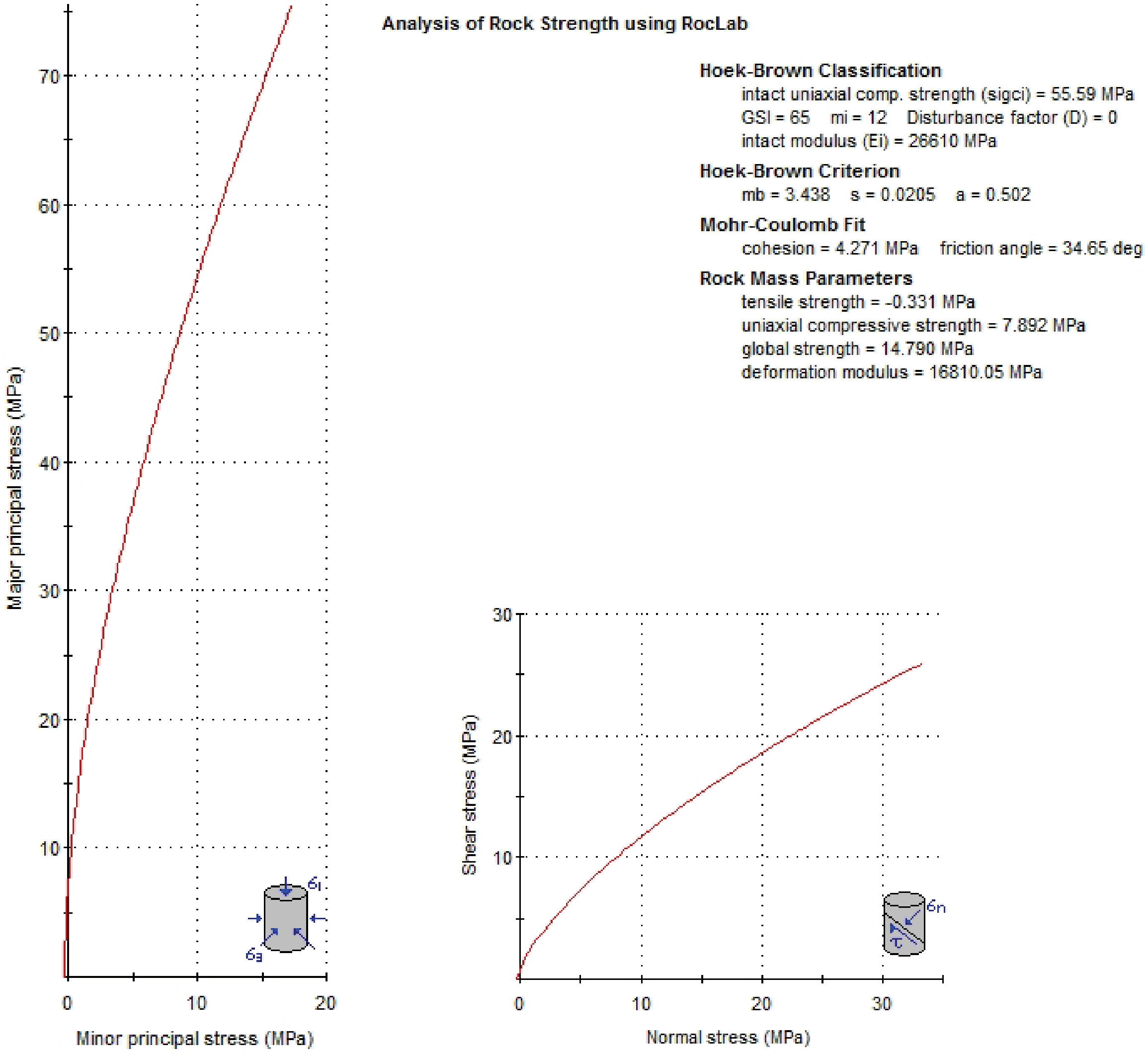

Analysis of Rock Strength using RocLab

Hoek-Brown Classification
intact uniaxial comp. strength (sigci) = 55.59 MPa
GSI = 65 mi = 12 Disturbance factor (D) = 0
intact modulus (Ei) = 26610 MPa

Hoek-Brown Criterion
mb = 3.438 s = 0.0205 a = 0.502

Mohr-Coulomb Fit
cohesion = 4.271 MPa friction angle = 34.65 deg

Rock Mass Parameters
tensile strength = -0.331 MPa
uniaxial compressive strength = 7.892 MPa
global strength = 14.790 MPa
deformation modulus = 16810.05 MPa

Figure 3.4: Rock Mass Strength for the Sherman Fall Limestone

The poorly defined bedding planes in the generally massive Cobourg limestone are represented explicitly in the model. This also applies to the weak Sherman Fall units. Therefore, and because there are no other large-scale joint sets, the mechanical properties for the Cobourg and weak Sherman Fall limestone, listed in Table 3.1, do not need to be reduced to account for the effect of rock mass jointing. However, because of their importance for cavern stability, the strengths of these two units were reduced relative to the averages by one standard deviation approximately, to account for uncertainty in the data. Thus, the UCS in the analyses was reduced to 93.5 MPa and 30.1 MPa for the Cobourg and the weak Sherman Fall limestones, respectively.

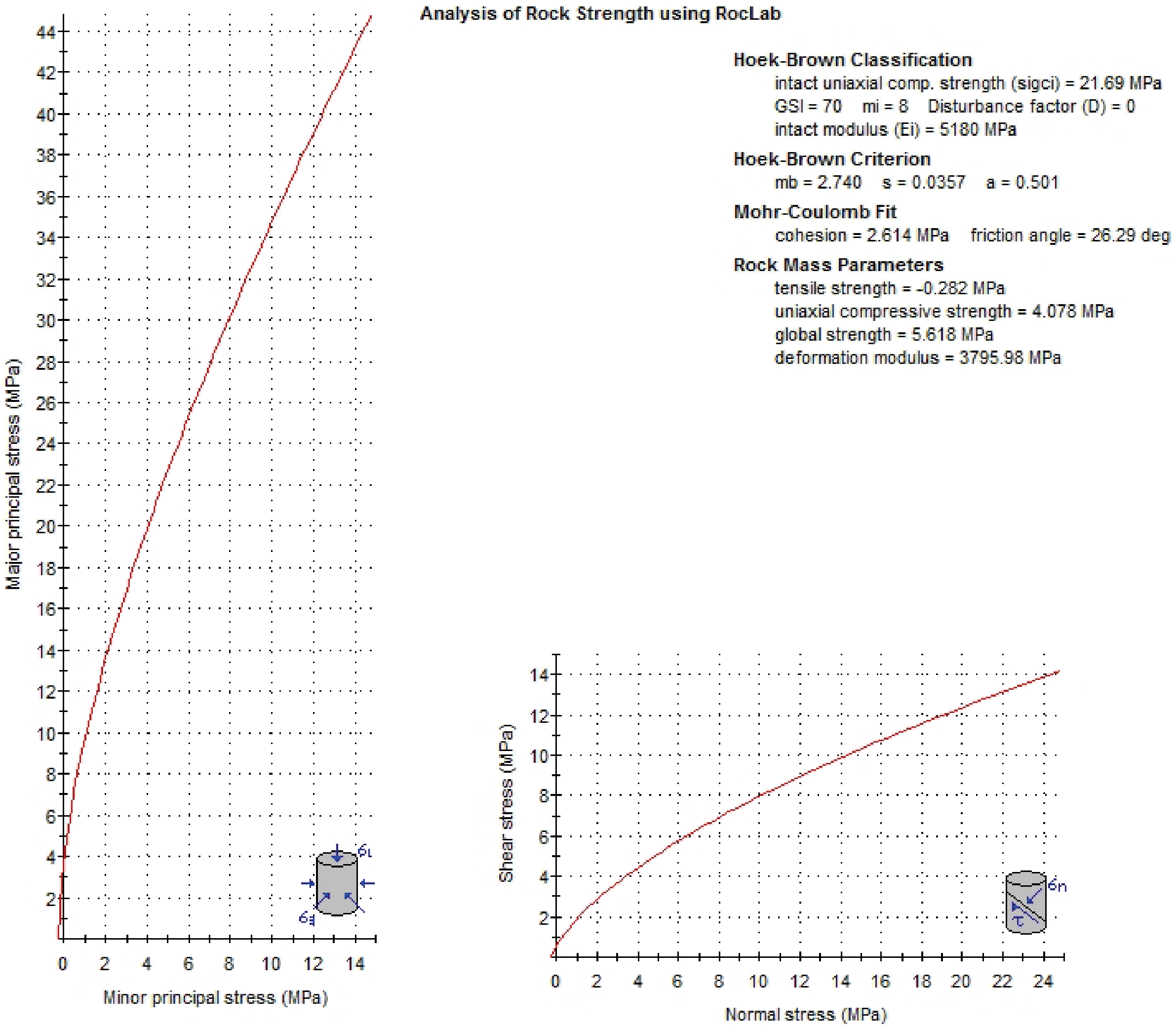

Analysis of Rock Strength using RocLab

Hoek-Brown Classification
intact uniaxial comp. strength (sigci) = 21.69 MPa
GSI = 70 mi = 8 Disturbance factor (D) = 0
intact modulus (Ei) = 5180 MPa

Hoek-Brown Criterion
mb = 2.740 s = 0.0357 a = 0.501

Mohr-Coulomb Fit
cohesion = 2.614 MPa friction angle = 26.29 deg

Rock Mass Parameters
tensile strength = -0.282 MPa
uniaxial compressive strength = 4.078 MPa
global strength = 5.618 MPa
deformation modulus = 3795.98 MPa

Figure 3.5: Rock Mass Strength for the Blue Mountain Shale

The mechanical properties of the different rock units (on the small and rock-mass scales), as used in the pillar-scale cavern stability analysis, are listed in Table 3.3.

Table 3.3: Intact Rock and Rock Mass Properties Used for the Pillar-scale Cavern Stability Analysis

Unit	ρ (kg/m^3)	E (GPa)	ν	K (GPa)	G (GPa)	UCS (MPa)	ϕ (°)	c (MPa)	T (MPa)
Blue Mountain Shale Rock Mass	2700	3.80	0.10	1.58	1.73		26.3	2.61	0.28
Cobourg Intact	2700	36.72	0.31	32.21	14.02	93.5			
Weak Sherman Fall Intact	2700	10.74	0.08	4.26	4.97	30.08			
Sherman Fall Rock Mass	2700	16.81	0.31	14.75	6.42		34.7	4.27	0.33

Note: Although the tensile strength was measured in the Brazilian tests (Gorski et al. 2009a, Table A-7; Gorski et al. 2010a, Tables A-9 and A-10), those exact values were not used in the analyses. The tensile strength was reduced from the laboratory values for the Blue Mountain shale and Sherman Fall limestone using the Hoek-Brown failure criterion. The tensile strength for the Cobourg limestone is approximated by the tensile strength of the Voronoi block calibration (Section 3.1.3).

3.1.3 Voronoi Block Approximation of Cobourg Limestone

All rocks have a microstructure. The Voronoi tessellation scheme is numerical methodology used to represent microstructure and consists of an assembly of small polygonal blocks. The blocks can be rigid or deformable, and, if deformable, either elastic or elastic-plastic. The blocks interact with each other through their contacts, which initially are elastic when the stresses are relatively small. As the load in the contacts increases, they can fail, either in tension or shear. Contact failure in tension is controlled by the contact tensile strength. The Coulomb slip criterion governs the onset of inelastic shear deformation, or slip of the block contact. Contacts between Voronoi blocks do not represent the actual internal structure of rocks. Instead, they are oriented randomly at relatively short spacing, acting as possible locations and orientations of discrete flaws within the rock. Failing of a contact in shear or tension represents fracturing of the rock mass. Fracturing initiates and evolves as a function of rock mass strength, and as dictated by stresses and forces in the rock mass. An example of the use of the Voronoi block approach for stability analysis of underground excavations at the Yucca Mountain Project, the U.S. program for high-level nuclear waste disposal, is described by Damjanac et al. (2007). The advantage of the Voronoi block approach is that it can simulate fracturing of a brittle rock mass, the formation of loose and unstable ground, and its rockfall. Continuum-based numerical models can be used to predict the redistribution of stresses, displacements and regions of inelastic deformation and damage, but they cannot predict rockfall. One small disadvantage of the Voronoi block approach is that micro-mechanical properties (of contacts and blocks) are not measured directly in laboratories. Instead, they have to be determined indirectly through the calibration process, in which micro-mechanical properties are adjusted until the macro-mechanical behaviour measured in laboratories is matched by the response of the Voronoi block model in the numerical simulation of that laboratory experiment.

The model is discretized into Voronoi blocks in the region around the cavern where stress concentrations from the in situ stresses and external loading occur. The average Voronoi block size (width) is selected to be 0.3 m. The ratio of the block size to the cavern span, which is $0.3/8.6 = 0.035 << 1$, is sufficiently small so that the block size does not affect the model results.

3.1.4 Voronoi Model Calibration

The Voronoi block model is calibrated to the laboratory mechanical properties of the Cobourg limestone and the weak Sherman Fall limestone. The calibration is conducted by simulating the laboratory experiments used to determine the laboratory properties of the rocks. The most important mechanical parameters that control stability of the underground excavation are UCS and Young's modulus (stiffness). The micro-mechanical parameters of the Voronoi block model are adjusted in order to match the stiffness and strength of the Cobourg limestone and weak Sherman Fall limestone (as listed in Table 3.3).

The following are the micro-mechanical parameters that need to be determined in the calibration process:

contact normal stiffness................... k_n
contact shear stiffness..................... k_s
block Young's modulus.................... E
block Poisson's ratio......................... ν
contact peak cohesion...................... c_p
contact peak friction .... ϕ_p
contact peak tensile strength........... T_p
contact residual friction.................... ϕ_r

The model parameters also include residual cohesion and tensile strength of the contacts. In all of the analyses discussed here, both of those parameters were considered to be zero in order to simulate the Cobourg limestone as a brittle material.

Matching of Young's modulus and Poisson's ratio and the macro-failure strength envelope defined by cohesion, friction angle and tensile strength, is an under-determined problem, because there are more micro-mechanical constants than constraints. The problem is resolved by assuming that the stiffness of the Voronoi blocks is much greater (>10) than the stiffness of the contacts, meaning that the contacts are the main contributors to the compliance of the model. The other extreme also is analyzed, when the contacts are much stiffer than the blocks. The results of the two approximations are found to be quite similar (BSC 2004a). In the case of the calibration of micro-mechanical strength parameters, additional constraints used to bound the solution were mode of failure and its evolution as a function of confinement, and post-peak behaviour (e.g., post-peak softening strain and residual strength). It was observed in unconfined laboratory tests that the Cobourg limestone fails predominantly by axial splitting. The post-peak behaviour recorded during 4 experiments illustrates quite a brittle response of the Cobourg limestone after failure. Therefore, the micro-mechanical strength parameters used in the Voronoi block model were adjusted to result in a brittle sample failure.

The calibration was carried out on 5 Voronoi block samples generated using different realizations of random block geometry. The results of the numerical simulation for one realization (number 3) of unconfined compression, direct tension and bi-axial compression tests (for 15 MPa and 30 MPa confinements) are shown in Figure 3.6 and Figure 3.7. The tests were carried out on 5 m edge square samples. It was not necessary to have a 2:1 height-to-width ratio for the tested samples, because perfectly frictionless boundary conditions were applied in the numerical tests on the loaded ends of the sample. (The height-to-width ratio of 2:1 is necessary in the laboratory tests in which the platen friction cannot be made zero, to ensure uniaxial stress state in the middle of the sample. In the numerical tests, the platen friction is exactly zero). Axial stress-strain curves are shown in Figure 3.6 for each test (on one sample), together with sample configuration and the displacement vector field in the final failure state. (Young's modulus for that case is indicated in the plot.) Red lines in the sample plots indicate the locations of micro fractures. The sample fails by axial splitting in the unconfined compression test. In case of confined tests, the micro fractures coalesce to form macroscopic "shear bands". The volumetric strain as a function of the axial strain for realization 3 is shown in Figure 3.7. The Poisson's ratio and average dilation angles (Ψ) for that particular case are indicated in the plot. The dilation angles vary as a function of confinement, being greatest for unconfined loading conditions.

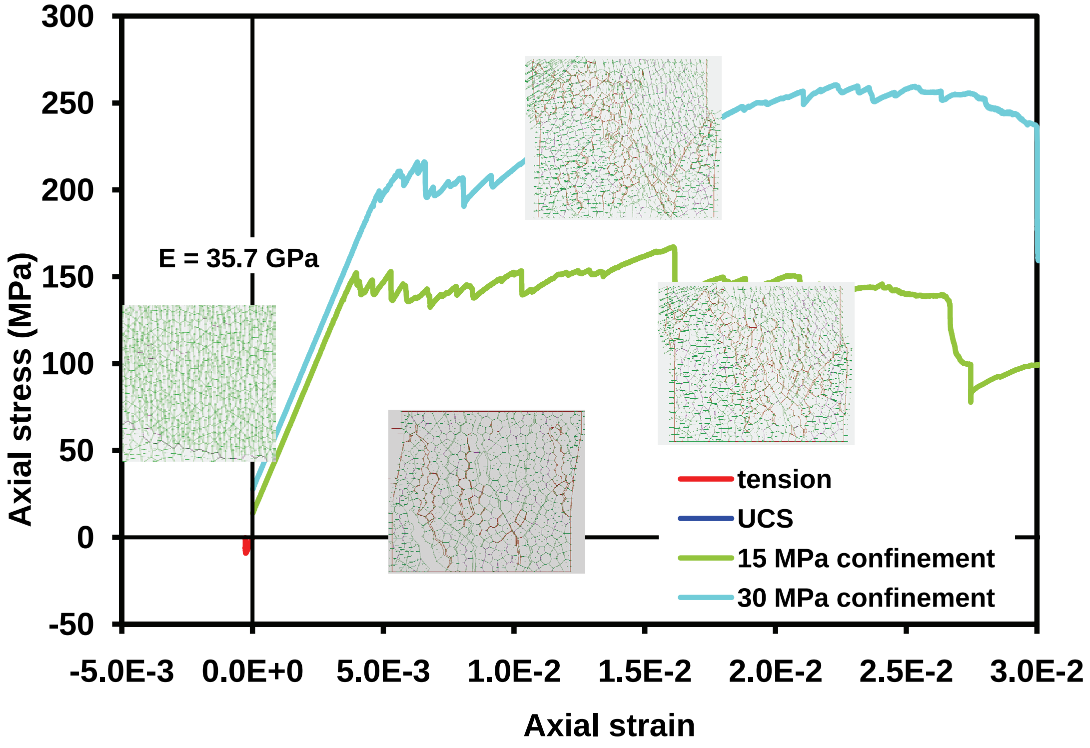

Figure 3.6: Axial Response Obtained from the Numerical Tests on Calibrated Voronoi Block Model of Cobourg Limestone (Compression Positive)

The stiffness and strength parameters that represent the properties of the Voronoi block samples are summarized in Tables 3.4 through 3.6. The results of uniaxial tests are listed in Table 3.4; confined test results are in Tables 3.5 and 3.6 for 15 MPa and 30 MPa confinement, respectively. The Young's modulus of 36.1 GPa and the UCS of 93.7 MPa, which are averages calculated from the results for 5 Voronoi block samples, are in good agreement with the target values of 36.7 GPa and 93.5 MPa, respectively, for the Cobourg limestone listed in Table 3.3.

The failure data for the Cobourg limestone in principal stress space are shown in Figure 3.8, as obtained from the laboratory tests and the results of numerical tests on the Voronoi block model. The comparison indicates that calibrated Voronoi block model represents the failure envelope of the material very well. In general, the failure data for the model have a lower failure load than the laboratory data, because of strength reduction by one standard deviation. The numerical data show greater failure load than the experimental data, on average, only for 30 MPa confinement.

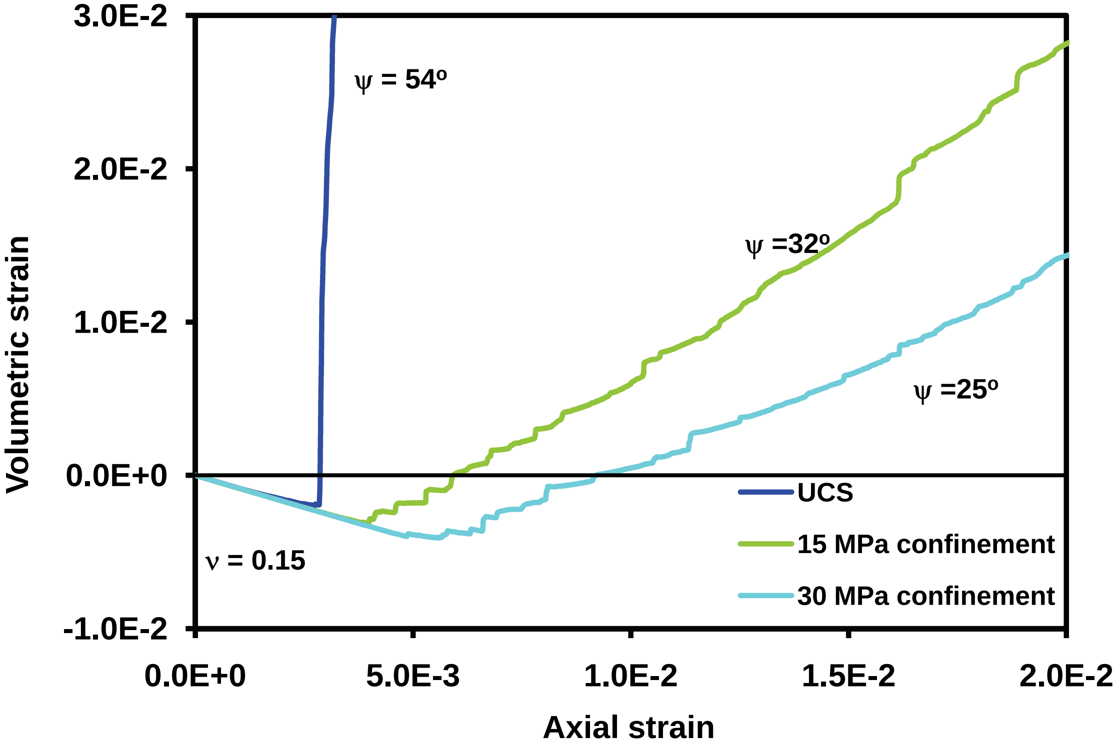

Figure 3.7: Volumetric Response Obtained from the Numerical Tests on the Calibrated Voronoi Block Model of Cobourg Limestone

Table 3.4: Summary of Voronoi Stiffness and Strength Parameters from Unconfined Tests

Case	E (MPa)	Poisson's Ratio	UCS (MPa)	Residual Strength (MPa)	Residual/ Peak Strength	Dilation Angle (°)	Tensile Strength (MPa)
1	35.8	0.15	87.2	17.5	0.20	53	-8.7
2	36.3	0.15	98.9	9.5	0.10	52	-9.0
3	35.7	0.15	95.7	13.0	0.14	54	-9.1
4	36.6	0.14	88.1	10.3	0.12	52	-8.8
5	36.0	0.14	98.5	12.8	0.13	53	-8.4
Average	**36.1**	**0.15**	**93.7**	**12.6**	**0.14**	**53**	**-8.8**

Table 3.5: Summary of Voronoi Strength and Dilation Values from Biaxial Tests for 15 MPa Confinement

Case	Strength (MPa)	Dilation Angle (°)
1	157	35
2	187	37
3	167	32
4	180	35
5	182	38
Average	**175**	**35**

Table 3.6: Summary of Voronoi Strength and Dilation Values from Biaxial Tests for 30 MPa Confinement

Case	Strength (MPa)	Dilation Angle (°)
1	254	32
2	321	33
3	260	25
4	275	33
5	289	36
Average	**280**	**32**

However, the reason for that observation is apparent from Figure 3.6. The curve for 30 MPa confinement shows that after yielding and some post-peak softening, the model exhibits strain hardening, and the maximum stress (50 MPa greater than initial yield strength) is reached at 2.5% strain. The absolute maximum stress, not the initial yield stress, is recorded in the numerical model as a failure load. However, when the maximum stress is reached, the sample is already in the failure state. During the laboratory testing, the initial yield stress is recorded as the failure load.

Direct tension tests were not carried out on the Cobourg limestone. The tests on the Voronoi block model indicate approximately a 10:1 ratio between compressive and tensile strengths. Although that ratio is typically in the range of 15:1 or 20:1 for rock masses, 10:1 is reasonable for the generally massive Cobourg limestone. Tensile strength obtained from Brazilian tests is in the range of 8 MPa to 9 MPa.

The post-peak behaviour observed in the numerical tests for three compression tests is quite different (e.g., Figure 3.6). Unconfined response is brittle. At 15 MPa confinement, the response of synthetic material is almost perfectly plastic. As discussed previously, at 30 MPa confinement, the model generally exhibits strain-hardening post-peak behaviour. Such a response is qualitatively typical for rocks. To ensure that the numerical model does not overestimate the strength of the rock and does not yield unconservative predictions of failure of excavations, it is necessary that the model has: 1) equal or lower yield strength (as illustrated in Figure 3.8), 2) equal or more brittle post-peak response and 3) equal or lower residual strength, compared to the mechanical behaviour of the analyzed rock mass. The post-peak response for 4 samples of the Cobourg limestone measured in the laboratory tests and obtained from numerical simulations during calibration for 5 realizations of Voronoi block geometry are compared in Figure 3.9. The numerical model matches the post-peak behaviour (both softening rate and residual strength) measured in the laboratory tests very well.

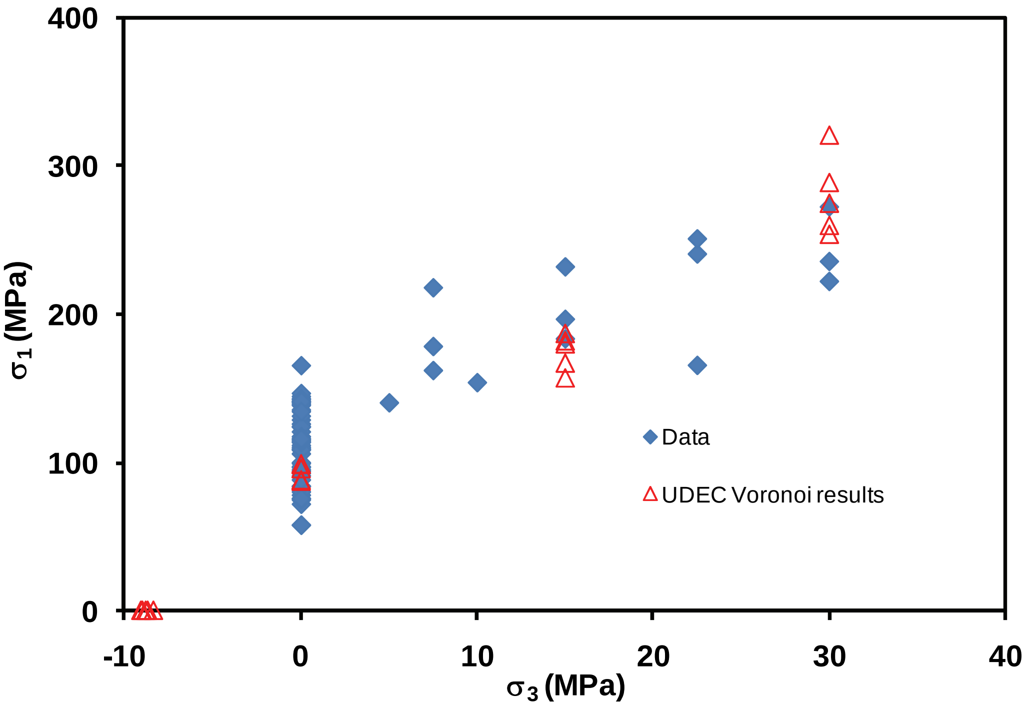

Note: Compression is positive.

Figure 3.8: Failure Data in $\sigma_1 - \sigma_3$ Space from Laboratory Experiments and Numerical Tests on the Talibrated Voronoi Block Model of Cobourg Limestone

The model response (including the calibration tests) will not be identical between different realizations of the block geometry (as illustrated in Tables 3.4 through 3.6), because the geometry of the Voronoi blocks is random. Although there is variability between different block geometry realizations in the model response, it is important that variability is relatively small, within 10% of the mean. The variability for 5 samples used in the calibration is less than 7%, which is much less than the variability of the laboratory test results.

The calibrated micro-mechanical properties for Cobourg limestone and weak Sherman Fall limestone are listed in Table 3.7. Those properties were assumed to be uniform throughout the model (or the sample). The effect of spatially variable properties (i.e., normally distributed joint peak cohesion and tension with a standard deviation between 10% and 30% of the mean) on the mechanical behaviour of the Voronoi block model, which also was investigated, was not significant, therefore it was not considered justifiable to introduce that as an additional complexity into the model.

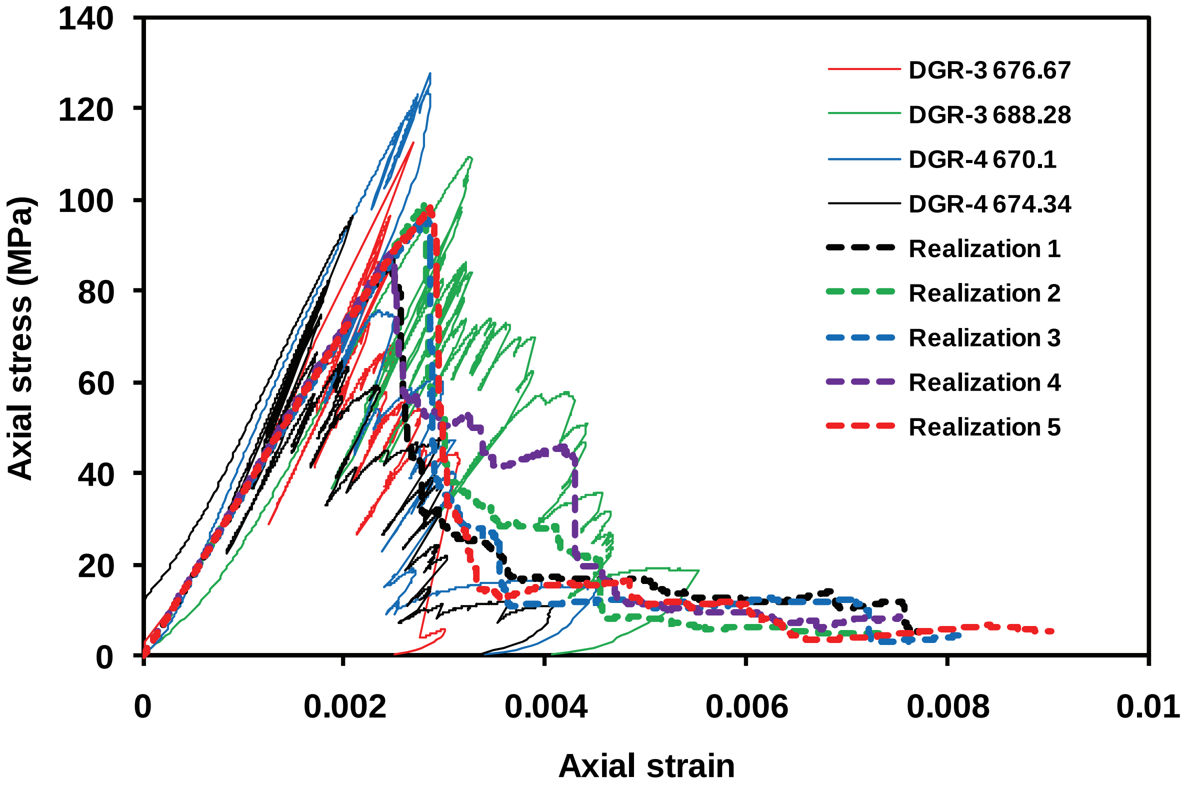

Note: The thin, continuous lines are from laboratory tests; the thick, dashed lines are from Voronoi block model.

Figure 3.9: Unconfined Stress-strain Curves Including the Post-peak Response from Laboratory Tests and Calibrated Voronoi Block Model

Table 3.7: Calibrated Micro-mechanical Properties for the Voronoi Block Contacts

Unit	Cobourg	Weak Sherman Fall
Contact Normal Stiffness k_n (GPa/m)	170	47.8
Contact Shear Stiffness k_s (GPa/m)	85	23.9
Block Bulk Modulus K (GPa)	328.9	92.4
Block Shear Modulus G (GPa)	247.3	69.5
Contact Peak Cohesion c (MPa)	36.4	12.1
Contact Peak Friction ϕ_p (°)	35	35
Contact Peak Tensile Strength T (MPa)	14.5	4.84
Contact Residual Friction ϕ_r (°)	15	15

Notes: Residual micro-tension and cohesion are assumed to be zero.

3.1.5 Long-term Strength

In the analysis of the long-term performance of the DGR the important factor could be time-dependent strength degradation. It was observed that rocks loaded at certain stress, smaller than the short-term strength (typically measured in laboratories), but greater than the long-term or true strength, can fail if that stress is maintained for a sufficiently long time period. If the stress is equal to or less than the long-term strength (a fraction of the short-term strength), the rock will not fail, irrespective of the stress (load) duration. In the static-fatigue tests, the samples are loaded by the load smaller than their short-term strength. That load is maintained constant until the sample fails, which is recorded as the time-to-failure. The objective of the long-term tests carried out on the samples taken at the DGR site was to determine the long-term strength of the rock (i.e., the stress at which their strength does not degrade with time), not the complete static-fatigue (or time-to-failure) curves.

The long-term strength testing of the Cobourg limestone was carried out on the samples taken from DGR-2 (Gorski et al. 2009b), DGR-3 and DGR-4 (Gorski et al. 2010b). There were 5 tests on samples from DGR-2 and 6 tests from both DGR-3 and DGR-4. For each long-term test, a long specimen was cut into 2 pieces. One piece was tested instantaneously to obtain short-term strength (UCS). The other piece was loaded at stress, σ, in the range between 0.2 and 0.4 of UCS. That load was maintained for 100 days, when the sample was loaded to failure. Thus, the test measures the change (decrease) in the rock strength (or damage accumulation) after 100 days of load at certain stress level. The results of long-term strength testing on all samples are presented in Figure 3.10. There is no obvious trend in data. Three measurements at approximately 0.35 UCS show some decrease in strength. However, other measurements at the same or greater load show increase in strength. The average of UCS_{100}/UCS of all measurement is 1.11. That implies the effect of damage accumulation at the tested load levels for 100 days is practically zero, or of the second order compared to natural variability of strength between relatively close samples. Based on existing test results, it can be concluded that there is no strength degradation for the loads less than or equal to 0.35 (of the mean) UCS or 39 MPa. Such a result is in agreement with unconfined test data (Table 3.1), which show that the crack initiation stress, CI, is 41% of UCS or 45.6 MPa. Many experts in the field believe that the lower bound value of the long-term strength of the rock is equal to or greater than crack initiation in uniaxial compressive tests, CI (Damjanac and Fairhurst 2010).

The shafts extend through all units in the geological profile above, including the Cobourg limestone (Figure 3.1). A number of bulkheads are designed along the shafts to prevent transport of water and gases along the shafts as potential pathways with increased permeability. The shaft analysis is focused on the locations of the bulkheads; therefore the material properties of the units where the bulkheads are located are of particular interest. A greater number of the geological units extending above and below the repository are included in the panel-scale models compared to the pillar-scale models. Also, the representation of the mechanical behaviour of the units in panel-scale models is different than the one discussed in Section 3.1. The shaft and panel-scale analyses were carried out using continuum numerical codes FLAC and FLAC3D. Derivation of parameters that characterize mechanical behaviour of all units used in the continuum models for shaft and panel-scale analyses are discussed in this chapter.

3.2 Geological Units and Their Properties in Shaft and Panel-Scale Analyses

Over the past 20 years there is growing evidence that the failure of brittle rock cannot be represented by a simple linear Mohr-Coulomb or non-linear failure envelope. Today brittle failure is analyzed using a concept of cohesion loss and friction mobilization (Martin 1997).

Diederichs (2007) used this concept to develop the damage initiation and spalling limit (DISL) failure envelope, which represents the failure of brittle, low porosity rock as fundamentally a process of progressive failure involving cohesion loss and friction mobilization. Martin et al. (1999) demonstrated using case histories that this concept was essential in predicting the extent of damage around underground openings in brittle rock masses. The DISL approach and a conventional GSI approach (Hoek-Brown rock mass envelope) are both appropriate methods and were considered as possible approaches for derivation of material properties for the analyses. The DISL approach can be used to predict the extent of brittle failure observed around underground openings; the GSI approach consists of scaling the intact rock properties to account for rock-mass shear behaviour based on the GSI classification system. Figure 3.11 compares the failure envelopes for the two approaches, and clearly shows that the GSI approach is a more conservative estimate of the peak strength. Therefore, the GSI approach was used as the basis for derivation of all continuum strength properties of the models discussed in this report (see also Section 3.1.2).

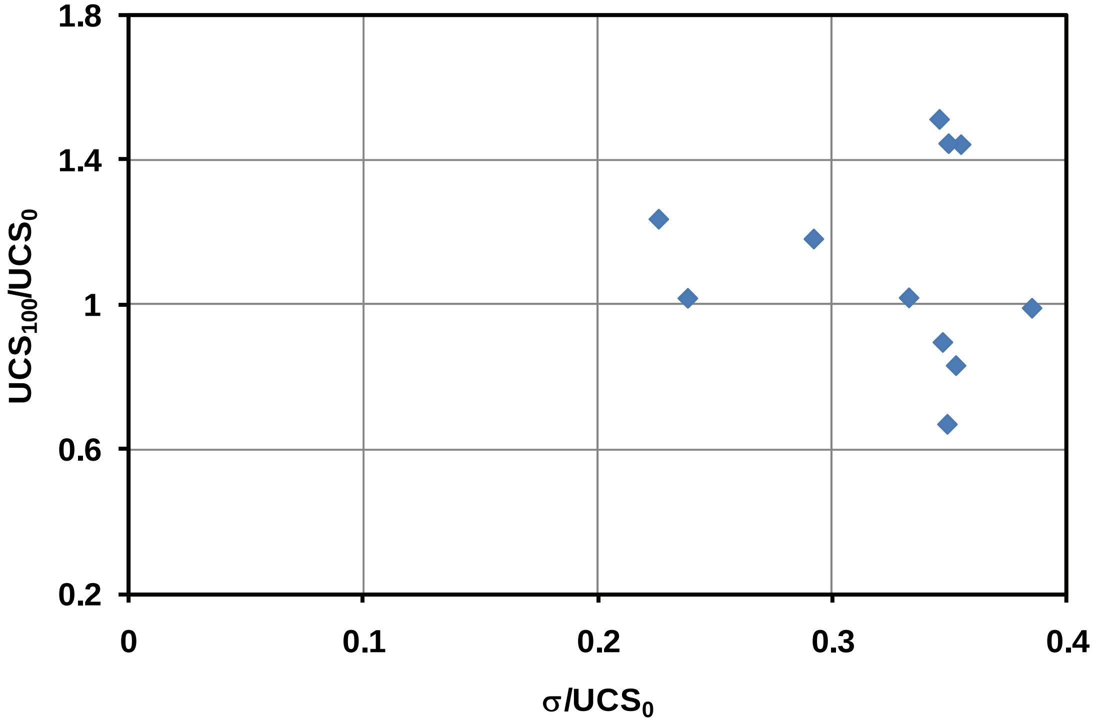

Note: UCS_{100} normalized to the initial uniaxial compressive strength (UCS_o) as a function of the long-term load (σ) normalized to the initial uniaxial compressive strength (UCS_o).

Figure 3.10: Uniaxial Strength of the Cobourg Limestone after 100 Days

Axisymmetric FLAC modelling of a shaft using the ubiquitous joint model to simulate the bedding planes were carried out with the assumption that the bedding plane cohesive strength was equal to bedding plane tensile strength. Bedding plane cohesive strength of 1 and 2 MPa with a friction angle of 30° was used for the analyses. The results from those models indicated that the horizontal bedding planes have negligible effect on the extent of failure predicted by the FLAC model. As a result of these findings, the horizontal bedding planes were not accounted for in the FLAC3D shaft analyses explicitly. Instead, the bedding planes were accounted for by reducing the laboratory strength properties to the rock mass strength properties using the GSI approach.

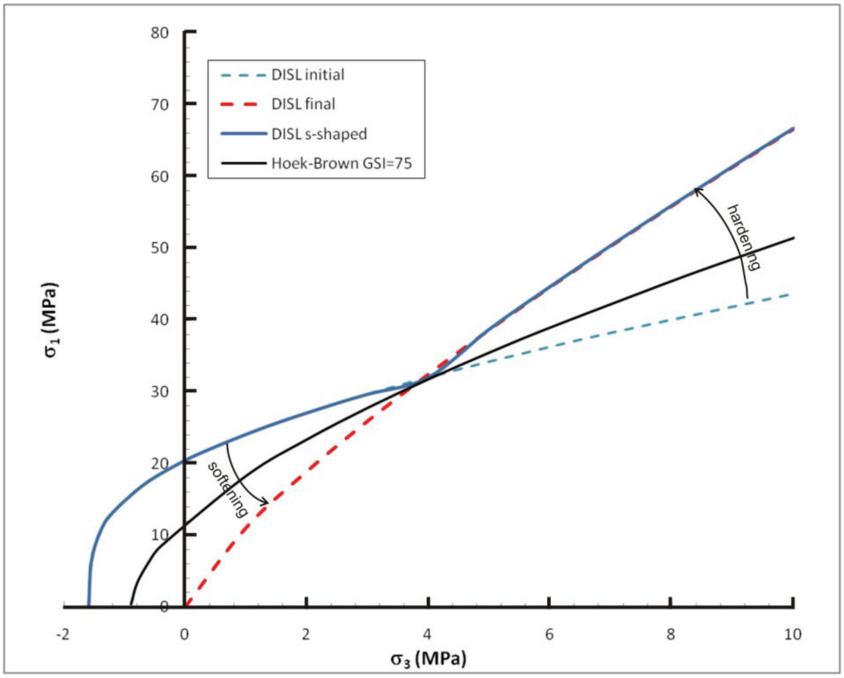

Note: The envelopes indicate that the GSI approach results in lower peak strength at low confining-stress levels, providing more conservative analysis results.

Figure 3.11: Hoek-Brown and DISL Envelopes for Queenston Shale (UCS = 48 MPa, GSI = 75, m_i = 8)

Swelling of both the geological units and the backfill materials is anticipated to provide additional confinement to the rock, and generally provide a stabilizing influence (i.e., reduced damage). Therefore, it was conservative not to include swelling effects as part of the analyses. Moreover, the strengthening effects of grouting the rock mass around the shaft also were not accounted for in the analyses.

The laboratory data used to develop rock mass properties of the units used in the shaft and panel-scale analyses compiled from Gorski et al. (Gorski et al. 2009a, 2009b, 2010a, 2010b, 2010c) and Wigston and Heagle (2009) are shown in Table 3.8. A strain-softening Mohr-Coulomb material model was used for all geological units in the shaft and panel-scale analyses. The only exception is the Cobourg limestone in the panel-scale analysis, which is represented as a ubiquitous-joint Mohr-Coulomb material, with matrix properties as listed in Table 3.3, and ubiquitous joint strength corresponding to bedding plane properties listed in Table 3.2. The rock mass properties were developed based on the approaches proposed by Hoek et al. (2002) and incorporated into the software program RocLab (ROCSCIENCE 2007), as already discussed in Section 3.1.2. Based on discussions with the DGR project Peer Review Committee, GSI = 75 and $m_i = 8$, with damage factor D = 0, were used as a starting point to develop properties for the units. The dilation angle was set at 50% of the peak friction angle. (Vermeer and de Borst (1984) suggest that dilation angle is between 0 and 20° approximately. The selected 50% of the peak dilation angle roughly coincides with the upper bound of the range). The residual post-peak strength parameters were based on a GSI = 75 and $m_i = 8$, with damage factor increased to D = 0.5 and a low value of s = 0.0001. Peak and post-peak model parameters (listed in Table 3.8), based on these suggested properties, are an initial estimate.

Table 3.8: Rock Mass Strength and Stiffness Properties Used in the Analyses

Unit	Intact Rock		Rock Mass Properties							
	UCS	E (GPa)	GSI	m_i	E (GPa)	c (MPa)	ϕ	T (MPa)	c_r (MPa)	ϕ_r
Sherman Fall Limestone	55.6	26.6	(65)*	(12)	(16.8)	(4.27)	(34.7)	(0.33)	(3.45)	(31.4)
Blue Mountain Shale	21.7	5.2	75 (70)	8	4.2 (3.8)	1.62 (2.61)	36.3 (26.3)	0.41 (0.28)	1.12 (2.13)	34.8 (23.8)
Georgian Bay Shale	40.8	11.8	75	8	9.6	2.75 (3.78)	38.1 (32.8)	0.77	1.80 (2.83)	36.6 (30.9)
Queenston Shale	48.0	15.4	75	8	12.6	2.97 (3.82)	39.7 (35.2)	0.91	1.83 (2.71)	38.4 (33.5)
Manitoulin Dolostone	70.7	23.9	75	8	19.5	3.77 (4.51)	42.8 (39.2)	1.34	2.02 (2.84)	42.2 (37.7)
Cabot Head Shale	12.6	4.5	75	8	3.7	1.37	30.3	0.24	1.07	28.4
Goat Island/ Gasport/ Lions Head/ Fossil Hill Dolostones	148.3	37.0	75	8	30.2	8.15	42.2	2.81	4.5	41.2
Guelph Dolostone	60.4	27.8	75	8	22.7	4.65	35.8	1.15	3.26	34.1
Salina A0 Dolostone	197.6	63.4	75	8	51.8	8.98	47.0	3.75	3.58	47.4
Saline A1 Evaporate	20.0	11.7	75	8	9.6	2.07	31.1	0.38	1.60	29.2
Salina A1 Carbonate	116.7	39.7	75	8	32.4	5.95	43.9	2.21	2.98	43.3
Salina C Shale	35.0	8.0	75	8	6.5	2.68	35.9	0.66	1.87	34.2

Note: Values in parentheses were used in the repository panel scale analysis; the difference in the peak and residual cohesion and friction angle is because in the panel scale analysis the maximum stress in the calculation of Mohr-Coulomb fit to the Hoek-Brown failure envelope was assumed to be horizontal stress, estimated using horizontal stress coefficient equal to 2. In the shaft analyses, the maximum stress is estimated based on coefficients in Table 4.2.

The main shaft will be backfilled with intermittent bulkheads and seals consisting of concrete, asphalt, bentonite-sand mixture and engineered compacted fill. Only some of the properties of these materials were provided to Itasca; those not provided were estimated based on typical values found in the literature (Akgun et al. 2006, Clifton et al. 1995, Huber and Decker 1995). The properties used to simulate the backfill/seal materials are listed in Table 3.9. A perfectly plastic Mohr-Coulomb material behaviour model was used for all backfill/seal materials. It was assumed that the concrete bulkheads degrade over a period of 100,000 years (Little et al. 2009) to a final state representative of compacted gravel ($E = 200\,\mathrm{MPa}$ and ν=0.15). This was achieved in the model by reducing the strength and stiffness properties linearly over this time period. Stresses within the softened/weakened material also were reduced appropriately to account for the associated change in secant modulus.

Table 3.9: Mechanical and Strength Properties of Seal Materials Used in the Numerical Analyses

Material	Density (Mg/m^3)	Young's Modulus E (GPa)	Poisson's Ratio ν	c' (MPa)	ϕ' (°)	T (MPa)
Sand-Bentonite (70:30 mix)	2.0	0.2	0.32	0.09	16	0
Concrete (UCS=70 MPa)	2.4	36	0.16	17.8	36	4.7
Asphalt (UCS=0.85 MPa)	2.4	1.5	0.45	0.18	43	0.06

4. LOADING CONDITIONS

The long-term stability of the caverns and shafts is analyzed considering different processes and loads that can affect their stability over a period of 1 Ma, including in situ stresses, time-dependent strength degradation, gas (inside the cavern) and pore pressures (inside the rock mass) and multiple glacial and seismic events. The analysis has been carried out for in situ stresses, time-dependent strength degradation and gas and pore pressures occurring concurrently.

The glacial events occur periodically, with variable time intervals between the events (of the order of tens of thousands of years), variable duration of the events (of the order of thousands of years) and variable maximum thickness of the ice sheet (and, equivalently, glacial loading on the repository of the order of tens of megapascals) during the events. Stability of the caverns is analyzed for multiple glacial events, until the steady state response to glacial loading is achieved (i.e., damage and fracturing within the model do not change during additional glacial load cycles). Stability of the caverns, subject to seismic event with 10^{-5} and 10^{-6} probabilities of annual exceedance, also is investigated assuming that seismic events occur at different stages during degradation of the caverns (as result of time-dependent strength degradation and multiple glacial cycles). The shaft analysis was carried out for single glacial and single seismic events, because the analysis has shown that those events do not have significant effect on shaft stability or on the extent of the damage around the shafts.

Different loading conditions and their representation in the models are discussed in this chapter.

4.1 In Situ Stresses

Although the in situ stresses have not been measured at the site, the extensive stress measurements have been carried out at shallow depth in the Southern Ontario. The stress tensor at the depth of the repository has been constrained by these local stress measurements, stress measurements at the Norton Mine (at depth of approximately 670 mBGS), repeated borehole televiewer surveys and extensive bounding analyses. As one of the initial steps in the numerical modelling program, an attempt to gain further insight into the range of in situ stress conditions was made. A simple three-dimensional model of the stratigraphy at the proposed DGR site is used to evaluate the effect of tectonic strains on the distribution of stresses in the different stratigraphic units (Cartwright 1997). The stresses developed in the model then were verified by comparison with limiting stress conditions, estimated from borehole breakout observations and other data from the literature.

The in situ stress estimates from several sources were available. Adams and Bell (1991) provided a summary of in situ stresses for the St. Laurence Platform, with a proposed stress distribution. In situ stress gradients pertinent to the DGR site were provided by a survey of the Canadian In Situ Stress Database compiled by Arjang (2001) and reviewed specifically for the DGR site by Kaiser and Maloney (2005). Bauer et al. (2005) describe the in situ stresses measured using the USBM overcore method at the Norton Mine, near Akron, Ohio. The room-and-pillar limestone mine is located within the 15 m thick Columbus limestone formation (E=49 GPa and ν=0.25) at a depth of 670 mBGS. The measurements indicated the following in situ stress field:

$$\sigma_H = 36.7\,\mathrm{MPa}\ \text{(N75°W)}$$

$$\sigma_h = 28.3\,\mathrm{MPa}$$

$$\sigma_v = 22.5\,\text{MPa} \text{ (\textasciitilde 1.26 times overburden)}$$

Valley and Maloney (2010) used a comparison of the strength of the various rock units with the extent of borehole breakouts from televiewer observations to bound the in situ stress profile at the DGR.

In order to develop a three-dimensional FLAC3D model that captures the important aspects of the site stratigraphy, without unnecessary complexity, the stratigraphy was simplified into model units of similar mechanical behaviour. The basis of these decisions was a relative comparison of the elastic properties of the geological unit, the geological descriptions of the units (OPG 2011) and units designated by Valley and Maloney (2009) as a means of limiting in situ stress estimates.

The elastic properties were arrived at by compiling and averaging the elastic properties from laboratory testing on cores from all four boreholes (DGR-1 through -4) for each proposed model unit. The testing consisted of uniaxial compressive strength, triaxial compressive strength, long-term compressive strength, and Brazilian testing. In total, data from 176 different laboratory tests were correlated. At the time of the study, test data were not available for all units. Units where testing was unavailable were grouped with adjacent units of similar geological description. The proposed model units and elastic properties are provided in Table 4.1.

Table 4.1: Stratigraphic Units Selected for Modelling Purposes and Corresponding Elastic Properties

Stratigraphic Unit	Top of Unit (mBGS)	Bottom of Unit (mBGS)	Thickness (m)	Density (Mg/m^3)	Young's Modulus: E (GPa)	Poisson's Ratio: ν
1	0.0	11.8	11.8	1.95	0.03	0.3
	Formations:	Overburden				
2	11.8	131.1	119.3	2.68	38.3** (7.7)	0.18
	Formations:	Lucas, Amherstberg, Bois Blanc				
3*	131.1	175.6	44.5	2.88	20.0** (4)	0.62^+ (0.3)
	Formations:	Bass Island				
4	175.6	227.9	52.3	2.55	13.9	0.22
	Formations:	Salina G and F				
5*	227.9	379.0	151.1	2.70	22.6	0.32
	Formations:	Salina E, D, C, B, B Evaporite, A2, A2 Evaporite, A1, A1 Evaporite, A0				
6	379.0	415.1	36.1	2.65	37.0	0.37
	Formations:	Guelph, Goat Island, Gasport, Lions Head, Fossil Hill				
7	415.1	612.3	197.2	2.66	13.8	0.3
	Formations:	Cabot Head, Manitoulin, Queenston, Georgian Bay				

Stratigraphic Unit	Top of Unit (mBGS)	Bottom of Unit (mBGS)	Thickness (m)	Density (Mg/m^3)	Young's Modulus: E (GPa)	Poisson's Ratio: ν
8*	612.3	656.3	44	2.59	5.2	0.1$^+$ (0.3)
	Formations:	Blue Mountain, Blue Mountain –Lower				
9	656.3	664.7	8.4	2.64	31.5	0.25
	Formations:	Cobourg-Collingwood				
10*	664.7	692.6	27.9	2.67	37.1	0.33
	Formations:	Cobourg-Lower				
11*	692.6	847.8	155.2	2.69	23.9	0.21
	Formations:	Sherman Fall, Kirkfield, Coboconk, Gull River, Shadow Lake				
12	847.8			2.7	76.6	0.25
	Formations:	Cambrian/Precambrian				

Notes: *Units that correspond to limiting in situ stress condition calculations (Valley and Maloney, 2010). ** To account for rock mass properties, 20% of intact stiffness will be used for units above the Salina Formation. $^+$ Value seems unlikely. A more conventional value of 0.3 will be used.

The in situ stresses at the DGR site were evaluated using a simplified FLAC3D model (1 m × 1 m in plan) of the DGR stratigraphy. The model was set up to be orientated in the direction of the in situ principal stresses (maximum stress oriented approximately NE-SW). It was then strained horizontally with constant velocity in both horizontal directions to simulate the tectonic forces. Several model iterations were carried out with different strain magnitudes until the model-produced in situ stresses were similar to those reported in the literature. A total strain of 5.16×10^{-4} in the maximum horizontal stress direction and 2.84×10^{-4} in the minimum horizontal stress direction produced a good match to the in situ stress data.

The maximum and minimum horizontal stress distributions from the model are shown in Figure 4.1, along with the relevant in situ stress data. It can be seen that the calculated stress distribution agrees well with the data available from the literature. The maximum (σ_H) and minimum (σ_h) horizontal stresses are listed in Table 4.2, along with the elastically calculated maximum tangential stress around a circular opening ($\sigma_{\max}$) in several of the geological units.

4.2 Time-Dependent Strength Degradation

One objective of the analysis presented here is to predict the amount of rockfall and degradation of the caverns and development of the EDZ around the shafts due to long-term (1 Ma) rock-strength degradation of the host rock units around the repository excavations subjected to in situ and glacially induced stresses.

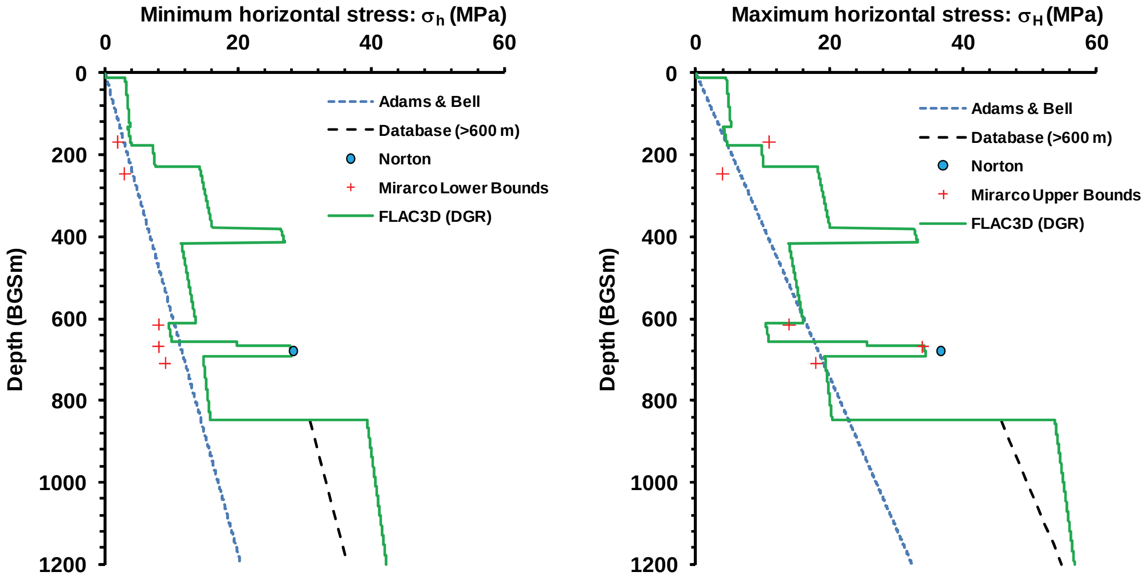

Note: Data from other sources are shown for comparison.

Figure 4.1: Maximum and Minimum Horizontal In Situ Stresses Predicted by FLAC3D Model of DGR Stratigraphy

Table 4.2: Maximum and Minimum Horizontal Stresses from the FLAC3D Model at the Base of Units Considered in the Shaft-seal Analyses

Geological Unit	σ_H (MPa)	σ_h (MPa)	σ_{max} (MPa)
Salina C Shale	18.7	14.8	41.3
Salina A1 Carbonate	20	16	44
Salina A1 Evaporite	20.1	16.1	44.2
Salina A0 Dolostone	20.2	16.2	44.4
Guelph Dolostone	32.7	26.5	71.6
Manitoulin Dolostone	14.3	11.8	31.1
Queenston Shale	15.2	12.7	32.9
Georgian Bay Shale	16.1	13.6	34.7
Blue Mountain Shale	11	10	23

4.2.1 Static-Fatigue Curves and Evolution of Damage Due to Strength Degradation

The static-fatigue (long-term) behaviour of a rock forms the basis of the model for simulating time-dependent processes. The static-fatigue curves, which are obtained from laboratory tests on small samples, provide the time-to-failure (t_f) of the material at a particular driving-stress ratio (σ / σ_c)[2]. The laboratory tests that are used to establish these static-fatigue curves have duration periods of less than 100 days and driving-stress ratios that are close to the short-term failure load. In addition, the tests are conducted in an unconfined condition. These tests show that when the driving-stress ratio approaches 50% of the short-term strength, failure is not observed. Damjanac and Fairhurst (2010) reviewed the issues and processes associated with such tests and proposed that a driving-stress threshold must exist for massive rock masses below which no damage occurs. Based on geological evidence and numerical modelling, they suggest that this lower limit occurs at a driving-stress ratio of approximately 40 to 60% of the short-term laboratory strength, and is equivalent to the crack-initiation stress measured in unconfined laboratory samples.

There are few static-fatigue datasets to evaluate if rock type has any influence on the slope of the static-fatigue curve. Schmidtke and Lajtai (1985) established the static-fatigue relationship for unconfined Lac du Bonnet granite and Lau et al. (2000) evaluated the static-fatigue relationship for confined (5 MPa and 10 MPa) samples (Figure 4.2a). Unlike the tests by Schmidtke and Lajtai (1985), the tests by Lau et al. (2000) measured the stress-strain throughout the duration of tests and were able to establish the driving-stress ratio relative to the crack damage stress, which typically is used to establish the long-term strength of brittle material such as rock and concrete (Martin and Chandler 1994). Lau et al. (2000) showed that when the driving-stress ratio was less than the crack damage stress, the samples did not fail irrespective of the duration of the applied stress. Data sets for each confinement were fit with a straight line, and the line was extrapolated to encompass driving-stress ratios measured. The approximation of static-fatigue line as used in the long-term stability analyses is shown in Figure 4.2b.

Limited time-dependent testing was carried out for the Cobourg limestone. The primary purpose of this testing was to assess the long-term strength threshold approximated by the crack initiation stress proposed by Damjanac and Fairhurst (2010). Consequently, all testing had driving-stress ratios that were between 0.2 and 0.4 of the UCS, or equal to or less than the crack initiation stress. No samples failed or showed strength reduction during 100 days of testing. Consequently, the long-term pillar-scale stability analyses were carried out assuming that the long-term strength ranged between 31.5 MPa and the crack initiation stress of 45 MPa for the Cobourg limestone (see Section 3.1.5). The additional panel-scale sensitivity analyses were carried out in which the long-term strength was assumed to vary between 0.4 and 0.8 of the short-term strength.

---

[2] The following notation is employed to describe the results of static-fatigue tests. The applied load in the axial direction and the confining pressure are denoted by σ_1 and P_c, respectively. The axial load at failure during a short-term test is denoted by σ_f. The stress difference maintained during a static-fatigue test conducted at a confining pressure of P_c is $\sigma = \sigma_1 - P_c$. The stress difference at failure during a short-term test is $\sigma_c = \sigma_f - P_c$. To facilitate comparison between different data sets, we generate a static-fatigue curve by plotting the logarithm of time-to-failure, t_f, versus the driving-stress ratio given by $\sigma / \sigma_c = \left(\sigma_1 - P_c\right) / \left(\sigma_f - P_c\right)$.

Once the lower-bound long-term strength was established, the next step was to develop a numerical process that degrades the short-term strength to the long-term strength. The evolution of damage, expressed in terms of the damage coefficient, D, which is the ratio of the degraded to the initial strength, for the Lac du Bonnet granite was developed using the discrete element software PFC (ITASCA 1999, BSC 2004a) and is shown in Figure 4.3.

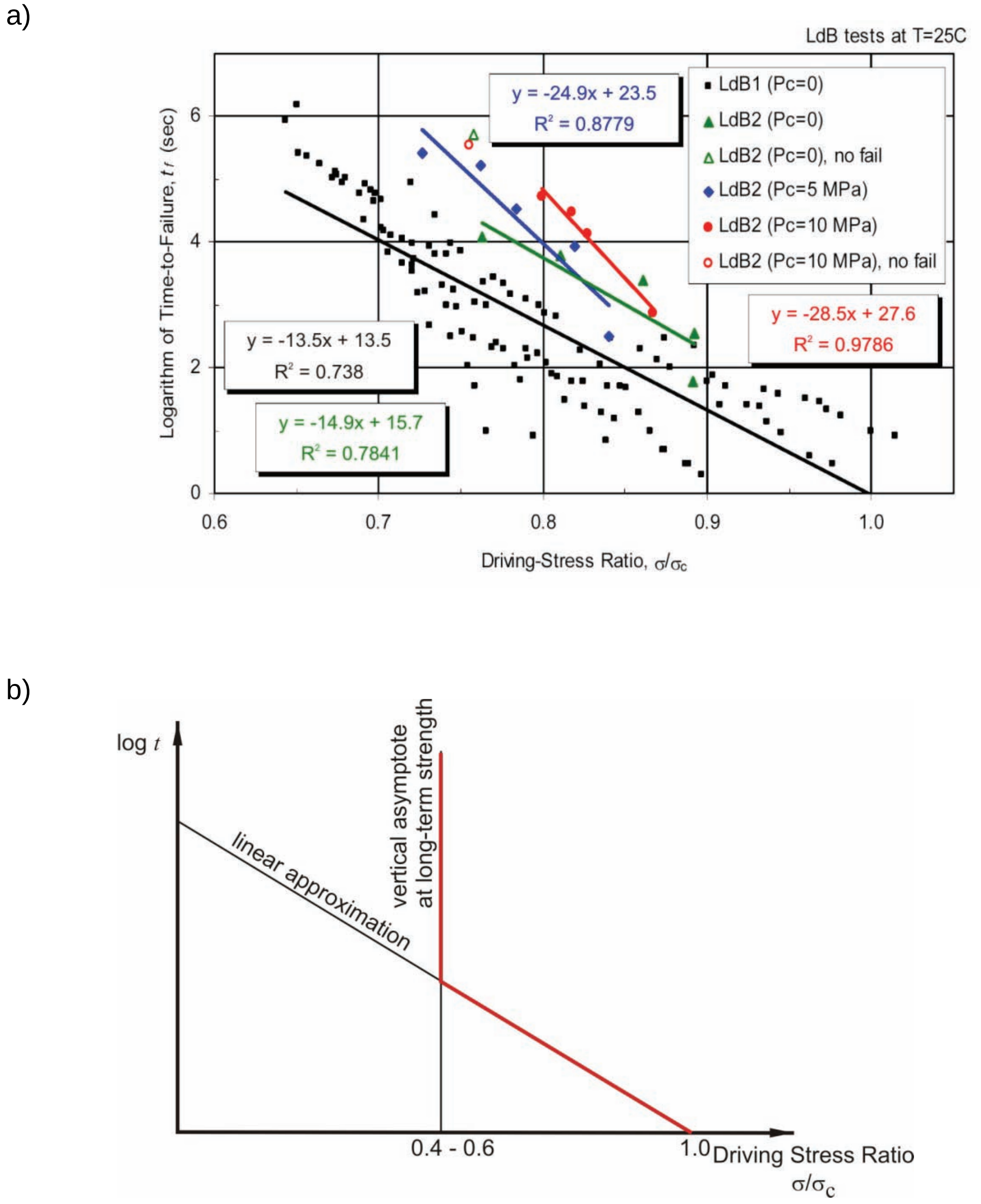

Notes: a) Laboratory static-fatigue data for Lac du Bonnet granite established by Schmidtke and Lajtai (1985) for unconfined conditions (LdB1) and Lau et al. (2000) for unconfined and confined conditions (LdB2). b) The static-fatigue curves (red line) for a rock mass based on the approach by Damjanac and Fairhurst (2010).

Figure 4.2: Bases and Approximation of Rock Mass Static-fatigue Curves Used in Long-term Cavern Stability Analyses

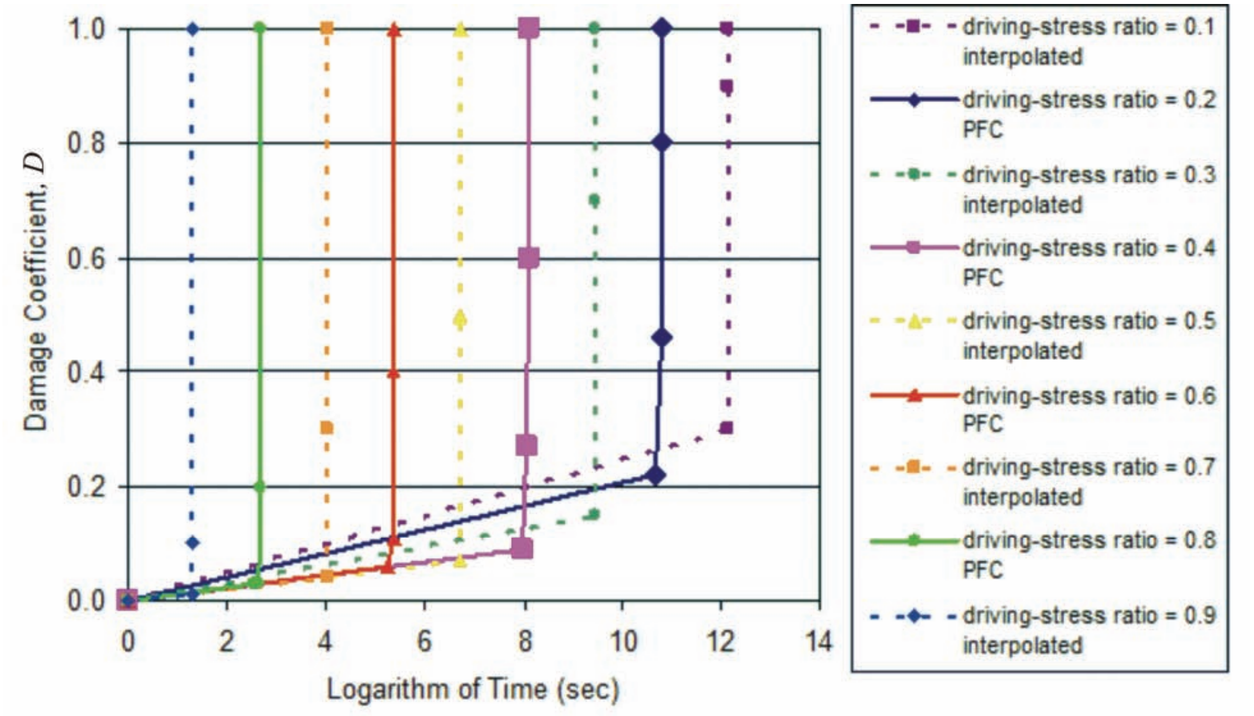

Notes: Each curve has a vertical asymptote at a time-to-failure for a given driving-stress ratio, which is provided by the LdB (P_c = 0) curve from Figure 4.2a. The evolution of damage up to the vertical asymptote (i.e., the failure time) is provided by the PFC time-dependent model.

Figure 4.3: Damage Curves Used as Input to the UDEC LdB Analyses ($P_c = 0$)

Two parameters control the predictions of time-dependent strength degradation and, eventually, the predictions of rockfall: 1) time-to-failure, and 2) damage evolution (rate) before time-to-failure. Time-to-failure as a function of the stress state (i.e., the driving stress) is determined from the static-fatigue lines constructed by interpolation and extrapolation of the only available comprehensive testing results (obtained on Lac du Bonnet granite) and from the test data on the long-term strength obtained on the Cobourg limestone. Damage rates at different stress levels are generated using the PFC stress corrosion model. There is concern about the level of uncertainty in PFC predictions and how the damage rates affect the final result of the model (i.e., the rockfall induced by time-dependent strength degradation). In order to investigate the sensitivity of the model predictions to the damage rate, new damage curves are generated where the damage rates for all driving stress levels are assumed to be the same, equal to the maximum rate predicted by PFC. The rockfall predictions due to time-dependent strength reduction, using different damage curves, are compared (BSC 2004a). It was confirmed that the considered variation of damage rates has no practical effect on predicted rockfall. Time-to-failure is the main factor controlling evolution of the rockfall due to time-dependent strength reduction. Consequently, predictions are not very sensitive to the input from the PFC stress corrosion model.

4.2.2 Time-dependent Strength Degradation in UDEC

Implementation of the time-dependent strength degradation scheme in the cavern stability model, which uses UDEC Voronoi block model (Section 3.1.3), is discussed in detail in this section. The implementation of the approach used in FLAC3D (the continuum code) shaft analyses is practically identical. The only difference is that in the continuum model the cohesion and tensile strength of strain-softening Mohr-Coulomb constitutive model are reduced to account for time-dependent strength degradation.

The long-term strength degradation of the Cobourg and Sherman Fall limestone units was implemented in the UDEC model by incrementally referencing a series of tables defining evolution of damage due to strength degradation as obtained from the PFC time-dependent model (Figure 4.3). Based upon the local driving-stress ratio at the Voronoi block contacts within the UDEC model, the strength of the contact in the model is degraded as a function of time. The times considered were 1, 2, 5, 10, 20, 50, 100, 200, 500, 1000, 200, 5000, 10,000, 20,000, 50,000, 100,000, 200,000, 500,000 and 1 Ma.

Time-dependent strength degradation in the UDEC model is generalized by a damage coefficient, D, which is in the range between zero and one. The cohesion and tensile strength of the material are assumed to be functions of time:

$$\begin{aligned} c(t) &= c_o D(t) \\ T(t) &= T_o D(t) \end{aligned} \tag{5}$$

where: c_0 and T_0 are the initial, short-term cohesion and tensile strength of contacts in the UDEC model, respectively. The large-scale short-term strength of the UDEC synthetic model of the rock mass is proportional to the cohesion and tensile strength of the contacts, c_0 and T_0, respectively. Consequently, the time-dependent strength of the UDEC synthetic model of rock mass will decay proportionally to $D(t)$.

It is assumed that, in the general case:

$$\frac{dD}{dt} = f(\mathrm{F}, D) \tag{6}$$

where: F, a function of stress state and material strength, defines the driving stress. For unconfined stress conditions (i.e., $P_c = 0$), function F must be identical to the ratio of the axial load and the unconfined short-term strength: $\mathrm{F}(P_c = 0) \equiv \sigma_1 / \sigma_f$. The load at failure during a short-term test is calculated as follows (Jaeger and Cook 1979, pp. 95 – 97):

$$\begin{aligned} \sigma_f &= P_c N_\phi + 2c\sqrt{N_\phi} \\ N_\phi &= \frac{1+\sin\phi}{1-\sin\phi} \end{aligned} \tag{7}$$

where: c and ϕ are the rock mass cohesion and friction angle, respectively. It is assumed that if time-to-failure for two different stress states were the same, then evolution of damage due to strength degradation for both states as a function of time would be the same, irrespective of the confinement. As discussed in this section, given the time-to-failure, the model predictions are not very sensitive to the assumption pertaining to the functional form of damage evolution. Based on the laboratory data of Lau et al. (2000) and Schmidtke and Lajtai (1985), the slope of the static-fatigue line, $k(P_c) = \Delta(\sigma / \sigma_c) / \Delta \log(t_f)$ is sensitive to the confining pressure. For example, the slope k of the static-fatigue lines for LdB granite (see Figure 4.3) is 0.051/log(s) for unconfined and 0.031/log(s) for 5 MPa confined conditions.

Given the conservative nature of the static-fatigue approach, it was assumed that linearizing the dependence of the slope k on confinement P_c was a reasonable simplification due to the observation that failure and damage usually take place at low confinements. The form of function F used in the UDEC model to capture the static-fatigue time-dependent induced damage is:

$$\mathrm{F} = 1 - \frac{k(0)}{k(P_c)}\left(1 - \frac{\sigma}{\sigma_c}\right) \tag{8}$$

The damage evolution D(F;t) was generated using PFC for values of function F in the range between zero and one, and used as the UDEC input data in a tabular form (see Figure 4.3). Interpolation was carried out for stress states in the model during the simulation, for which function F did not coincide with values for which the tables were provided. This is reasonable given the data in Figure 4.3 are generated for small driving-stress increment of 0.1.

It is convenient for numerical implementation in UDEC that the damage increment in Equation 6 depends on accumulated damage, which is a function of the stress history. Although the stress state (at a given point) can have a complex history as a function of time (due to stress redistribution), it is sufficient to only keep track of accumulated damage in the simulation. The calculation of the damage increment in the UDEC simulation was carried out in the following manner: (1) for the time increment Δt, it is assumed that the stress state and the stress function, F, at a given point in the model are constant, $\mathrm{F} = \mathrm{F}_i$ (2) the table of damage evolution $D(\mathrm{F};t)$ is selected or interpolated based on tables provided (3) a point on the damage evolution curve corresponding to accumulated damage D_i is determined $D_j = D(\mathrm{F}_i;t_j)$ and (4) the damage increment is calculated as:

$$\Delta D = D(\mathrm{F}_i;t_j + \Delta t) - D(\mathrm{F}_i;t_j) \tag{9}$$

Time increment(s) for the simulation must be selected. The only criteria for selection are the accuracy of the simulation and calculation time. The stress state is assumed to be constant during the time increment. Preliminary investigations showed that selected time increments did not affect model results significantly.

Damage is calculated and accumulated for the Voronoi contacts to simulate the rock mass strength degradation with time. The stress state used for calculation of the damage is determined by averaging stresses in the blocks separated by a contact.

4.3 Gas and Pore Pressures

Corrosion and microbial degradation of the wastes and packages inside the DGR will result in the generation of gases. Because of the low permeability of the host rock, a significant amount of gas will remain inside the repository, which could result in a gradual build-up of gas pressure.

To estimate this gas pressure, detailed gas flow and transport modeling was employed using T2GGM (QUINTESSA and INTERA 2011). T2GGM comprises a TOUGH2/EOS3 2-phase gas and water transport model (Pruess et al. 1999), coupled to a custom gas-generation model (GGM).

GGM has been developed to simulate various microbial and corrosion processes, the gas evolution of the repository, and its interaction with the geosphere. GGM tracks the production and consumption of the key chemical species (e.g., metals, organic wastes, gases, water) and tracks the fluxes of the water and gases into and out of the repository. GGM includes four key mechanisms for the generation of gas and consumption of water:

1. Microbial degradation of organic wastes;
2. Hydrogen reactions including methanogenesis;
3. Corrosion of metallic wastes; and
4. CO_2-enhanced corrosion of metallic wastes and formation of siderite ($FeCO_3$).

These processes may occur in either the saturated (water submerged) or vapour phases.

The rates of generation or consumption of water and gas within the repository are interpreted as sources for water and gas within TOUGH2's 2-phase flow model of the repository. TOUGH2 simulates the transport of gas and water through the repository and geosphere.

The GGM model of the repository and the TOUGH2 model of the geosphere are coupled via the total gas pressure, repository gas/water saturation, relative humidity, and repository void volume. The coupled model is refered to as T2GGM. These couplings determine the flows of water and of gas into and out of the repository.

The principal results of the modelling as they relate to gas generation and water processes within the repository (INTERA and QUINTESSA 2011) are summarized below.

1. Oxygen within the repository is consumed and conditions become anaerobic shortly after the repository closure.
2. Moisture initially present in the wastes, plus water that seeps into the repository from the surrounding rock and the shaft, support the anaerobic corrosion of metals and the degradation of organic wastes, resulting in generation of hydrogen, CO_2 and CH_4 gases. The gas pressure in the repository rises grradually.
3. There is a pressure balance between the water seepage into the repository and the gas generation within the repository. The very low permeability of the rock precludes significant water saturation of the repository for the 1-Ma assessment period. In some sensitivity cases, the repository is virtually dry (or completely unsaturated) after 100 ka.
4. Over the 1Ma period, the peak repository gas pressure is in the range of 7 to 9 MPa, converging towards or somewhate higher than the steady state environmental head at the repository horizon of around 7 MPa, and much less than the lithostatic pressure of about 17 MPa at the repository horizon.
5. Methane is generally the dominant gas throughout the evolution of the repository, due to degradation of organic wastes and the consumption of hydrogen and carbon dioxide via the microbial methanogenic reaction.

For the DGR geomechanical stability analysis, two simplified cases of gas pressure histories were developed representing a base case condition with gas pressure plateau at 7 MPa at about 100,000 years postclosure and an extreme case scenario with 15 MPa peak gas pressures approaching lithostatic pressure. Figure 4.4 shows these simplified gas pressure profiles comparing with profiles from various gas modelling cases for the normal evolution scenario in the repository with time (INTERA and QUINTESSA 2011). Both base and extreme case gas pressure histories will be used to provide insight on the mechanical effects on the DGR cavern stability.

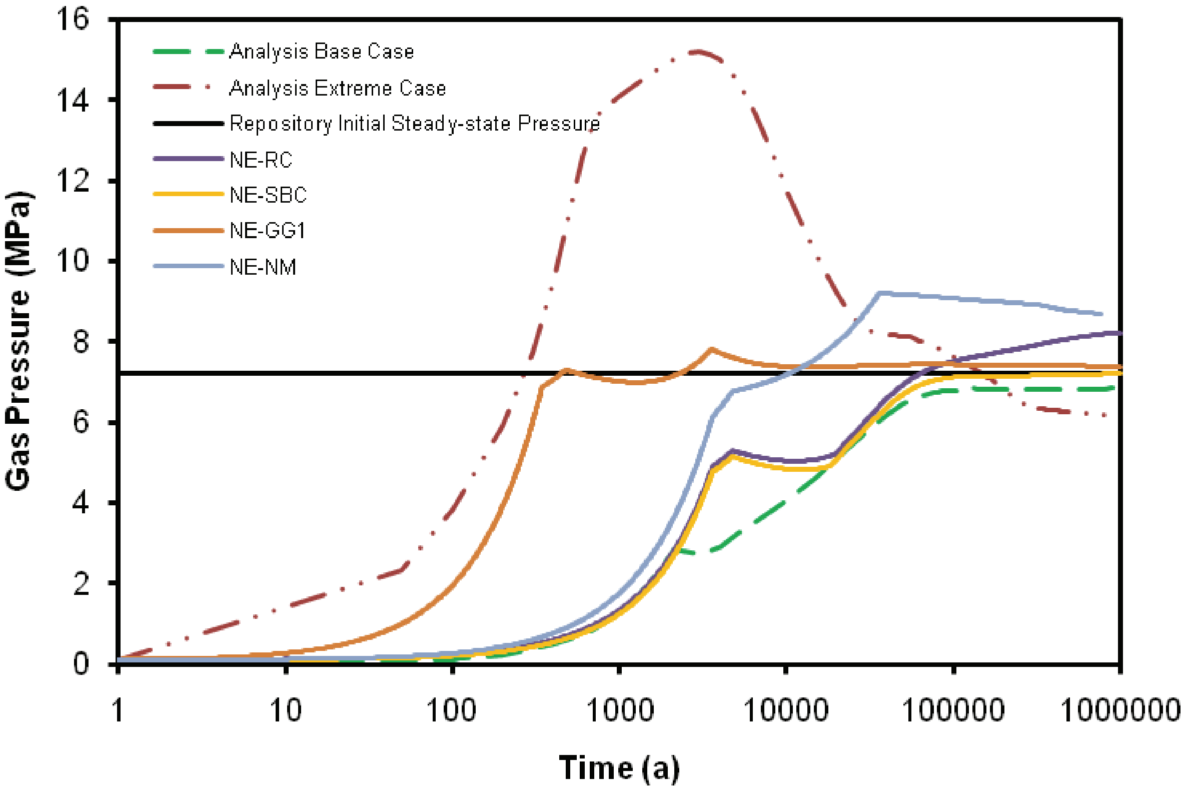

Notre: NE-RC = DGR Reference Case, NE-SBC = Steady-state Cambrian Overpressure Case, NE-GG1 = Increase Gas Generation Case, and NE-NM = Methanogenic Reaction Case. Figure from AECOM (2011).

Figure 4.4: Repository Gas Pressure Histories Used in Geomechanical Stability Analyses

4.3.1 Modelling Approach

Corrosion processes of the waste packages inside the caverns will result in the generation of gases. During the life of the repository, these gasses may cause pressure changes inside the cavern and in the rock, due to diffusion of the gasses into the surrounding formations. Due to the low permeability of the Cobourg limestone formation, a significant amount of the gas may remain inside of the caverns, resulting in a gradual build-up of gas pressure.

Effective stress analyses that account for pore-pressure effect on the failure of rock has been carried out in order to evaluate the long-term effect of gas and pore pressure evolution inside and around the caverns and shafts. The analyses were carried out using one-way coupling (as opposed to fully-coupled approach), meaning that pore pressure evolution with time was used as input into the mechanical model for deformation and damage, and these pore pressures were used by the material constitutive models. The full effects of mechanical deformation on pore pressure were not accounted for in the analyses. Instead, a simplified approach, described in Section 4.3.4, was used to approximate for the effect of stress-induced fracturing on pore pressure change. This is considered a reasonable methodology to account for the long-term pore pressure evolution because the long-term pore pressure change will be dominated by fluid flow within the geological units.

The base case represents the most unfavourable conditions for damage of rock because it predicts the largest pressures and pressure gradients in the rock. The case that is considered in the cavern stability analysis is the most unfavourable from the perspective of cavern stability, because the gas pressures in the cavern typically are smaller than the pore pressures in the surrounding rock mass. This condition does not represent an unfavourable condition from the perspective of hydraulic fracturing of the rock mass. For that reason, the other extreme was also analyzed, i.e., when the gas pressure inside the cavern is greater than the pore pressures in the rock mass.

The T2GGM output data provided water pressure, gas pressure and gas saturation. These values were converted to an equivalent total pore pressure value, P_e for stability analysis using the equation (Lewis and Schrefler 1998, Section 2.6.1):

$$P_e = S_g \cdot P_g + (1 - S_g) P_w \tag{10}$$

where: S_g is the gas saturation, P_g is the gas pressure and P_w is the water pressure.

4.3.2 Approximation of Pore Pressures Around Caverns

The geometry of the emplacement caverns is not represented explicitly in the analysis of the evolution of gas pressure inside the cavern and pore pressure throughout the rock mass . Instead, the entire repository is simulated as a horizontal slot. Although this approximation is adequate in the analysis of gas and pore pressure changes, the model does not provide the pressure variation in the vicinity of the caverns and in the pillars between the caverns, which is important in the cavern stability analysis. Furthermore, the effect of glacial cycles on pressure changes in the rock mass is not considered in the analysis.

In a general case, fluid flow around the caverns involves two phases: 1) gas generated inside the caverns and 2) in situ water. However, the two-phase flow analysis shows that rock mass in the base case remains almost completely saturated with water throughout 1 Ma. The gas generated inside the caverns does not percolate far into the rock. Thus, in order to resolve detailed pore pressures around the caverns, the analysis of water pressure evolution on the cavern scale is conducted in a single-phase continuum model using the numerical code FLAC (ITASCA 2008). In this model, the gas pressures inside the cavern, as calculated in T2GGM, are used as evolving boundary conditions for water flow inside the rock mass.

The FLAC flow model also accounts for the effect of the glacial loads on the pore pressures. The changes in pore pressures due to stress change and water pressure dissipation during a glacial cycle are simulated. A coupled analysis is conducted. The model is incremented in time at finite time increments, Δt by subsequent execution of the mechanical and flow models. For each time increment, the vertical stress on the top of the model is changed (a result in change in the ice-sheet thickness) and the model is solved for mechanical equilibrium (i.e., pore pressures do not change in this step of the analysis). At the end of the mechanical step, the pore pressure increments, Δp are calculated for each zone of the model based on the mean stress changes, $\Delta\sigma$:

$$\Delta p = B\Delta\sigma \tag{11}$$

where: B is the Skempton coefficient. Detournay and Cheng (1993) suggested that $B = 0.7$ results in conservative estimate of pore-pressure using Equation 11. In the next calculation step, which involves flow simulation only, the gas pressure change inside the cavern predicted to occur over the time increment Δt is applied as the boundary condition inside the cavern, and the flow model is incremented for time Δt allowing pore pressure dissipation. It is assumed that the glacial cycle does not affect the gas pressures inside the cavern. The properties used in the flow analysis (Table 4.3) are consistent with properties used in T2GGM model .

Table 4.3: Flow Model Properties

Porosity	0.02
Horizontal Permeability (m^2)	1.37×10^{-21}
Vertical Permeability (m^2)	1.37×10^{-22}

Because the fluid flow step in the analysis is carried out uncoupled, the fluid bulk modulus is adjusted to account for the effect of rock deformability on specific storage and, equivalently, on diffusivity. The apparent fluid bulk modulus, $K_w^{'}$, is calculated from the following relation (ITASCA 2008, Fluid-Mechanical Interaction Volume):

$$\frac{n}{K_w^{'}} = \frac{1}{M} + \frac{\alpha^2}{G + \frac{4}{3}K} \tag{12}$$

where M is the Biot modulus, α is the Biot coefficient, K is the undrained bulk modulus of rock, G is the shear modulus of rock and n is the porosity. The Biot coefficient is estimated to be 0.5 for low-porosity rocks (Detournay and Cheng 1993). The Biot modulus, M, is calculated to be 52 GPa using the following formula (ITASCA 2008, Fluid-Mechanical Interaction Volume):

$$M = \frac{K_w}{n + (\alpha - n)(1-\alpha)\frac{K_w}{K}} \tag{13}$$

The apparent bulk modulus of fluid of 0.79 GPa was calculated from relation Equation 12 and used in the analyses.

The calculated gas pressures at different times along two vertical profiles, one through the center of the cavern and the other through the center of the pillar, are shown in Figure 4.5 and Figure 4.6.

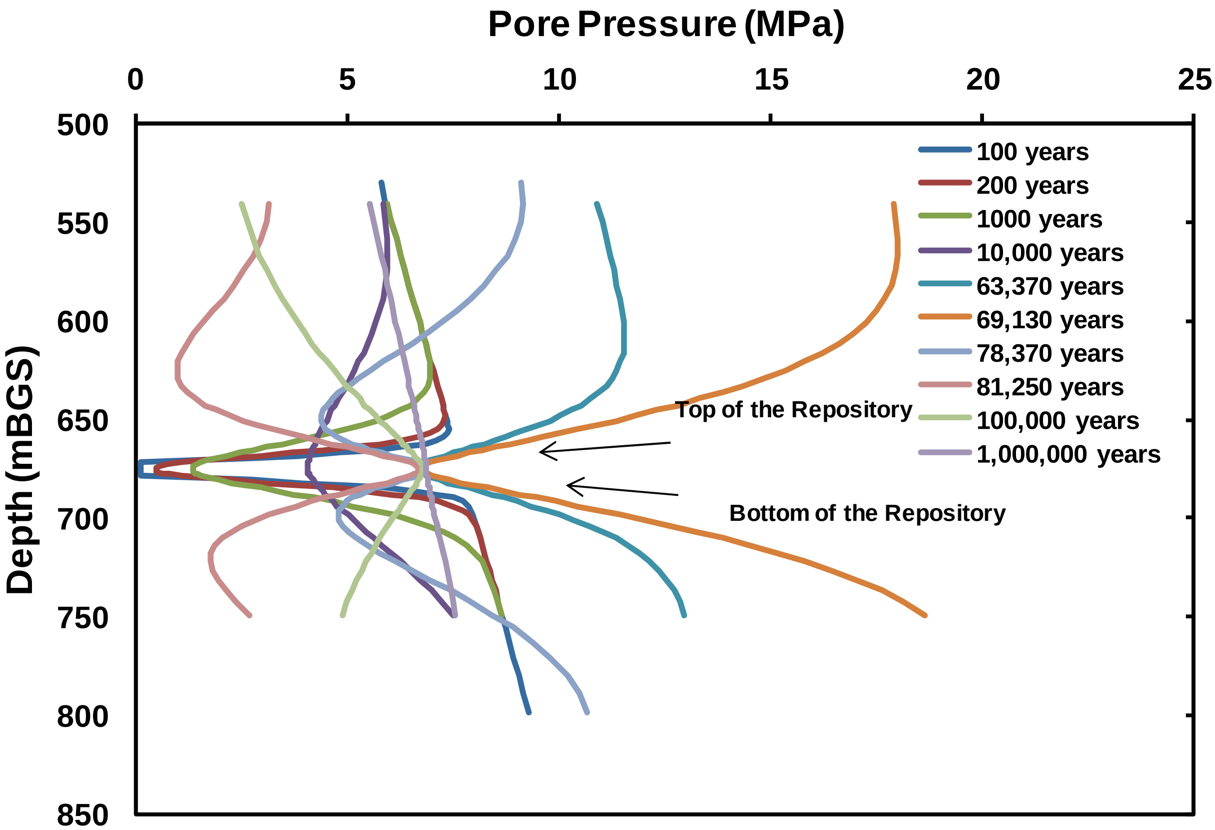

Figure 4.5: Vertical Profiles of Pore Pressure through the Cavern Center at Different Times: Glacial Event Starts at 60,000 Years

The pore pressures are imported in the UDEC model at analyzed times, and used in the effective stress calculations. The pore pressure contours in the vicinity of the caverns and in the pillars as imported in the UDEC model are shown in Figure 4.7. The pressure contours indicate that within the first 100 years the horizontal pressure gradients become negligible. Even during the glacial cycle (Figure 4.6) the pressures throughout the pillar are in equilibrium with pressure inside the cavern. That implies that pore pressures will not have a negative effect on the pillar stability. Although non-negligible pressure gradients in the vertical direction persist for a longer time, after 1000 years they become relatively small compared to the initial and early time conditions. The long-term pressure field around the caverns is somewhat different from the initial far-field pressure, because it is controlled mainly by the gas pressure inside the cavern, which is different (lower) than the initial pressure at the repository elevation. (The pressure contours shown in Figure 4.7 do not show the effect of time-dependent and stress-induced damage on water pressures discussed in Section 4.3.4.)

4.3.3 Approximation of Pore Pressures Around Shaft

Pore pressure data over a distance of 50 m from the shaft center was provided for a period of 1 Ma for several seal locations based on gas/water-pressure evolution modelling of the base case.

The pore pressure histories until 1000 years for seal B1 from the T2GGM base case model is plotted in Figure 4.7. Over the long term, the pore pressure gradually increased to a steady-state value of approximately 3.9 MPa. (Although the pore pressures are shown only until 1000 years, they basically remain constant after 1000 years until 1 Ma.) Within the seal/backfill material, the T2GGM results indicated very high negative pore pressure (>30 MPa). Negative pore pressures were omitted from the FLAC3D models, as these cause an apparent increase in the shear strength.

4.3.4 Effect of Damage on Pore Pressures

The unloading-induced yielding associated with the excavation of underground openings in low porosity sedimentary rocks (e.g., porosity of Cobourg is ~2%) results in a dilatant zone around the excavation boundary. Within this zone, field measurements have shown that the pore pressures are essentially zero (Souley et al. 2007). Predicting pore pressure using conventional poroelasticity concepts leads to erroneous results for these conditions. An approach is implemented in the models used for long-term stability analysis of the caverns and the shafts, in which the pore pressure at the yield/fracture location is conservatively set to the gas pressure inside the cavern or shaft at the instant yielding/fracturing occurs. Although fracturing would cause an instantaneous pressure drop to zero, gas dissipation throughout the dilatant zone (with increased permeability) will equilibrate over some time to the pressure in the underground opening.

Figure 4.8 shows a detail of the Voronoi block assembly used for cavern stability analysis with indications of the fluid forces (the red lines) and damage or micro cracks (the black lines). The scheme of fluid pressure reduction due to micro-cracking is implemented in the model shown in the figure. Because, in this example, the cavern gas pressure is small compared to the pore pressures inside the rock, the figure illustrates that fluid forces act perpendicular to the undamaged contacts between the Voronoi blocks.

A similar scheme was implemented in the FLAC3D shaft (continuum) model to account for pre-peak micro-crack induced pore pressure change. When stress levels in a given model zone reached 80% of the shear strength limit or 90% of the tensile strength limit, the pore pressure in that zone was set equal to the value at the center of the seal/backfill material (or zero when negative pore pressure was indicated). This is based on the assumption that fracturing occurs in the pre-peak range resulting in a significant drop in pore pressure. With time, the pore pressure within the seal/backfill material equilibrates with the rock mass pore pressure, which evolves according to the T2GGM input data. This allows for evaluation of the effect of long-term pore pressure evolution in low-porosity rocks.

4.4 Glacial Loading

The northern portion of North America has been subjected to glacial events over the past million years. These events, which occur periodically, are associated with the development of the ice sheet covering certain portions of the Earth’s surface. The University of Toronto Glacial Systems Model (UofT GSM), which is a model of continental-scale glaciation events, was used by Peltier (2011) to develop a description of glaciation of the Canadian Shield as a means of assessing the impact that such an event would have on performance of the DGR. Eight possible realizations of glaciation and deglaciation during the last 120,000 years were developed, and provide acceptable fits to the observed constraints. Based on these realizations, the maximum ice thickness over southern Ontario, where the DGR is planned, could have exceeded 2.5 km during the most southerly ice sheet advance (Peltier 2011).

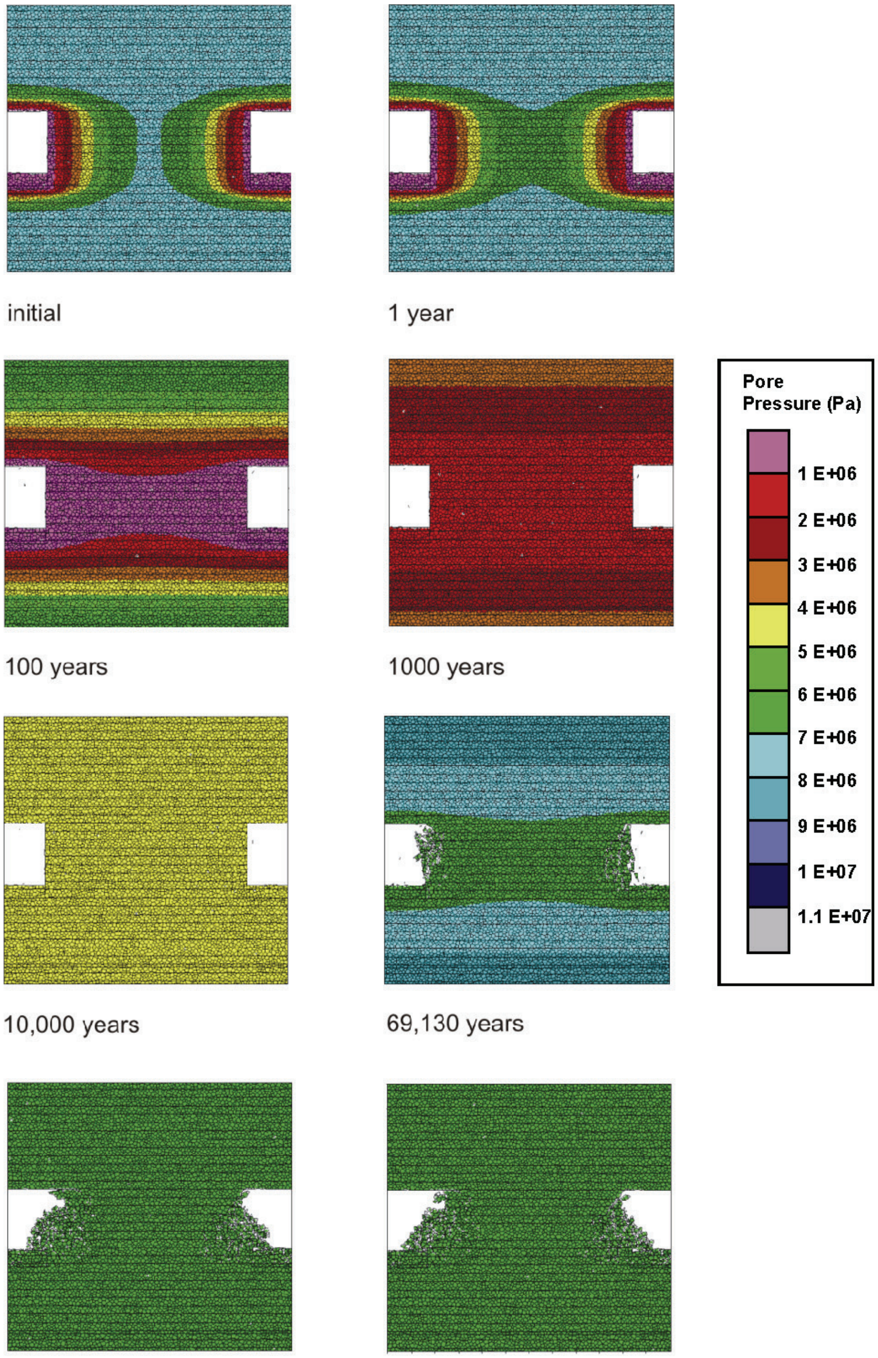

initial

1 year

100 years

1000 years

10,000 years

69,130 years

100,000 years

1,000,000 years

Note: Assuming one glacial cycle starting at 60,000 years .

Figure 4.6: Evolution of Pore Pressure (Pa) Around the Cavern for 1 Ma

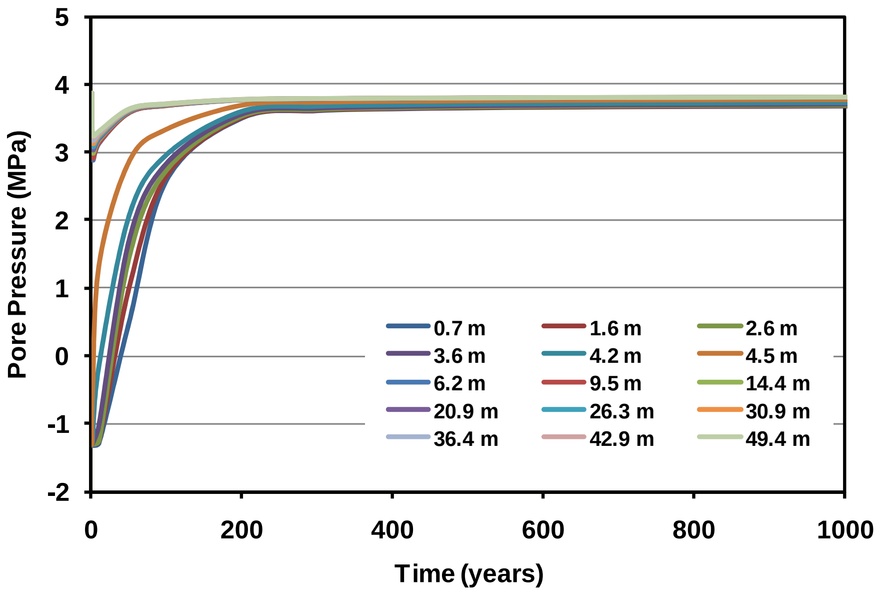

Figure 4.7: Pore Pressure Data (Base Case) at Various Distances from the Shaft Center for Seal B1

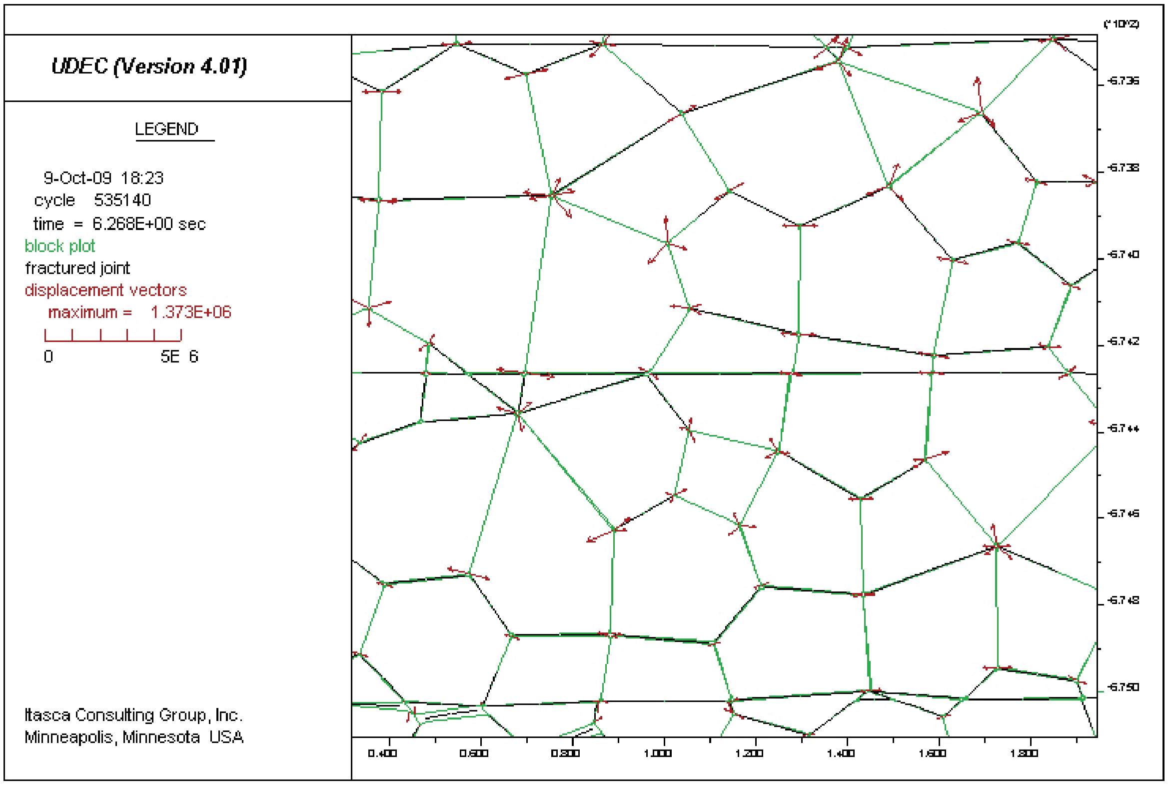

Notes: Fluid forces are represented as the red arrows. Block outlines are in green. Locations of the micro cracks are shown as black lines.

Figure 4.8: Fluid Forces (N) and Damage in the Voronoi Block Model

These glacial models were used to assess how the formation of the ice sheet will affect cavern stability. The weight of the ice sheet will increase both vertical and horizontal normal stresses. Furthermore, as the ice sheet moves sliding at a relatively slow rate, it will impose additional shear stresses on the ground surface. Glacially induced shear stresses were not considered in the analyses, because detailed analyses carried out by Lund et al. (2009) showed that these shear stresses are relatively minor compared to the vertical and horizontal normal stresses. The evolution of vertical normal stresses at the repository location over the last 120,000 years for four analyzed realizations, as taken from Peltier (2011), is shown in Figure 4.9. The greatest vertical stress (approximately 30 MPa) takes place for realization nn9904.

The conditions for the next advance of continental scale glaciation will not be favourable for approximately another 60,000 years (Peltier 2011). However, predictions of possible variations of the ice load during future glaciations are not available. Instead, the repository is analyzed using one of the eight realizations in the previous 120,000 years that resulted in the greatest ice load (i.e., nn9904). (The pressure history for nn9904 is shown in Figure 4.9.) However, the pressure history as shown in was not simulated. Instead, in the case of multiple events, the simulated history of the maximum glacially induced normal stress for one event, shown in Figure 4.10, was applied repeatedly, assuming that glacial episodes start at the different times. The first glacial episode is assumed to start 60,000 years in future.

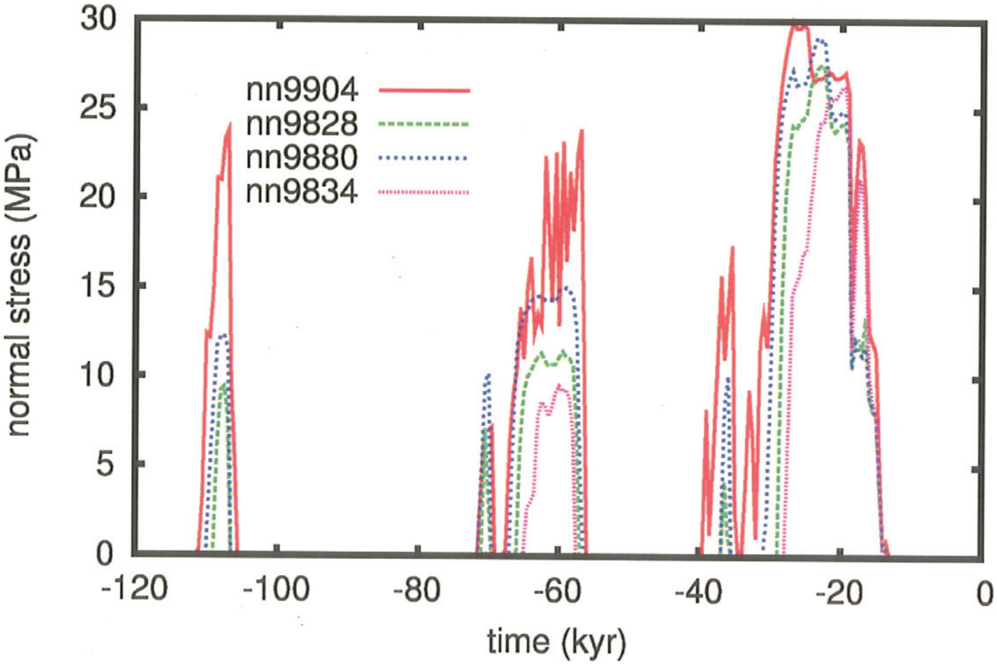

Note: Figure is from Peltier (2011).

Figure 4.9: Four Analyzed Realizations of Normal Stress Due to an Ice Sheet at the Surface of the Earth at the Repository Site

The models also include the horizontal stress increase due to both Poisson’s effect and plate bending. The horizontal stress increase due to Poisson’s effect is:

$$\Delta\sigma_h = \frac{\nu}{1-\nu}\Delta\sigma_v \tag{14}$$

The tectonic plates float on magma. The ice sheet, which typically develops on a part of the tectonic plate, will impose non-uniform loading on the plate and cause its bending. In the upper portions of the Earth's crust, the bending of the plates will cause increase in the horizontal stresses. The increase in the horizontal stress due to plate bending also is assumed proportional to the increase in vertical stress, with the maximum increase assumed to be 2 MPa.

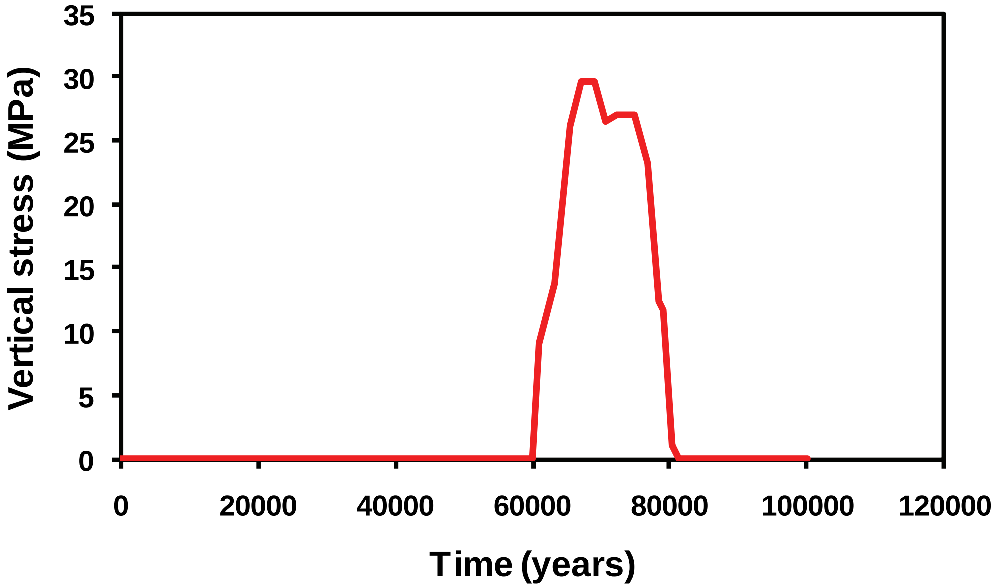

Figure 4.10: Simulated Evolution of Ice Sheet Load During Single Glacial Event as Assumed in the Cavern Stability Analysis

4.5 Seismic Loading

4.5.1 Ground Motions

Stability of the emplacement caverns and the shafts was analyzed for seismic ground motions, which could be generated by earthquakes with an annual probability of exceedance of 10^{-5} for the reference case and 10^{-6} for the extreme case. The ground motion time histories were developed for the ground surface, but also at depths of interest to be used as inputs as the ground motions at the base of the models for stability analysis. Thus, different time histories were used for the cavern and the shaft analyses. The ground motions used as the inputs to the analyses include the surface reflections, because the numerical models do not extend to the ground surface (i.e., they are truncated at some height above the structure of interest) and use the non-reflecting boundaries at the model top.

There are three seismic scenarios with combinations of the earthquake magnitude and the distance from the DGR that match the uniform hazard spectra at each probability level of 10^{-5} and 10^{-6} for the entire frequency range (AMEC GEOMETRIX 2011). Time histories for each seismic scenario include two horizontal components (H1 and H2) and one vertical component (V). The scenarios and the corresponding peak ground velocities (PGVs) and peak ground accelerations (PGAs) for each scenario and each motion component at the repository level and the elevations of shaft concrete bulkheads B1 and B2 are listed in Tables 4.4 and 4.5, respectively. Note that the shaft bulkheads are analyzed for 10^{-6} ground motions only. For example, the entire velocity time histories at the repository level for M7.4 event at 200 km distance are shown in Figure 4.11 through Figure 4.13.

In summary, the maximum PGVs of 22.1 cm/s and 24.3 cm/s, at the repository level and elevation of shaft concrete bulkheads B1 and B2, respectively, at 10^{-6} probability level occur for M6.25 event at 25 km distance. The maximum PGA of 0.5g and 0.61g, at the repository level and elevation of shaft concrete bulkheads B1 and B2, respectively, at 10^{-6} probability level occur for M5.25 event at 10 km distance. The maximum PGV of 11 cm/s at the repository level at 10^{-5} probability level occurs for M6.5 event at 100 km distance. The maximum PGA of 0.16g at the repository level at 10^{-5} probability level occurs for M5.5 event at 20 km distance.

Table 4.4: Analyzed Seismic Scenarios with Corresponding PGVs and PGAs at the Repository Level

Probability	Magnitude	Distance (km)	PGV (cm/s)			PGA (g)		
			H1	H2	V	H1	H2	V
10^{-5}	5.5	20	3.3	4.1	2.5	0.15	0.16	0.11
	6.5	100	6.8	11.0	6.0	0.09	0.10	0.08
	7.4	300	9.5	8.8	5.7	0.05	0.05	0.04
10^{-6}	5.25	10	8.1	9.8	*6.3*	0.45	0.50	0.36
	6.25	25	14.4	22.1	11.8	0.37	0.36	0.28
	7.4	200	19.8	19.1	12.0	0.12	0.12	0.09

Note: Data is from AMEC GEOMATRIX (2011).

Table 4.5: Analyzed Seismic Scenarios with Corresponding PGVs and PGAs at the Elevations of Concrete Bulkheads B1 and B2

Probability	Magnitude	Distance (km)	PGV (cm/s)			PGA (g)		
			H1	H2	V	H1	H2	V
10^{-6}	5.25	10	9.0	10.9	7.2	0.52	0.61	0.44
	6.25	25	16.3	24.3	14.5	0.47	0.45	0.32
	7.4	200	22.7	22.1	14.4	0.16	0.17	0.11

Note: Data is from AMEC GEOMATRIX (2011).

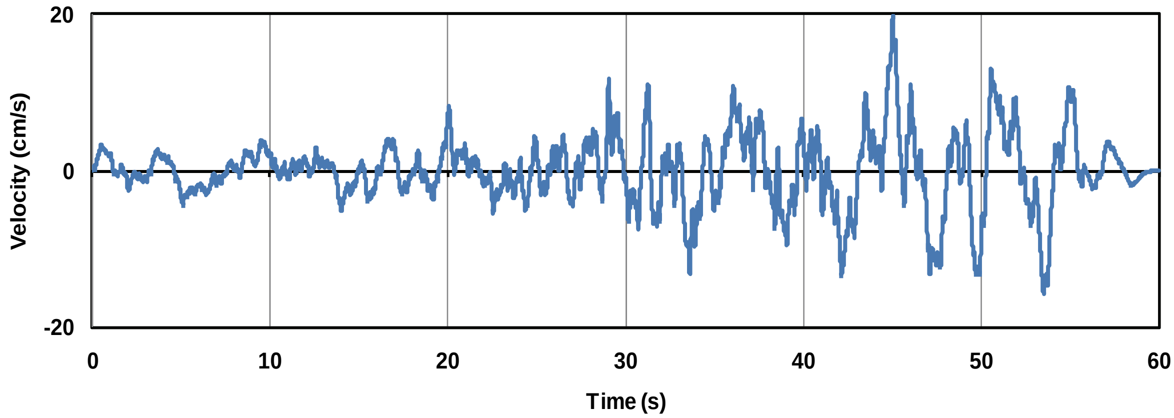

Note: Figure is from AMEC GEOMETRIX (2011).

Figure 4.11: Time History of Horizontal Velocity Component (H1) at the Repository Level for M7.4 at 200 km

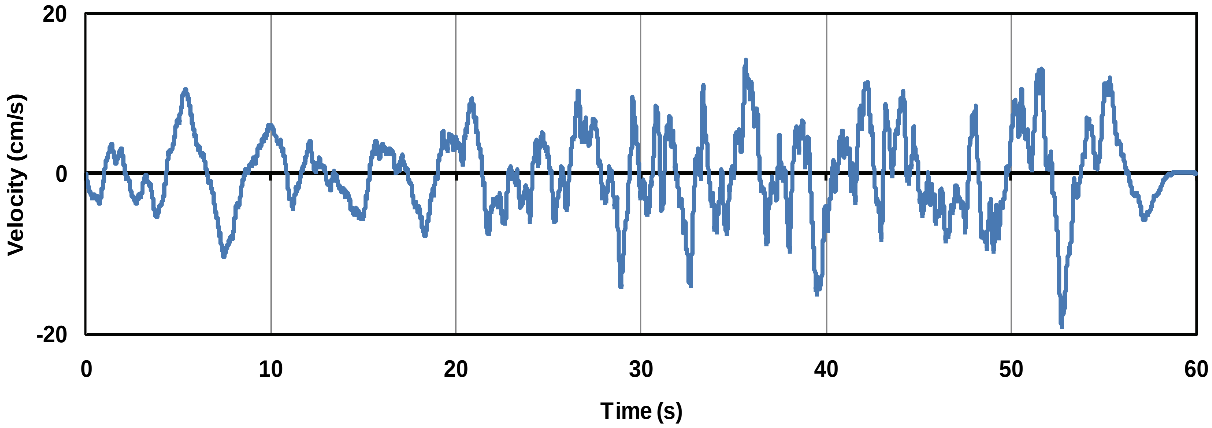

Note: Figure is from AMEC GEOMETRIX (2011).

Figure 4.12: Time History of Horizontal Velocity Component (H2) at the Repository Level for M7.4 at 200 km

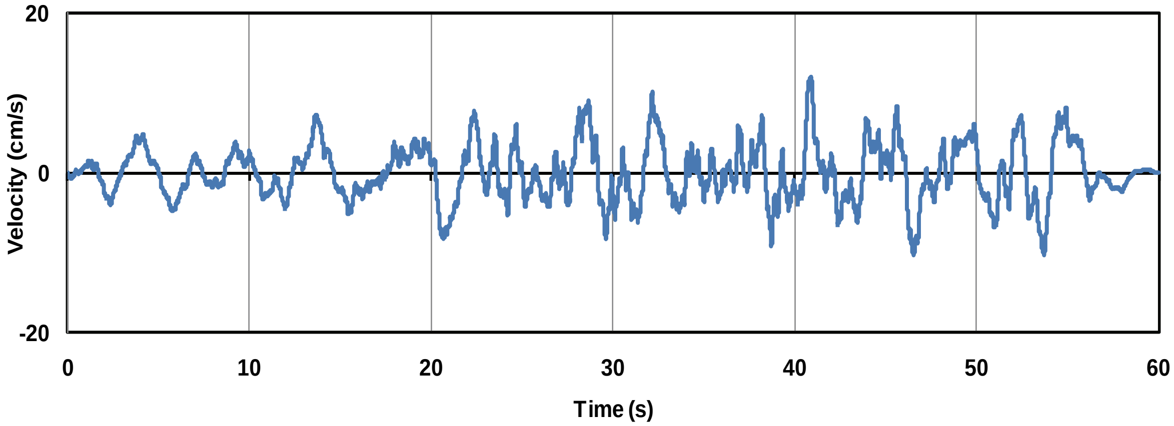

Note: Figure is from AMEC GEOMETRIX (2011).

Figure 4.13: Time History of Vertical Velocity Vomponent (V) at the Repository Level for M7.4 at 200 km

For both probability levels, the duration of two closer events (within shorter distance) is 40 s. The duration of the third event is 60 s. In order to optimize the dynamic simulations, the seismic ground motions were not simulated for their entire durations. The seismic ground motions typically start and end with lower intensity. The strong motion and majority of the energy are within the middle portion of the time histories. Thus, the simulations were conducted for the interval between the time thresholds when 15% and 85% of the Arias intensity for the entire duration, T_d , of the ground motion are accumulated. The Arias intensity, I_A, defined as:

$$I_A = \frac{\pi}{2g}\int_0^{T_d} a^2 dt \tag{15}$$

where: a is acceleration and t is time, is a measure of the energy of seismic ground shaking. The simulation interval starts at the earliest 15%-threshold and ends at the latest 85%-threshold among the three components, because there are three components of the ground motion. The calculated simulation times for the ground motions at the repository level and the elevations of the shaft concrete bulkheads are listed in Tables 4.6 and 4.7, respectively.

Table 4.6: Simulation Times for Ground Motions at the Repository Level

Probability	Magnitude	Distance (km)	Start time (s)	End time (s)
10^{-5}	5.5	20	5.11	24.06
	6.5	100	8.85	27.06
	7.4	300	22.57	49.46
10^{-6}	5.25	10	4.96	24.87
	6.25	25	8.59	28.12
	7.4	200	22.10	49.34

Table 4.7: Simulation Times for Ground Motions at the Elevations of Concrete Bulkheads B1 and B2

Probability	Magnitude	Distance (km)	Start time (s)	End time (s)
10^{-6}	5.25	10	4.91	24.97
	6.25	25	8.54	28.38
	7.4	200	22.11	49.29

In the two-dimensional analyses of the emplacement caverns, only two components (one horizontal and one vertical) of the ground motion can be analyzed. The analyzed horizontal component acts perpendicular to the cavern axis. The other, neglected horizontal component, acts in the direction of the cavern axis and, consequently, should have insignificant effect on the cavern stability. Because the orientations of the two horizontal components of the ground motions are undetermined, it is always assumed that the horizontal component with greater PGV acts perpendicular to the cavern axis. (The maximum seismically induced damage and rockfall in the underground excavations are typically well correlated to the PGV.) Consequently, at both probability levels, the horizontal component H2 is used in two-dimensional analyses for two seismic scenarios within the shorter distance (see horizontal PGVs in Table 4.4). The horizontal component H1 is used for the third, the furthest seismic scenario at both probability levels.

4.5.2 Material Damping

The geological materials (e.g., soils and rocks) dissipate energy during cyclic deformation (e.g., caused by seismic loading) at all levels of shear strain. On the other hand, the constitutive models dissipate energy only when the strains exceed the yielding strain. Energy dissipation during cycling at relatively low strain amplitudes is accounted for through material damping, which in the case of geological materials, is hysteretic, or frequency independent, and typically in the range between 2% and 5% of the critical damping. The superposition of mass- and stiffness-proportional damping, called Rayleigh damping, provides hysteretic, frequency-independent damping over a certain frequency range. The problem with the Rayleigh damping is that it imposes severe restrictions on the calculation timestep, making it more than 10 times shorter for typical damping ratios than in the case without Rayleigh damping. To avoid the excessively long simulation times and ensure that calculations are conservative, the cavern stability simulations were carried out using only local damping amounting to approximately 1.5% of the critical damping. No material damping was used in the shaft analyses.

5. CAVERN ANALYSIS

The repository layout, shown in Figure 5.1, indicates that there are two distinct scales that affect stability of the emplacement caverns and the pillars between the caverns. The scale of the pillars (17.2 m width) and caverns (8.6 m span) is much smaller than the scale of the panels (approximately 200 m span). The panel scale is important for pillar stability, because it affects the loads on the pillars within the panel, as stress arching above the panel will result in reduction of the loads on the pillars. Furthermore, the panel-scale deformations may damage the overlying cap shales, and therefore, these deformations must be investigated at the panel and repository scale.

The pillar/cavern- and panel/repository-scales were modelled separately. The models that are used for detailed investigation of cavern and pillar stability are two-dimensional, plane-strain and use Voronoi block approach with relatively small block size (~0.3 m) to discretize the pillars and rock mass below and above the caverns. Two different models were used, one representative of the caverns and the other representative of the pillars. The models include single cavern or pillar and appropriate symmetry boundary conditions along the model vertical boundaries, representing an infinitely long cavern with an infinite number of caverns extending on both sides of the analyzed cavern or pillar, because of the vertical symmetry boundary conditions. The models are representative of the caverns and pillars in the middle of the panels as indicated in Figure 5.1. The models are conservative, because stress arching above the panels is completely neglected resulting in over-estimated loads even on the most highly loaded pillars. The level of conservatism increases further for the sections approaching the panel abutments (Figure 5.1). The pillar-scale models and their results are discussed in detail in this chapter.

The panel-scale models and their results are discussed in Chapter 6. Two panel-scale analyses were carried out. Parametric stability analyses of the pillars and caverns on the panel scale were carried out in a two-dimensional model using the cross-section indicated in Figure 5.1. The model underestimates the stress arching above the panel and overestimates stresses in the pillars and potential for their failure, because of the orientation of the model plane along the longer panel axis and plane-strain approximation of the two-dimensional model. Continuum constitutive models were used to represent deformation and damage in the rocks. No time-dependent strength degradation was considered in these analyses. Instead, the long-term strength in the Cobourg limestone was assumed from the beginning of the simulations. The parametric analysis of the effect of the range of long-term strengths on degradation of the pillars and the caverns were analyzed and the results are presented in Section 6.1.

A three-dimensional panel-scale model was used to investigate the effect of panel deformation on integrity of the cap shales, and also to quantify the level of conservatism in the pillar-scale models. In these panel-scale models, only the outlines of the panels are represented. The geometry of the individual pillars and caverns is not represented explicitly. Instead, the pillars are represented with continuum material, which mechanically behaves equivalent to pillars considering the stage of their degradation due to yielding. The equivalent mechanical properties of degraded pillars are determined from the stress-strain responses of the pillar-scale models recorded during glacial cycles. The results of the three-dimensional panel-scale analyses are documented in Section 6.2.

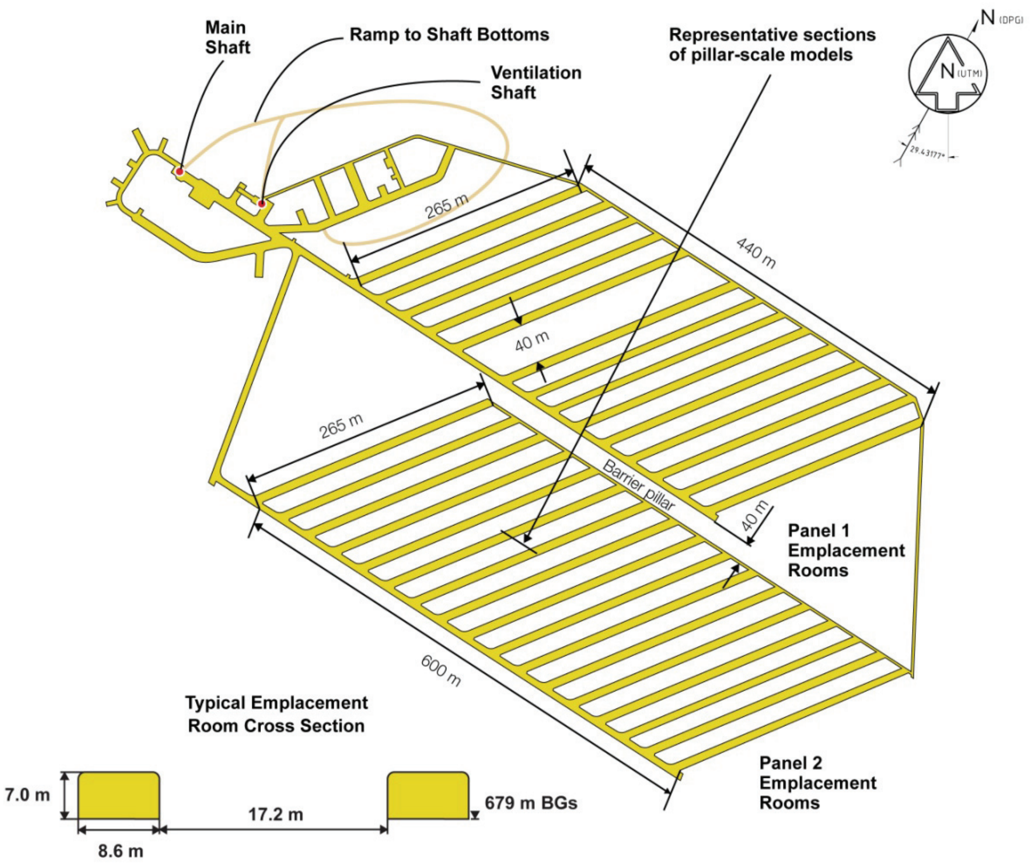

Figure 5.1: Repository Layout Showing the Location of Panel 1 and Panel 2 and Location of the Pillar-scale and Panel-scale Models

5.1 Description of Static Model

The pillar-scale analyses are carried out using numerical code UDEC Version 4.01.203 (ITASCA 2006). The typical geometries of the analyzed models for static calculations are shown in Figure 5.2. Elevations in the figures are shown as depths and, therefore, are positive values. Two geometries were considered, one representative of the caverns (left in Figure 5.2) and the other representative of the pillars (right in Figure 5.2), to ensure that the symmetry conditions applied along the vertical model boundaries do not affect the failure mode potentially preventing asymmetrical failure mechanisms. The model that primarily investigates stability of the caverns (left in Figure 5.2) includes a single cavern and half of the adjacent pillars using appropriate symmetry conditions on the vertical boundaries along the symmetry planes in the middle of the pillars. The model that primarily investigates stability of the pillars between the caverns (right in Figure 5.2) includes a single pillar with half of the widths of the adjacent caverns and symmetry conditions along the vertical model boundaries in the planes in the middle of the caverns. Asymmetrical modes of deformation, damage and degradation are possible in these models, despite symmetrical geometries and mechanical properties because of Voronoi block discretization, which is not symmetrical. Although only one cavern or pillar is included explicitly, the models, with symmetry boundary conditions, approximate typical conditions in the middle of the panels (as illustrated in Figure 5.1). These models are used for static analyses. The model geometry and boundary conditions for dynamic analysis are discussed in Section 5.2.

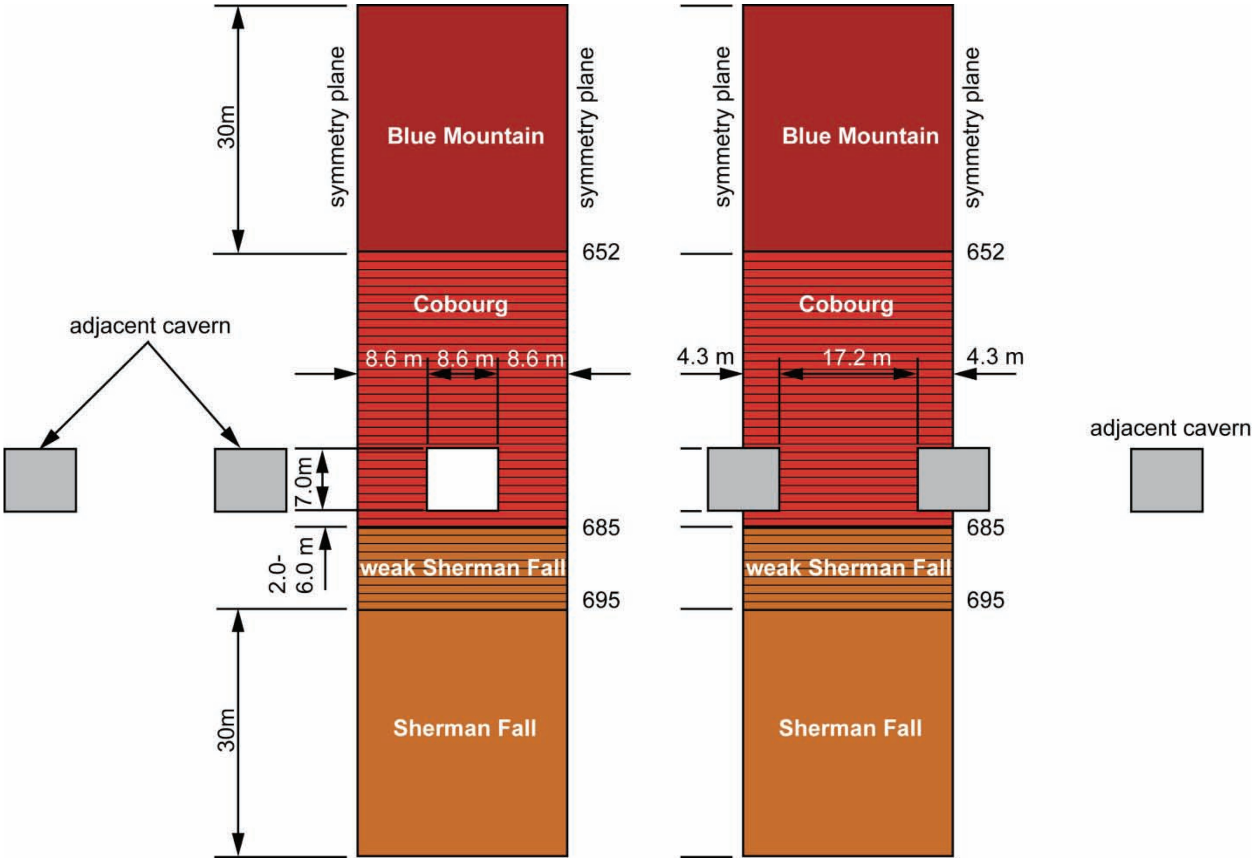

Figure 5.2: Geometry of the Cavern (left) and Pillar (right) Models

The cavern is located in the high-strength Cobourg Formation, which could provide a competent roof for the cavern. At the same time, the cavern floor typically is 6 m above the interface between the Cobourg limestone and weak Sherman Fall. The cavern design is based on OPG (2011). The caverns are rectangular shaped, 7.0 m high, and 8.6 m wide. The 250 m cavern length compared to characteristic dimensions in the cross-section, justify the use of two-dimensional approximation for the analysis. When one dimension of an underground excavation is much greater than the other two, as, for example, in case of tunnels, the deformation field, which is a plane strain in the cross-sectional plane of the excavation, is two-dimensional. The width of the pillar between the caverns (or cavern spacing) is 17.2 m.

A region extending below and above the caverns is discretized in 0.3 m large Voronoi blocks, which allow simulation of initiation and propagation of stress-induced fractures in the rock mass and formation of loose blocks. The continuum analyses showed that these areas have the greatest potential for damage and unravelling. The bedding planes are explicitly represented in the Cobourg and weak Sherman Fall at 0.75 m spacing (indicated in Figure 5.2). The thickness of the competent Cobourg limestone in the floor of the cavern is variable, because of approximately 0.6° dip of the interface between the weak Sherman Fall and the Cobourg limestones. The analyses were carried out for the thickness of the competent Cobourg limestone in the cavern floor in the range between 2 m (extremely conservative case) and 6 m (typical case).

Some of the calculations were conducted in such a way that loose blocks were deleted after their movement exceeded a given threshold (e.g., 0.25 m). This approach provided a realistic estimate of the cavern and the pillar degradation when the volume of unravelled rock is relatively small compared to the cavern volume. Block deletion significantly speeds up the numerical simulations, because simulation of loose-block free fall is very time consuming, due to much longer time scale of free-block fall compared to elastic deformation. However, in the case of complete cavern collapse, the block deletion leads to extremely conservative results, because block accumulation is the main mechanism of self-arresting the caving process (Brady and Brown 2004). Thus, in the models that resulted in complete cavern collapse, the loose blocks are allowed to unravel and accumulate on the cavern floor. In those models that resulted in cavern collapse, the degraded waste packages and waste also are represented as a 1.4 m high loose waste accumulated on the cavern floor. The loose waste height calculated based on postclosure safety assessment data (QUINTESSA and INTERA 2011).

The models do not extend vertically to the ground surface. They include the total thickness of the Cobourg Formation, where the repository is located, plus the 30 m thickness of the overlying Blue Mountain shale and the 30 m thickness of the underlying Sherman Fall Formation. The mechanical effect of the truncated portion of the rock mass above the top model boundary is represented as a dead weight, or stress boundary condition, and calculated conservatively assuming the saturated density of the entire column of rock to be 2700 kg/m^3. (The averages of the density measurements on a number of samples, as discussed in Section 3.1.1.1, are less than 2700 kg/m^3.) The bottom of the model is fixed in the vertical direction. The vertical boundaries along the symmetry planes are fixed horizontally, but left free in the vertical direction.

The initial vertical stress, σ_z, has a magnitude equal to the overburden weight:

$$\sigma_z = \rho g z \tag{16}$$

where: ρ is the rock mass density, g is acceleration due to gravity, and z is the vertical coordinate in the coordinate system, with origin at the ground surface and the positive z-axis oriented upward. Assuming that the rock mass density is 2700 kg/m^3, the vertical stress at the level of the caverns is 18.3 MPa. Although the repository has the caverns aligned with the regional orientation of the major horizontal principal stress, the initial horizontal stress state is assumed conservatively to be isotropic with a magnitude two times greater than the magnitude of the vertical principal stress. Thus, the magnitude of the horizontal stress at the repository level is 36.7 MPa.

5.2 Description of Dynamic Model

Different model boundary conditions than those described in Section 5.1 are used for the dynamic analysis of the effect of seismic ground shaking on stability of the emplacement caverns. The geometry of the model used for the dynamic analysis is shown in Figure 5.3. At the bottom and the top of the model, the viscous boundaries are applied in both normal and tangential directions. (In the static model, those boundaries are fixed.) Those boundary conditions prevent outgoing elastic waves from being reflected from the artificial model boundaries, included to make the model size finite, back into the model as would happen in the case of velocity or stress boundary conditions. Although the model does not extend to the ground surface, and viscous boundary conditions were used on the top model boundary, the effect of the ground surface is accounted for because the ground motions applied at the base of the model already include reflections from the ground surface. The seismic ground motion actually is applied as a stress boundary condition, because the viscous boundary conditions used at the model bottom are not compatible with fixed boundaries or boundaries along which velocities are prescribed. The following relation is used to calculate the stresses equivalent to velocities:

$$\begin{aligned} \tau_{vh} &= 2\rho C_s v_h \\ \sigma_v &= 2\rho C_p v_v \end{aligned} \tag{17}$$

where: τ_{vh} is the shear stress at the bottom boundary of the model, σ_v is the vertical stress, ρ is the density, C_s and C_p are S- and P-wave speeds, respectively, and v_h and v_v are horizontal and vertical particle velocities, respectively. Equation 17 is similar to a relation between velocities and the stresses for plane waves in an infinite medium. The factor of two is an added correction, because of the viscous boundaries that dissipate half of the applied energy. The free-field boundaries, shown (in Figure 5.3) as vertical bars parallel with the model vertical boundaries, represent the stresses and deformation of the truncated semi-infinite domains on the left and right sides of the model. The free fields perform simple one-dimensional wave propagation. Viscous boundary conditions also are placed between the main model domain and the free fields.

5.3 Results of Static Analyses

Although the different loading conditions (e.g., in situ stresses, time-dependent strength degradation, gas and pore pressures, glacial and seismic loading) are expected to take place concurrently, the analyses were carried out for different loading combinations in order to estimate their relative importance, but also to estimate the likely evolution of cavern states considering duration and probability of different loads.

Two sets of analyses are conducted. In the conservative bounding case, it is assumed that the long-term strength of the Cobourg limestone is 31.5 MPa and the thickness of the competent Cobourg limestone in the cavern floor is 2 m. In (also conservative) the base case, the long-term strength of the Cobourg limestone is assumed to be 45 MPa; the Cobourg limestone in the cavern floor is 6 m thick.

5.3.1 Conservative Bounding Case

The results of the long-term cavern stability analysis considering only the in situ stresses and time-dependent strength degradation are shown in Figure 5.4. A number of conservative assumptions are used in this model, including: (1) Cobourg limestone lower-bound long-term strength of 31.5 MPa compared to a measured uniaxial compressive strength of 111.3 MPa (Table 3.1), (2) only 2 m thick competent Cobourg limestone in the cavern floor, (3) all lose blocks are deleted when their vertical displacement exceeds 0.25 m and (4) the waste packages inside the caverns are not represented (i.e., the caverns are empty).

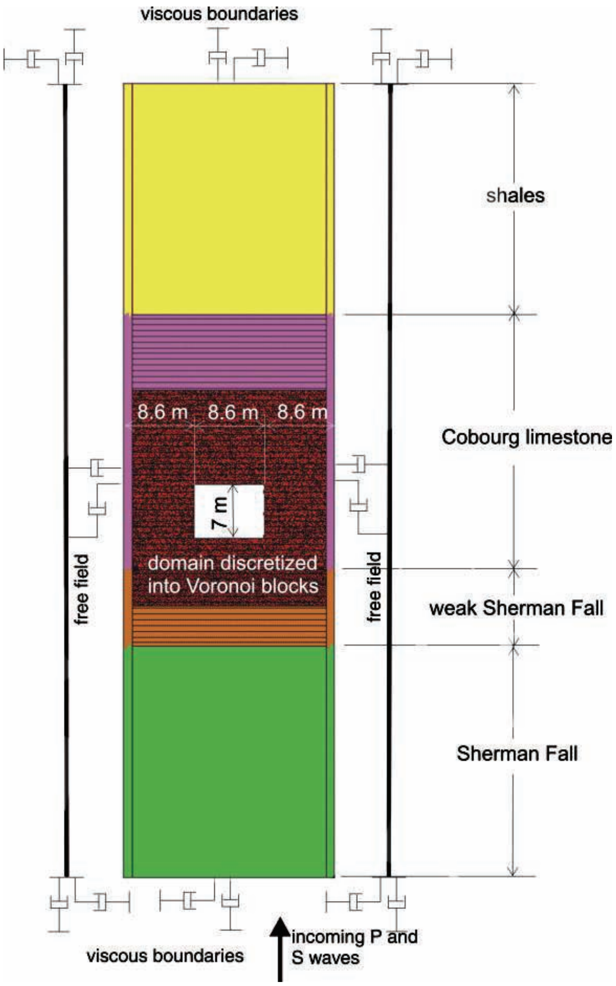

Note: Colors correspond to different model materials (as denoted in Figure 5.2).

Figure 5.3: Geometry and Boundary Conditions of the Model Used in Dynamic Analysis

The results indicate gradual degradation of the cavern rock mass. The depth of block-removal in the crown increases to approximately 6 m after 1 Ma. However, the cavern walls remain in a reasonably good condition. The floor buckles after approximately 100 years, but that does not affect stability of the walls or the crown.

The analysis shown in Figure 5.4 is conducted for dry conditions. However, the formations are saturated under in situ conditions, close to hydrostatic state corresponding to water head in Lake Huron. The results of the cavern stability analysis, which include the effect of the gas and water pressure in the cavern and rock as discussed in Section 4.3, are shown in Figure 5.5. The model indicates that when both pressures in the cavern and in the rock formation are considered, the conditions of cavern stability compared to the dry conditions initially are worse, but then improve for times longer than 100 years. The main reason for more stable conditions at later times is the confining effect of the gas pressure inside the cavern, which increases with time. Thus, it appears that the effect of the pore pressure generally is not significant.

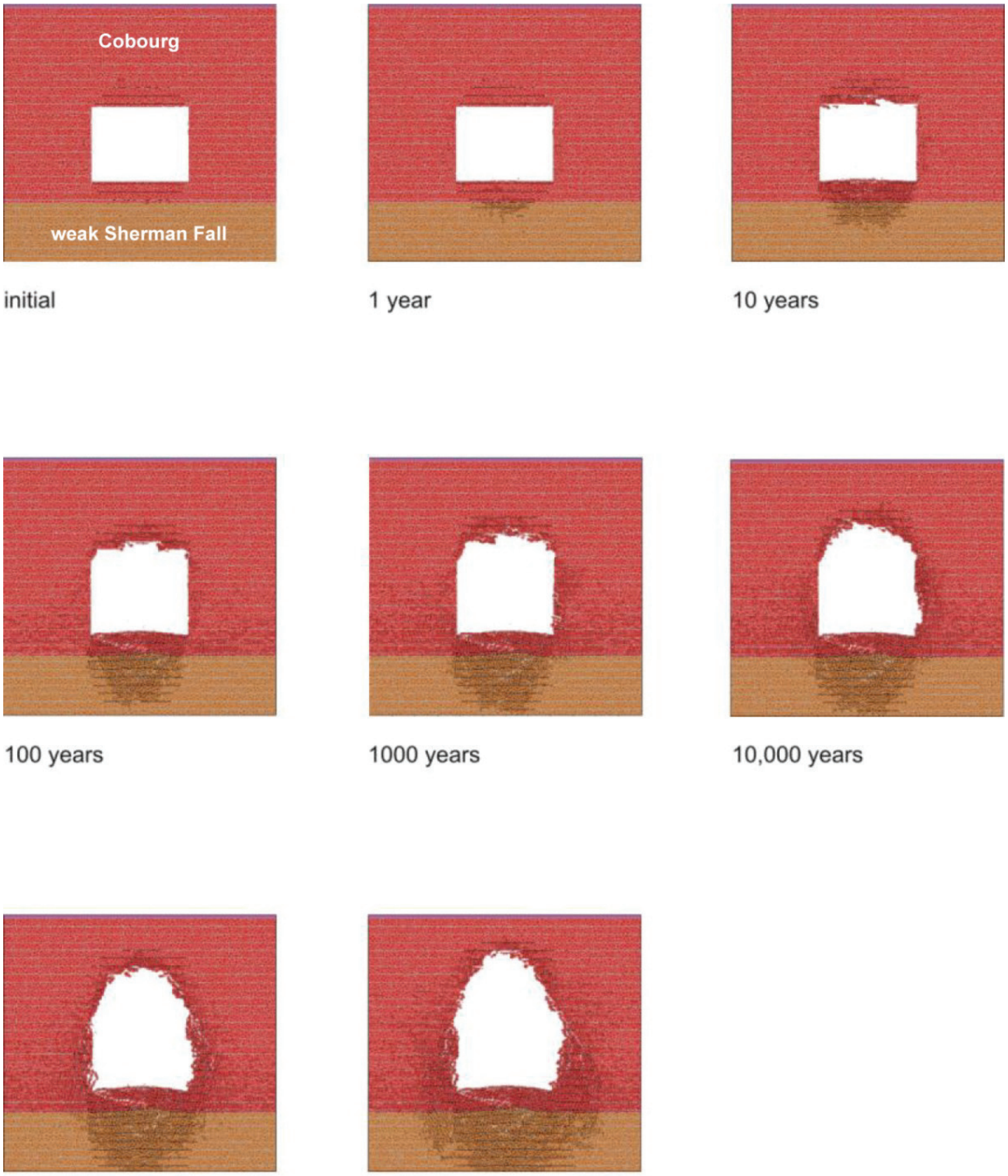

initial

1 year

10 years

100 years

1000 years

10,000 years

100,000 years

1,000,000 years

Notes: Different colors represent different regions of the model. Cobourg limestone is pink; Cobourg limestone discretized into Voronoi blocks is red; weak Sherman Fall limestone discretized into Voronoi blocks is brown. Black lines represent location of the fractures. Model parameters: Model-UCS 90 MPa; long-term strength 31.5 MPa; 2 m thick Cobourg in the floor (invert at 683 mBGS); deletion of loose blocks; caverns empty. Loading conditions: time-dependent strength degradation; dry conditions; no glacial load; no seismic load.

Figure 5.4: Evolution of Cavern Outline and Damage of the Rock: Bounding Conservative Case

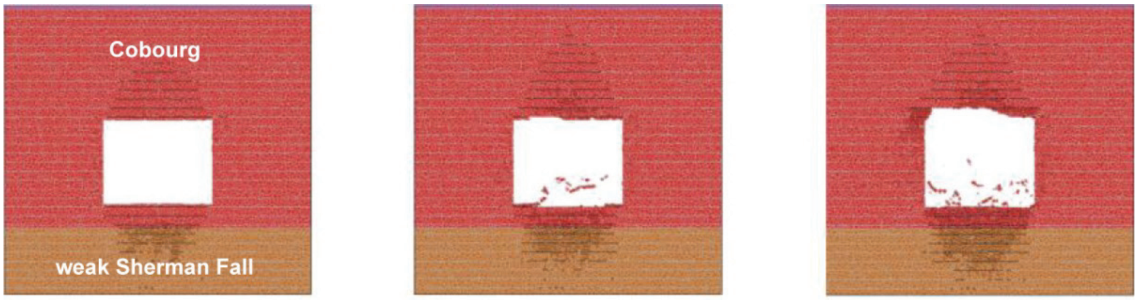

initial 1 year 10 years

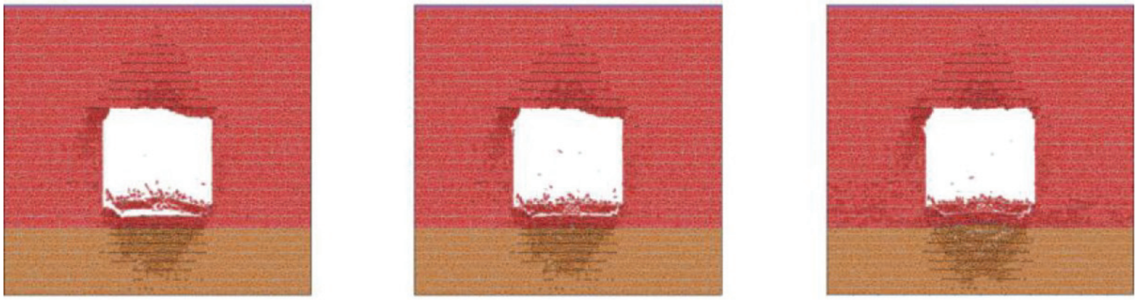

100 years 1000 years 10,000 years

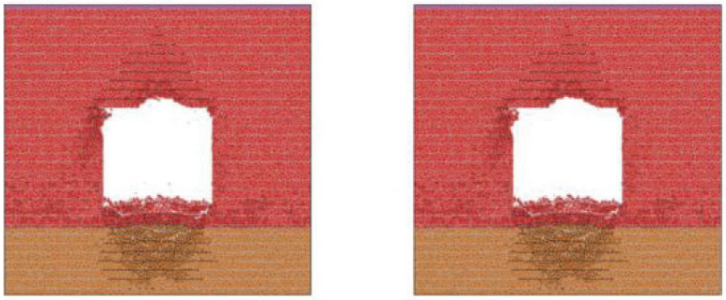

100,000 years 1,000,000 years

Notes: Different colors represent different regions of the model. Cobourg limestone is pink; Cobourg limestone discretized into Voronoi blocks is red; weak Sherman Fall limestone discretized into Voronoi blocks is brown. Black lines represent location of the fractures. Model parameters: UCS 90 MPa; long-term strength 31.5 MPa; 2 m thick Cobourg in the floor (invert at 683 mBGS); deletion of loose blocks; caverns empty. Loading conditions: time-dependent strength degradation; gas and pore pressure; no glacial load; no seismic load.

Figure 5.5: Evolution of Cavern Outline and Damage of the Rock: Bounding Conservative Case for Gas and Pore Pressures

The stability of pillars subject to two glacial cycles concurrently with time-dependent strength degradation also was analyzed. The glacial load is represented by the vertical pressure history (Section 4.4) lasting approximately 20,000 years with maximum of 30 MPa. The potential glacially-induced shear stresses are neglected, being relatively small. The first glacial cycle is assumed to start after 60,000 years, with peak vertical load at 67,200 years. The second glacial cycle is assumed to start after 100,000 years, with peak at 107,200 years. In the analysis of the effect of glacial load on pillar stability, the unravelled rock is allowed to accumulate as rubble on the cavern floor. The degraded waste and waste packages are also represented in the model as a loose, frictional material, accumulated to a 1.4 m height above the cavern floor. The results of analysis using conservative assumptions of the Cobourg limestone long-term strength of 31.5 MPa and 2 m thick competent Cobourg limestone in the cavern floor are shown in Figure 5.6. This model predicts that at the end of the first glacial cycle (e.g., 100,000 years), the pillars between the caverns are damaged completely. At the peak of the second glacial cycle (107,200 years), the caverns are filled with rubble. As it fails and unravels into the caverns, the rock bulks and eventually fills the caverns, preventing further damage and propagation of breakout. Thus, for this bounding conservative scenario, the model predicts that the caverns will be open for almost 100,000 years. However, even after cavern collapse, the collapsed rock bulks and fills the cavern, and the rock mass around the repository reaches a stable configuration. After filling the caverns with bulked rock mass, further expansion of the caved and damaged regions is arrested. Figure 5.7 and Figure 5.8 indicate that the cave, due to cavern collapse, propagates approximately 10 m above the cavern crown, which is still 15 m below the interface between the Cobourg limestone and the Blue Mountain shale (652 mBGS). Even in these conservative bounding analyses, the potential cavern collapse does not propagate to the interface between the Cobourg limestone and the cap rock.

5.3.2 Base Case

The previous analyses were carried out using assumptions purposely chosen to induce wide-scale failure. The purpose of those analyses was to assess the potential extent of such failure. Analyses also were carried out using the mean value of 45 MPa for the laboratory crack-initiation stress as the equivalent long-term strength. In addition, the cavern floor was increased from 2 m to 6 m above the interface between the Cobourg limestone and weak Sherman Fall limestone. These conditions are referred to as the Base Case. The results from these analyses show that the pillar core between the caverns will remain elastic for at least two glacial cycles (Figure 5.9).

The results of the same model, in which one glacial cycle and gas and pore pressures were simultaneously considered in a coupled analysis, are shown in Figure 5.10. Comparison of the results shown in Figure 5.9 and Figure 5.10 again indicates that even in the case when the glacial loading is considered, the gas and pore pressures do not have significant effect on stability of the caverns and pillars.

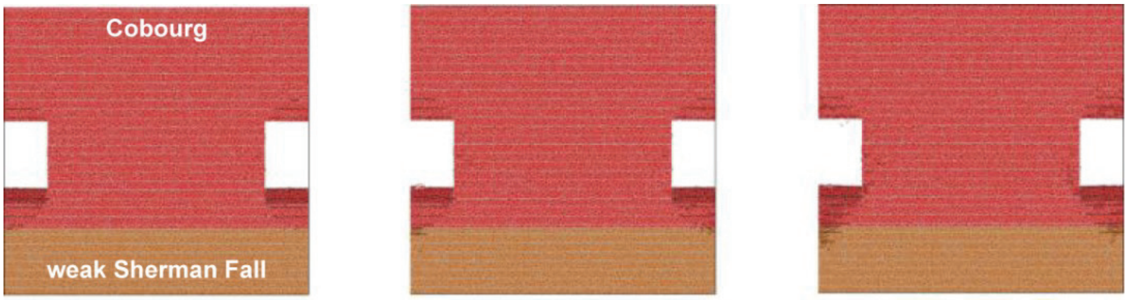

initial 1 year 10 years

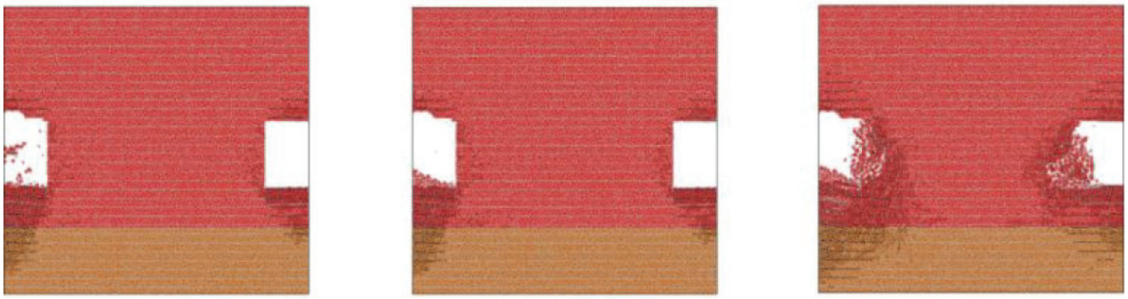

1000 years 60,000 years 67,200 years

100,000 years 107,200 years 1,000,000 years

Notes: Different colors represent different regions of the model. Cobourg limestone is pink; Cobourg limestone discretized into Voronoi blocks is red; weak Sherman Fall limestone discretized into Voronoi blocks is brown. Black lines represent location of the fractures. Model parameters: UCS 90 MPa; long-term strength 31.5 MPa; 2 m thick Cobourg in the floor (invert at 683 mBGS); accumulation of loose rubble; degraded waste and packages represented as 1.4 m high frictional material. Loading conditions: time-dependent strength degradation; dry conditions; 1st glacial cycle started at 60,000 years and reached its peak at 67,200 years; 2nd cycle started at 100,000 years and peak at 107,000 years; no seismic load.

Figure 5.6: Evolution of Cavern Outline and Pillar Damage: Bounding Conservative Case for Two Glacial Cycles

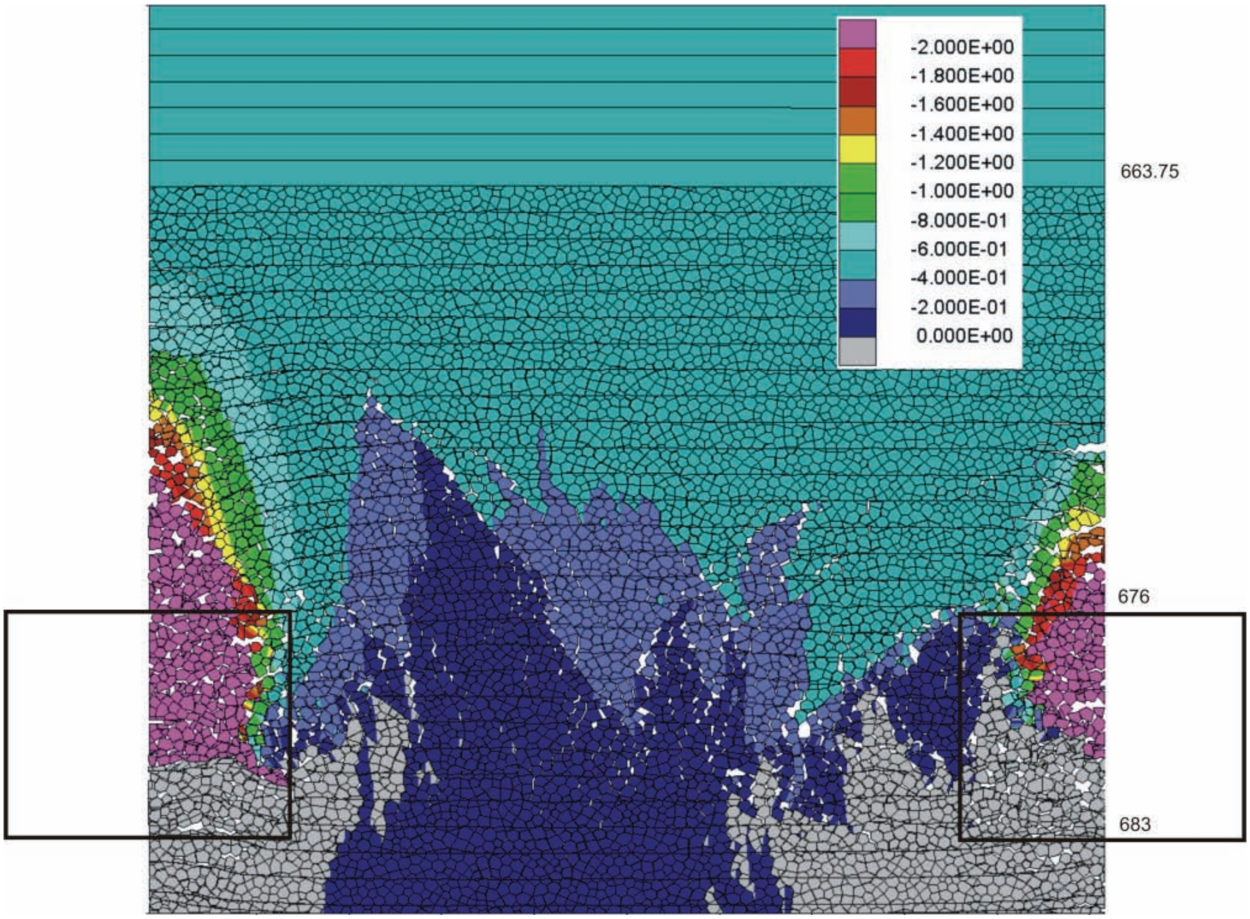

Notes: The rectangles indicate the original cavern configurations (before deformation and collapse). Depths of characteristic points are indicated on right. The total displacements include the displacement of the far field due to compaction of rock and additional displacement due to deformation and damage of the pillars. Depths are expressed as mBGS.

Figure 5.7: Total Displacement Contours (m) after Collapse of the Caverns after Two Glacial Load Cycles: Bounding Conservative Case

The base-case model was further subjected to multiple glacial events until the model reached a steady state (i.e., the additional glacial cycles did not result in additional damage). The results are illustrated in Figure 5.11 and show the extent of yielding at the peaks of the glacial loads and after the complete unloading for each glacial event. For the base-case, the caverns collapse after three glacial events, each with the maximum vertical stress of 30 MPa. During the collapse, the unravelled rock mass increases in volume as a result of large displacements and rotations, fills the caverns, and arrests further damage and unravelling of the rock mass. Comparison of the damage after the third and fourth cycles indicates no additional damage increase, confirming that future glaciations will have no additional effects on damage of the rock around the caverns. In these base-case analyses, the extent of damage is contained completely within the Cobourg limestone.

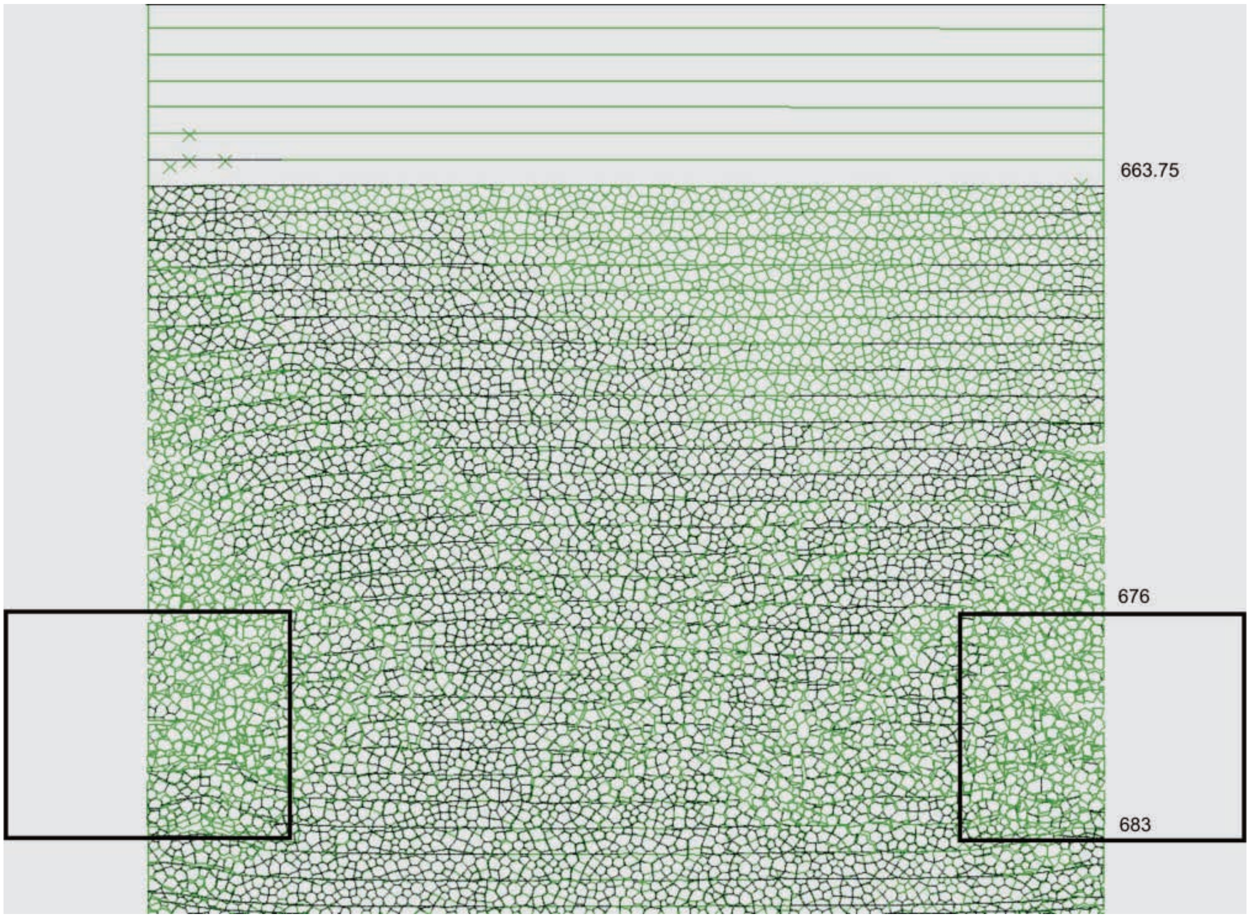

Notes: The rectangles indicate the original cavern configurations (before deformation and collapse). Depths of characteristic points are indicated on right.

Figure 5.8: Fracture Zone (black) Contained Within Cobourg Formation at Point of Complete Filling of Cavern Void: Bounding Conservative Case

On the pillar scale, the collapse of the caverns does not affect the integrity and stability of the cap rock. Damage, particularly unravelling of the rock mass, does not propagate to the Blue Mountain shales. Although the pillar-scale models are conservative with respect to stability of the caverns and pillars, (because they over-estimate the vertical load) they do not represent the strain gradients in the Blue Mountain shale as a result of deformation of the entire panel. The effect of pillar collapse on deformation of the entire panels and deformation and potential damage in the Blue Mountain shales is assessed using the panel-scale model and discussed in Section 6.2.

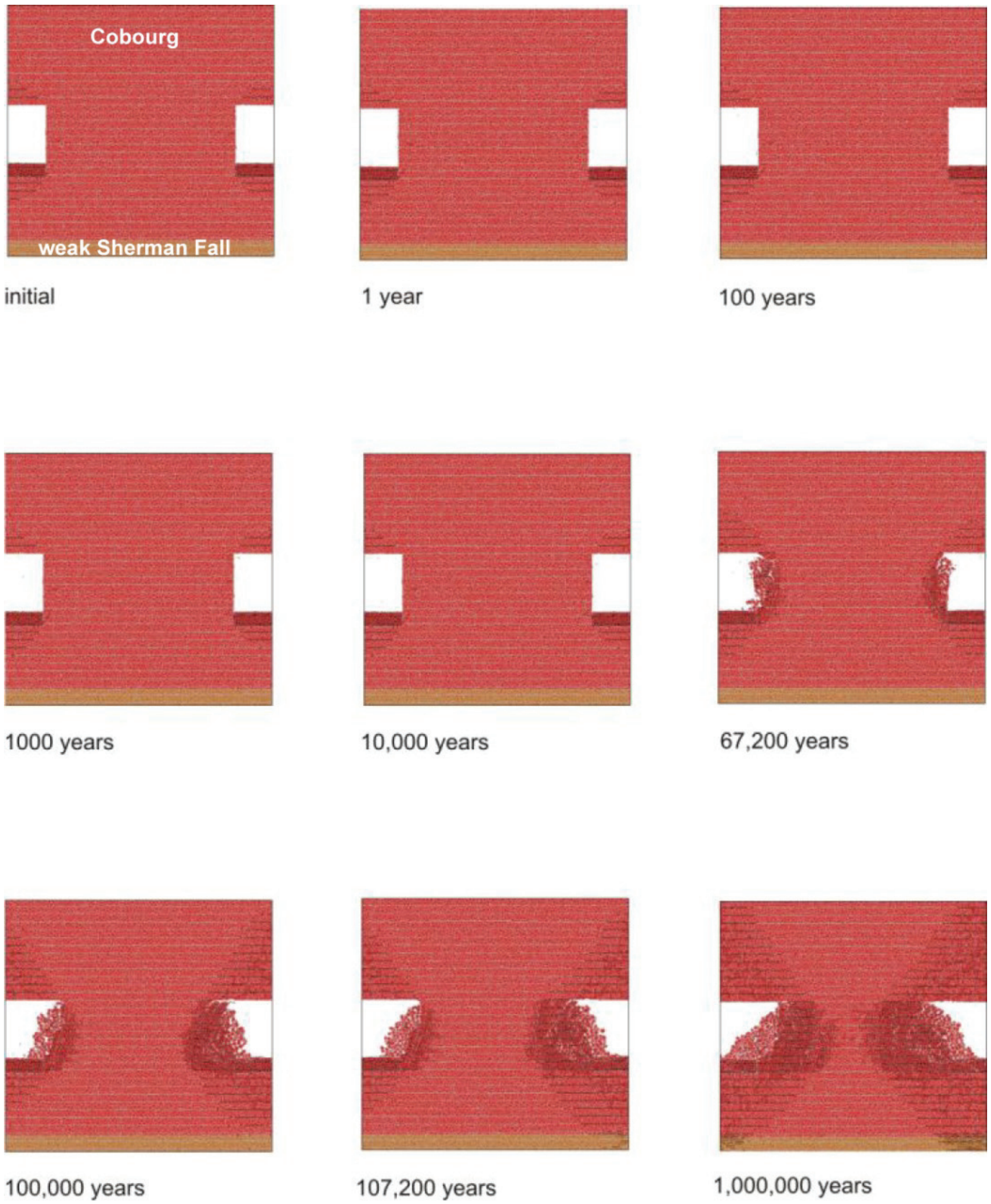

initial

1 year

100 years

1000 years

10,000 years

67,200 years

100,000 years

107,200 years

1,000,000 years

Notes: Different colors represent different regions of the model. Cobourg limestone is pink; Cobourg limestone discretized into Voronoi blocks is red; weak Sherman Fall limestone discretized into Voronoi blocks is brown. Black lines represent location of the fractures. Model parameters: UCS 90 MPa; long-term strength 45 MPa; 6 m thick Cobourg in the floor (invert at 679mBGS); accumulation of loose rubble; degraded waste and packages represented as 1.4 m high frictional material. Loading conditions: time-dependent strength degradation; dry conditions; 1st glacial cycle started at 60,000 years and reached its peak at 67,200 years; 2nd cycle started at 100,000 years and peak at 107,000 years; no seismic load.

Figure 5.9: Evolution of Cavern Outline and Pillar Damage: Representative Case for Two Glacial Cycles

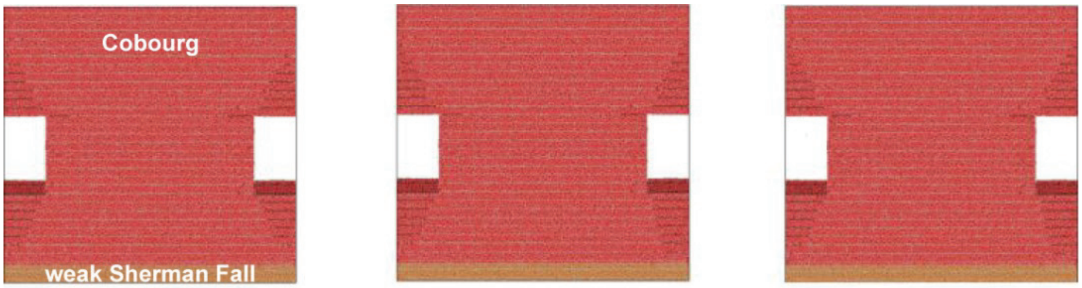

initial

1 year

100 years

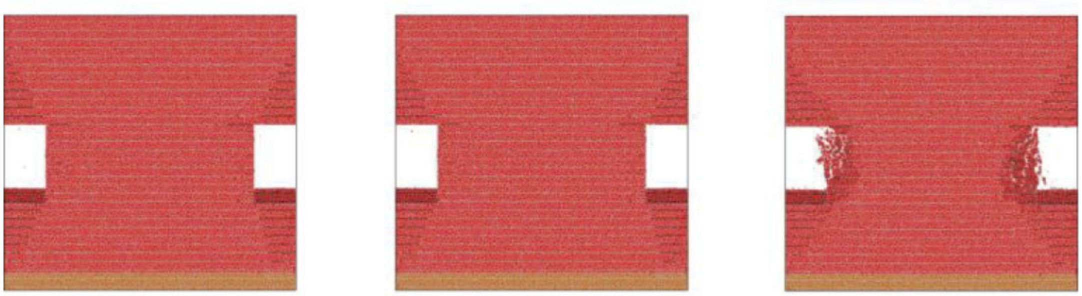

1000 years

10,000 years

69,130 years

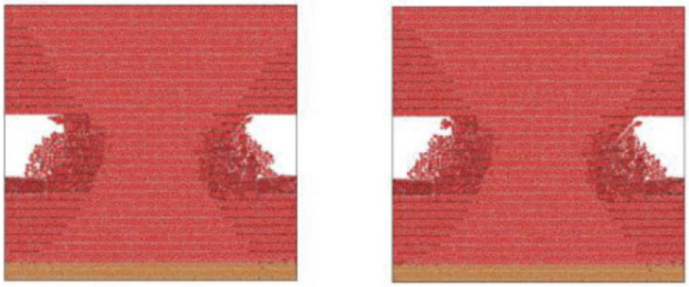

100,000 years

1,000,000 years

Notes: Different colors represent different regions of the model. Cobourg limestone is pink; Cobourg limestone discretized into Voronoi blocks is red; weak Sherman Fall limestone discretized into Voronoi blocks is brown. Black lines represent location of the fractures. Model parameters: UCS 90 MPa; long-term strength 45 MPa; 6 m thick Cobourg in the floor (invert at 679mBGS); accumulation of loose rubble; degraded waste and packages represented as 1.4 m high frictional material. Loading conditions: time-dependent strength degradation; gas and pore pressure; glacial cycle started at 60,000 years and reached its peak at 67,200 years; no seismic load.

Figure 5.10: Evolution of Cavern Outline and Pillar Damage: Representative Case for One Glacial Cycle and Gas Pore Pressure

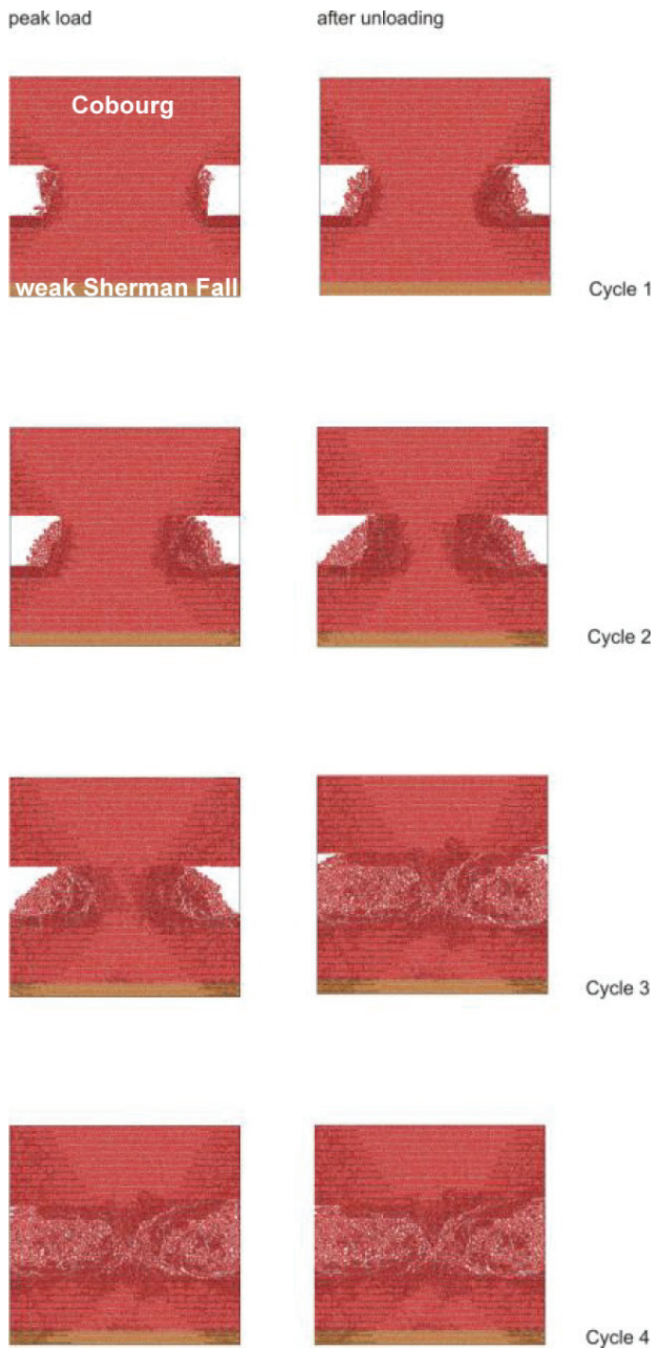

Note: Different colors represent different regions of the model. Cobourg limestone is pink; Cobourg limestone discretized into Voronoi blocks is red; weak Sherman Fall limestone discretized into Voronoi blocks is brown. Black lines represent location of the fractures. Model parameters: UCS 90 MPa; long-term strength 45 MPa; 6 m thick Cobourg in the floor (invert at 679mBGS); accumulation of loose rubble; degraded waste and packages represented as 1.4 m high frictional material. Loading conditions: time-dependent strength degradation; dry conditions; 1st glacial cycle started at 60,000 years and reached its peak at 67,200 years; 2nd cycle started at 100,000 years and peak at 107,000 years; 3rd cycle started at 200,000 years and peak at 207,000 years; 4th cycle started at 300,000 years and peak at 307,000 years; no seismic load.

Figure 5.11: Evolution of Cavern Outline and Pillar Damage: Representative Case for Four Glacial Cycles

5.3.3 Potential for Hydraulic Fracturing Due to Gas Pressure

The decaying waste will produce gas, and the build-up of this gas pressure in the caverns has the potential to open and fracture planes that are normal to the minimum principal stress. At the repository depth, the vertical stress of 18 MPa is the minimum principal stress, and therefore, the potential for hydraulically induced fracturing is greatest along the sub-horizontal bedding planes (which are planes of weakness), if the gas pressure should exceed the vertical stress of approximately 18 MPa. The gas pressure, using normal gas generation rates, is not expected to exceed 10 MPa . The results of the analyses for the normal pressure evolution scenario with updated permeabilities, or base case (shown in Figure 5.5 and Figure 5.10), do not indicate any localized fracturing typically formed during hydraulic fracturing. No horizontal fractures can be observed propagating from the cavern to distance greater than a few metres.

To demonstrate the margin with respect to the potential for hydraulic fracturing (the extreme case) when the gas pressure reaches approximately 15 MPa (Section 4.3), is investigated also. The potential for fracturing of bedding planes due to gas pressure was investigated assuming that there is no time-dependent rock strength degradation, which is the case that promotes localized deformation along the bedding planes instead of distributed damage and fracturing of the rock matrix. The full gas pressure history (Figure A), which reaches the maximum of 15 MPa, is simulated. The results of this calculation are shown in Figure 5.12. In this case, the 5 m long shear (not tensile) fractures localize along the bedding planes in the floor and in the crown of the cavern.

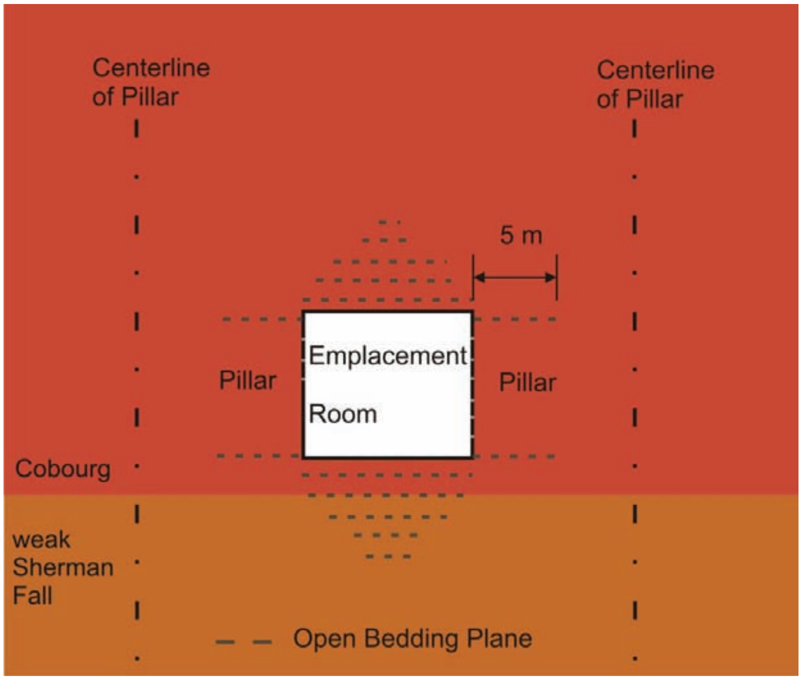

Figure 5.12: Fractured Bedding Planes Around a Cavern in the Middle of the Repository Due Gas Pressure of 15.2 MPa

5.4 Results of Dynamic Analysis

The dynamic analyses of the effect of seismic ground shaking on stability of the emplacement caverns is carried out for 6 ground motions, 3 at each 10^{-5} and 10^{-6} probabilities of annual exceedance (Section 4.5.1). The time histories at the repository level were used in the cavern stability analyses. The dynamic analyses are considered combined with in situ stresses, time-dependent strength degradation and glacial loading. The gas and pore pressure do not have significant effect on the cavern stability (Section 5.3.1), therefore they were not included in the load combinations with dynamic analysis. Three different occurrences of each seismic event are analyzed: 1) before the first glacial cycle, 2) at the peak of the first glacial cycle and 3) at the peak of the second glacial cycle. A total of 18 dynamic simulations were completed.

The results of the dynamic analyses are shown in Figure 5.13 through Figure 5.15, for cases of the seismic events occurring before the glacial loading, at the peak of the first glacial cycle and at the peak of the second glacial cycle, respectively. The seismic shaking of the considered magnitudes does not cause any additional damage or fracturing of the rock mass. That is particularly the case for the events occurring early, before glacial events when the rock mass is relatively unfractured. The seismic shaking does promote unravelling of already fractured and loose rock mass. That unravelling can cause additional fracturing of the rock mass, as a result of reduction in the confinement, but not a result of seismically induced stress change or inertial forces. Consequently, the effect of seismic shaking appears to have more effect as the area of the damaged rock mass increases, when the rock mass is subject to more glacial events. Also, it seems that the events with larger PGV (i.e., stronger events at greater distance) have more effect than the events with larger PGA (i.e., weaker events at shorter distance). An interesting observation from these simulations is that seismic shaking does not cause any instability in the cavern roof. Although the bedding planes in the roof slip, the rock matrix between the bedding planes (or within the beams formed by the bedding planes) remains predominantly elastic. If the long-term strength of the Cobourg limestone is assumed to be 31.5 MPa, the roof becomes, over time, unstable under static conditions (Figure 5.4). However, in the more realistic case of the long-term strength equal to 45 MPa, the cavern roof remains stable for 1 Ma. The results presented in this chapter demonstrate that any of considered seismic events are not expected to cause the roof collapse if the long-term strength is 45 MPa.

5.5 Summary and Discussion

The cavern stability analyses for different conditions and loads expected over the period of 1 Ma indicate that only multiple glacial events can potentially cause collapse of the emplacement caverns. In situ stresses and gas and pore pressures combined with time-dependent strength degradation cause some damage of the Cobourg limestone around the caverns and unravelling of loose rock, but it is of a limited extent and always contained within the Cobourg limestone. Even in the case of the long-term strength of 31.5 MPa (28% UCS) for the Cobourg limestone, which is the bounding conservative case, the caverns remain stable for 1 Ma when subjected to those loading conditions. The model predicts some breakouts from the crown (up to 6 m after 1 Ma) and approximately the same damage in the floor. The extent of damage in the walls is much smaller, at most 2 m. The pillar core always remains elastic. When the repository is subjected to multiple glacial cycles, the pillar-scale model with 31.5 MPa long-term strength of the Cobourg limestone predicts complete collapse of the pillars and the caverns after the second glacial cycle. The gas pressure inside the caverns and the pore pressure do not have significant effect on the damage around the caverns and the breakout depth.

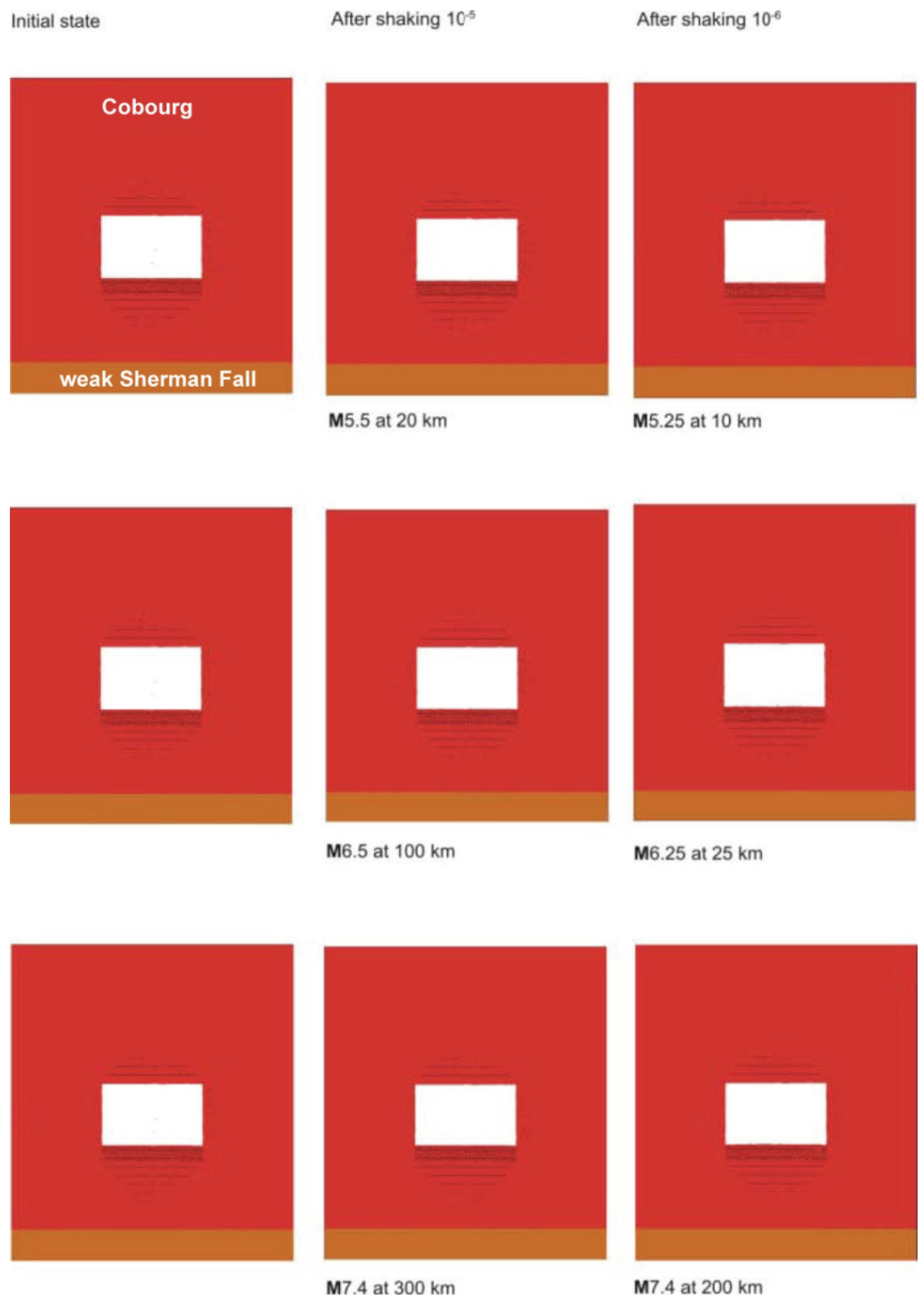

Notes: Different colors represent different regions of the model. Cobourg limestone is pink; Cobourg limestone discretized into Voronoi blocks is red; weak Sherman Fall limestone discretized into Voronoi blocks is brown. Black lines represent location of the fractures. Model parameters: UCS 90 MPa; long-term strength 45 MPa; 6 m thick Cobourg in the floor (279 mBGS); accumulation of loose rubble; degraded waste and packages represented as 1.4 m high frictional material. Loading conditions: time-dependent strength degradation; dry conditions; 1st glacial cycle started at 60,000 years and reached its peak at 67,200 years; 2nd cycle started at 100,000 years and peak at 107,000 years; seismic load.

Figure 5.13: Effect of Seismic Shaking Occurring after 60,000 Years, before the First Glacial Cycle

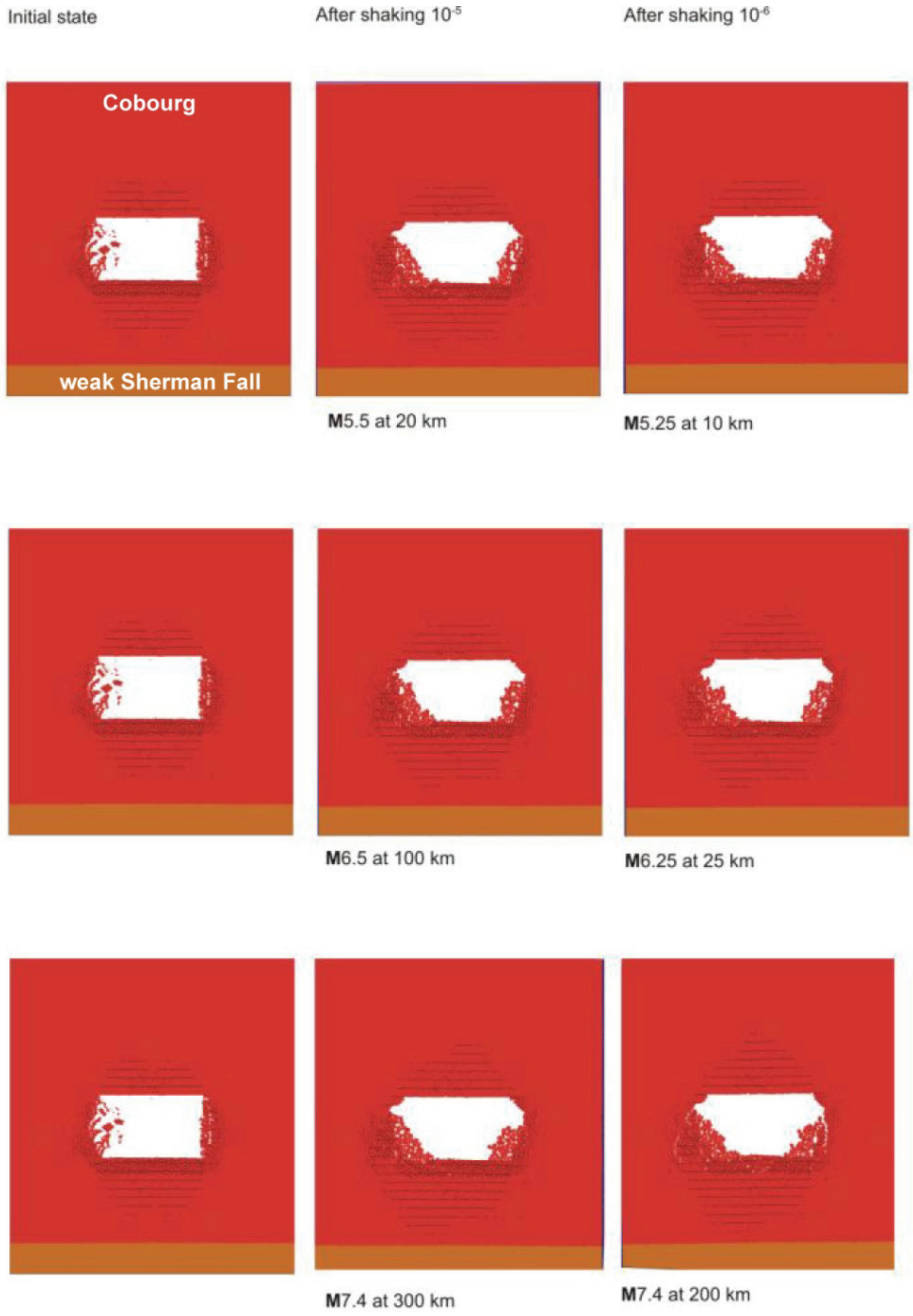

Notes: Different colors represent different regions of the model. Cobourg limestone is pink; Cobourg limestone discretized into Voronoi blocks is red; weak Sherman Fall limestone discretized into Voronoi blocks is brown. Black lines represent location of the fractures. Model parameters: UCS 90 MPa; long-term strength 45 MPa; 6 m thick Cobourg in the floor (279 mBGS); accumulation of loose rubble; degraded waste and packages represented as 1.4 m high frictional material. Loading conditions: time-dependent strength degradation; dry conditions; 1st glacial cycle started at 60,000 years and reached its peak at 67,200 years.

Figure 5.14: Effect of Seismic Shaking Occurring at the Peak of the First Glacial Cycle

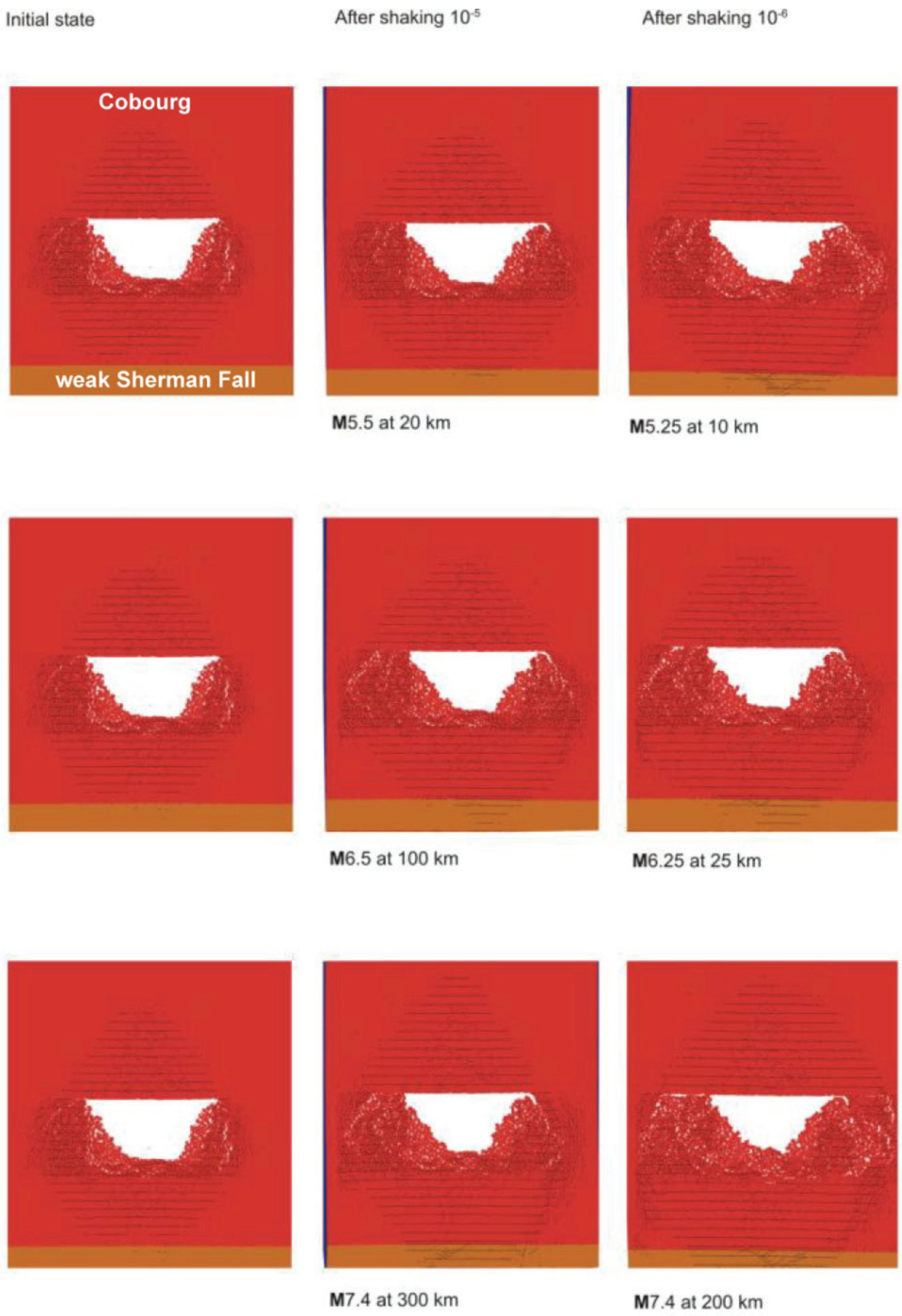

Notes: Different colors represent different regions of the model. Cobourg limestone is pink; Cobourg limestone discretized into Voronoi blocks is red; weak Sherman Fall limestone discretized into Voronoi blocks is brown. Black lines represent location of the fractures. Model parameters: UCS 90 MPa; long-term strength 45 MPa; 6 m thick Cobourg in the floor (279 mBGS); accumulation of loose rubble; degraded waste and packages represented as 1.4 m high frictional material. Loading conditions: time-dependent strength degradation; dry conditions; 1st glacial cycle started at 60,000 years and reached its peak at 67,200 years; 2nd cycle started at 100,000 years and peak at 107,000 years; seismic load.

Figure 5.15: Effect of Seismic Shaking Occurring at the Peak of the Second Glacial Cycle

Also in the conservative base case, in which the long-term strength is 45 MPa, the pillar-scale model predicts that the pillars would collapse after three glacial cycles. In all cases, when the pillar and cavern collapse is predicted, the rubble fills the cavern and arrests further propagation of the cave above the caverns. After the caverns are filled with rubble, subsequent glacial cycles do not cause increase in extent of damage, as the model reaches steady state. The maximum extent of damage does not reach the Blue Mountain shale in any of the analyzed cases.

Multiple glacial events and associated loading/unloading cycles are expected to cause failure of the pillars between the caverns and cavern collapse eventually. The number of glacial cycles that will cause the pillar collapse and timing of the pillar collapse depend on the long-term strength of the Cobourg limestone. For the Cobourg limestone long-term strength of 45 MPa, the caverns are expected to stay open for at least 100,000 years. Sensitivity of the number of the glacial cycles required to cause complete collapse of the pillars throughout the repository, considering more realistic higher long-term strengths, is investigated in Section 6.1.

The effect of the six seismic scenarios, three for each the 10^{-6} and 10^{-5} probabilities of annual exceedance, on stability of the emplacement caverns is investigated. Three ground motions match the uniform hazard spectra for each probability level. Because it was expected that the response of the emplacement cavern to dynamic shaking would depend on the magnitude and extent of damage of the surrounding rock mass, the analysis was carried out for three different initial states when the model is subjected to dynamic loading, including: 1) before the first glacial cycle, 2) at the peak load for the first glacial and 3) at the peak load for the second glacial. The analyses show that the effect of seismic loading at both probability levels is relatively small. The seismic ground shaking causes some additional unravelling of already fractured rock mass, but no new damage is predicted irrespective of the probability level of the seismic events.

6. PANEL-SCALE ANALYSES

The purpose of the analysis documented in the previous chapter was to investigate the effect of potential collapse of the pillars within the panels, which are assumed to be infinite, on integrity of the cap shales using a discontinuum modelling approach. The purpose of the panel-scale parametric analyses discussed in this chapter is to provide sensitivity analysis of the long-term pillar stability using an alternative approach. In this approach, the repository at the panel scale is modelled to capture the cavern-interaction that may occur, and to investigate the associated deformations on the overlying shales. Also, the panel-scale analysis was used to investigate the effect of stress arching over the panels after the potential pillar collapse on integrity of the cap shales.

6.1 Parametric Analysis

6.1.1 Model Description

The panel-scale parametric analysis was conducted using continuum finite difference code FLAC V.6.00.393 (ITASCA 2008). The model geometry indicating different geological units is shown in Figure 6.1. The analysis is two-dimensional in the plane of the cross-section along Panel 2 as shown in Figure 5.1. The model uses symmetry to include only one half of the panel length. The “rollers”, which represent the symmetry conditions, are applied on both vertical model boundaries. The model bottom is fixed in the vertical direction and stresses equal to the overburden weight are applied on the top. The initial vertical stress is equal to the overburden weight. The horizontal stress in the Cobourg limestone and the units below the Cobourg limestone included in the model is two times the vertical stress. The horizontal stress ratios in the cap formations included in the model (e.g., Blue Mountain shale, Georgian Bay shale, Queenston shale and Manitoulin dolostone) are consistent with horizontal stress estimates provided in Section 4.1.

Continuum Mohr-Coulomb strain-softening constitutive model was used to represent mechanical behaviour of all rock units. In addition, the bedding planes in the Cobourg limestone are represented using the continuum ubiquitous-joint model. In the model for the Cobourg limestone, the ubiquitous joint model, which represents reduced shear and tensile strengths on the bedding planes, is combined with Mohr-Coulomb strain-softening model for the intact rock between the bedding planes.

Time-dependent strength of the Cobourg limestone was degraded and assumed to be equal to the long-term strength from the beginning of the simulations irrespective of the stress state. The Cobourg limestone long-term strength values in the pillar-scale analyses (in Chapter 5), were 31.5 MPa (28% of the laboratory UCS) and 45 MPa (40% of the laboratory UCS). The 45 MPa value corresponds to the crack initiation stress measured in the uniaxial laboratory compressive tests. While Damjanac and Fairhurst (2010) suggest the crack initiation stress as a lower bound for the long-term strength of rock there is no physical evidence to suggest that actual rock strength reaches this lower bound in situ. Rock masses have sustained deviatoric stresses for tens of millions to billions of years, yet their measured strength values do not correspond to crack initiation stress. Hence, there is significant uncertainty in proposing a long-term strength for rock. In the concrete industry, the static fatigue strength of normal concrete is nominally expressed as 75% of the short term strength, while Tepfers and Kutti (1971) suggested it could range from 56% to 100% of the short term strength. To investigate the sensitivity of the predictions of cavern and pillar degradation to the assumption of the long-term strength, the parametric analysis was carried out for six values of the Cobourg limestone long-term strength:

1. 45 MPa (40% UCS);
2. 54 MPa (49% UCS);
3. 63 MPa (57% UCS);
4. 72 MPa (65% UCS);
5. 81 MPa (73% UCS); and
6. 90 MPa (81% UCS).

The analysis for 45-MPa long-term strength was conducted with both the pillar-scale discontinuum model (Section 5.3.2) and the panel-scale continuum model. The comparison of the results of two models provides a means of assessment of sensitivity of predictions to different model assumptions and approaches.

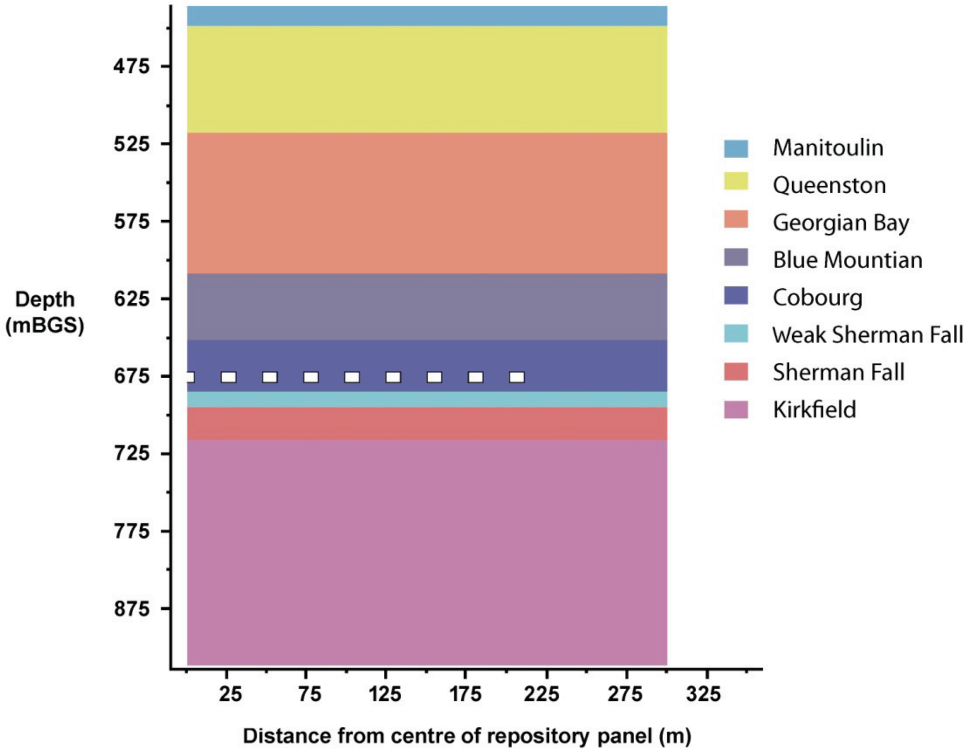

Note: The Vertical Axis is Depth Below Ground Surface in Metres and the Horizontal Axis is in Metres.

Figure 6.1: Geometry of the Model for Panel-scale Parametric Analysis

The analysis considers in situ stresses, the effect of time-dependent strength degradation as discussed in the previous paragraph and multiple glacial load cycles. The effect of gas and pore pressure is not included in this analysis because the pillar-scale analysis (Section 5.3) showed that this effect was not significant. Ten glacial cycles were simulated in each case. The Glacial load cycles are applied quasi-statically, irrespective of time, because the time-dependent strength degradation was not simulated explicitly (i.e., from the beginning of the simulation it was assumed that the strength is equal to the long-term-strength).. In each cycle, the vertical stress on the top of the model, in addition to the vertical stress due to overburden weight, is increased gradually from zero to the maximum glacial load of 30 MPa (Section 4.4) and subsequently decreased again to zero.

6.1.2 Results

The results of the parametric analyses are summarized in Figure 6.2 through Figure 6.7. Each figure shows regions of plastic deformation, where rock yields because stresses reach the yield strength, at the states before the first glacial cycle and after each glacial cycle. Considering the model symmetry, the results are shown for the 7 caverns in the middle of the repository (along the dashed line in Figure 5.1). The results for the remaining caverns are similar to those shown in the figures. Only a vertical section of the model between elevations -695 mBGS and -655 mBGS is shown in the plots, because no inelastic deformation outside that range is predicted in these models.

The prediction of the long-term response (before glacial load cycles) from the continuum panel-scale model (shown in Figure 6.2) is in a good agreement with predictions of the corresponding pillar-scale discontinuum model (Figure 5.9). Under the in situ stress conditions, the long-term strength degradation results in relatively minor fracturing of rock in both the cavern crown and the walls.

The continuum panel-scale models predict that the extent of the fractured rock mass increases with each glacial cycle. The increment of the damaged volume per glacial cycle increases with decrease in the long-term strength. However, all continuum models show that portions of the pillars between the caverns will remain elastic for at least six glacial cycles. Yielding throughout the pillars after seven glacial cycles is predicted for long-term strength of 45 MPa (40% UCS). In comparison, complete pillar failure is predicted in the pillar-scale discontinuum models after three glacial cycles (Figure 5.11). There are two reasons for difference in predictions of number of glacial cycles required for pillar collapse. The pillar-scale discontinuum model overpredicts the vertical stresses on the pillars, particularly as the pillars undergo large displacements. With increase in damage and displacements, stress arching above the panel becomes more important. The stress arching is underestimated even in the two-dimensional panel scale model, but is neglected completely in the pillar-scale model. The effects from stress arching are shown in the three-dimensional panel-scale model discussed in Section 6.2. Another reason for the discrepancy between two models is that the panel-scale model uses a continuum formulation, while the pillar-scale model utilizes discontinuum modelling approach. Although the continuum model includes strain-softening constitutive relation and representation of strength loss with plastic strain, it is not equivalent to the discrete unravelling of fractured rock mass in the discontinuum model.

Thus, considering the results of pillar- and panel-scale models, it can be concluded that if the long-term strength of the Cobourg limestone is 40% of the UCS, the pillars are predicted to fail after three to seven glacial cycles. However, if the long-term strength is 49% UCS or greater, the continuum panel-scale model predicts that pillar core will remain elastic for at least 10 glacial cycles (Figure 6.3). Considering uncertainties in the magnitudes of the peak glacial load (always assumed to be 30 MPa, i.e., the maximum load within last 120,000 years), frequency of recurrence of glacial events (Figure 4.10) and uncertainty in the long-term rock strength, the pillars and the panels are expected to be stable for at least 100,000 years. However, sensitivity analyses also show that if the long-term Cobourg strength is equal to or greater than 72 MPa (or 65% UCS), the extent of the damaged (or plastically deformed) region does not increase with glacial cycles after the first glaciation (Figure 6.5). This implies that the pillars and the emplacement caverns will remain stable for 1 Ma. If the Cobourg limestone long-term strength is equal to or greater than 81 MPa, the zone of damaged rock in the pillars remains confined to 1 m from the pillar wall. Consequences of potential pillar collapse on integrity of the cap rocks and overall performance of the repository are discussed in Section 6.2.

6.2 Integrity of Cap Rock

The vertical displacement of the Cobourg/Blue Mountain interface was tracked during multiple glacial events and at the subsequent peak glacial loads. When the long-term strength was 31.5 MPa, the maximum vertical displacement of the interface was 0.5 m, while the maximum vertical displacement increased to 0.9 m when the long-term strength was increased to 45 MPa. It is not obvious why the maximum displacement should increase when the strength is increased. However, inspection of the various analyses shows that the caverns are filled with rock blocks much earlier in the loading history when the strength is 31.5 MPa, and therefore prevents later wide-scale displacements. When the strength is increased to 45 MPa, the filling of the caverns occurs later in the loading history, and consequently more displacement has occurred already. These analyses illustrate the important role of waste packaging in controlling the maximum displacements should the ground around the cavern collapse. Regardless for the reason for the maximum displacements, in all the two-dimensional analyses the displacements are overestimated because the stress arching that occurs around multiple excavations is ignored. The three-dimensional panel-scale analysis were carried out to assess the magnitude and impact of this stress arching, and to investigate the effect of potential cavern collapse on the integrity of the Blue Mountain shale above the repository.

6.2.1 Model Description

The three-dimensional panel-scale analysis is carried out using FLAC3D Version 4.00.35 (64 bit). The geometry of the model is illustrated in Figures 6.8, 6.9 and 6.10. Isometric view of the model and the geological units included are shown in Figure 6.8. The base of the model is at 861 m depth, while the top is at 435 m (including the Manitoulin shale). Thus, the model extends at least 200 m above and below the repository level.

As shown in Figure 6.9 and Figure 6.10, two panel layouts of the repository are represented in the models: one with 20 m wide barrier pillar (Figure 6.9) and the other with 40 m wide barrier pillar (Figure 6.10). The model simulates deformation of the rock mass above the panels and the repository, therefore the rooms and the pillars are not represented explicitly. The effect of individual rooms and pillars on stresses and displacements extends above the top of the repository to a distance which is comparable to the cavern span. At greater distances there is only average, smeared effect of multiple caverns and pillars. Furthermore, after collapse of the pillars, there is no significant distinction between the pillars and the caverns, because entire repository is filled with rock blocks. Thus, in the three-dimensional panel-scale analysis after pillar collapse, the rock within the panel layout is represented as an elastic material with stiffness determined based on deformation observed in the pillar-scale model during the steady-state glacial cycle after the pillar collapse. In the model with 20 m wide barrier pillar (Figure 6.9), it is assumed conservatively that the barrier pillar also will collapse if the panel pillars collapse.

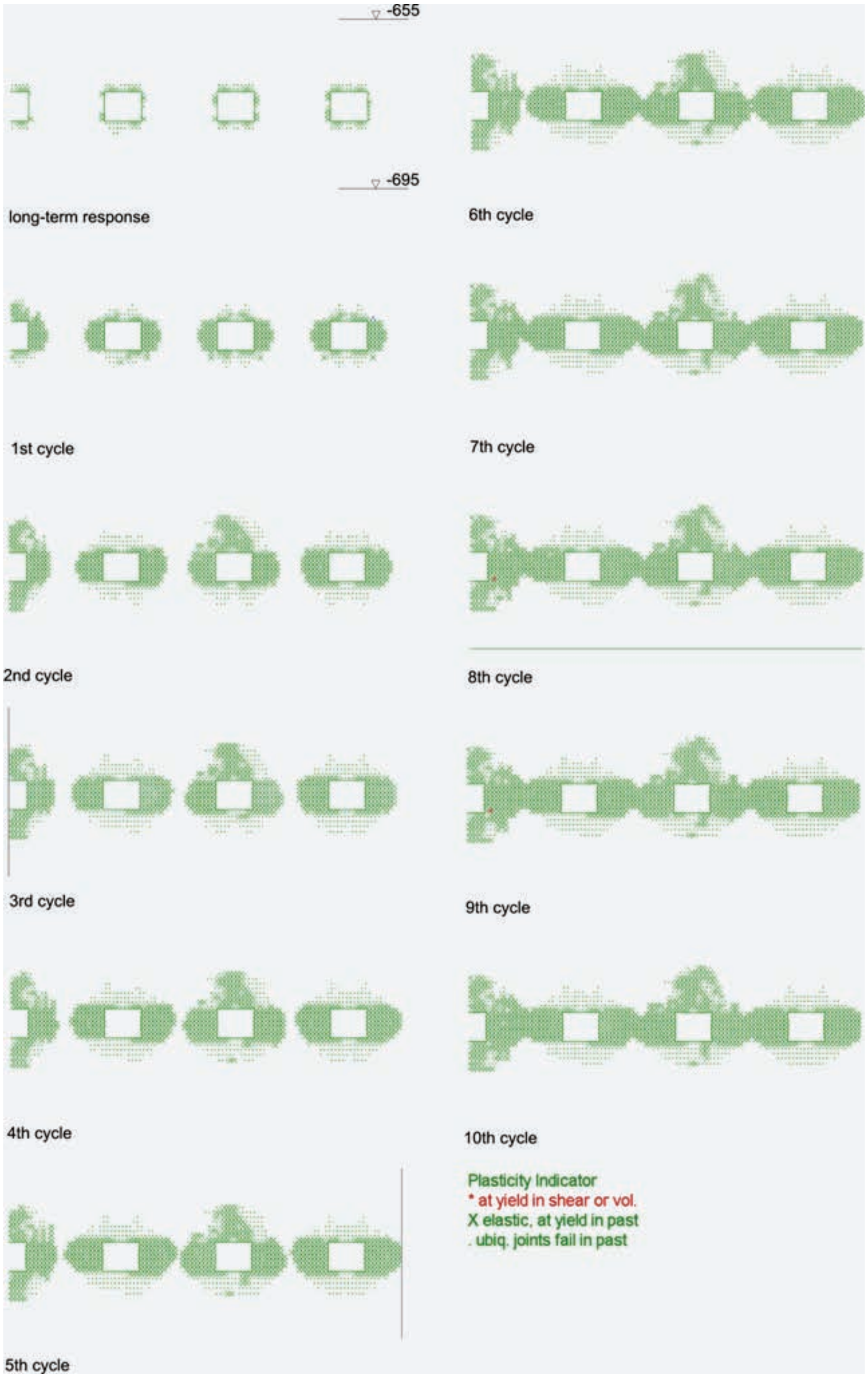

Figure 6.2: Evolution of Plasticity Around Caverns: Panel-scale Model for Long-term Strength Equal to 45 MPa (40% UCS)

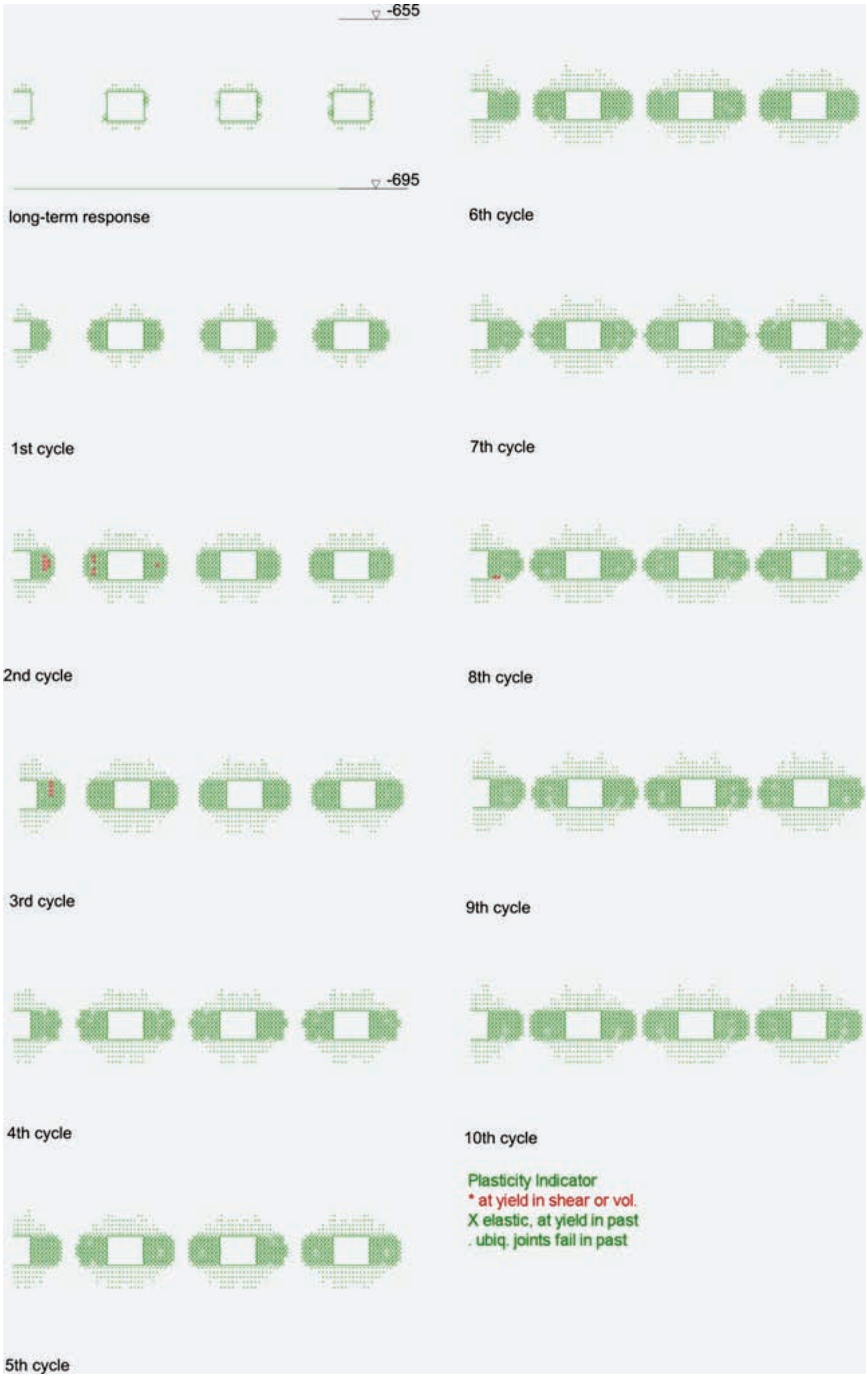

Figure 6.3: Evolution of Plasticity Around Caverns: Panel-scale Model for Long-term Strength Equal to 54 MPa (49% UCS)

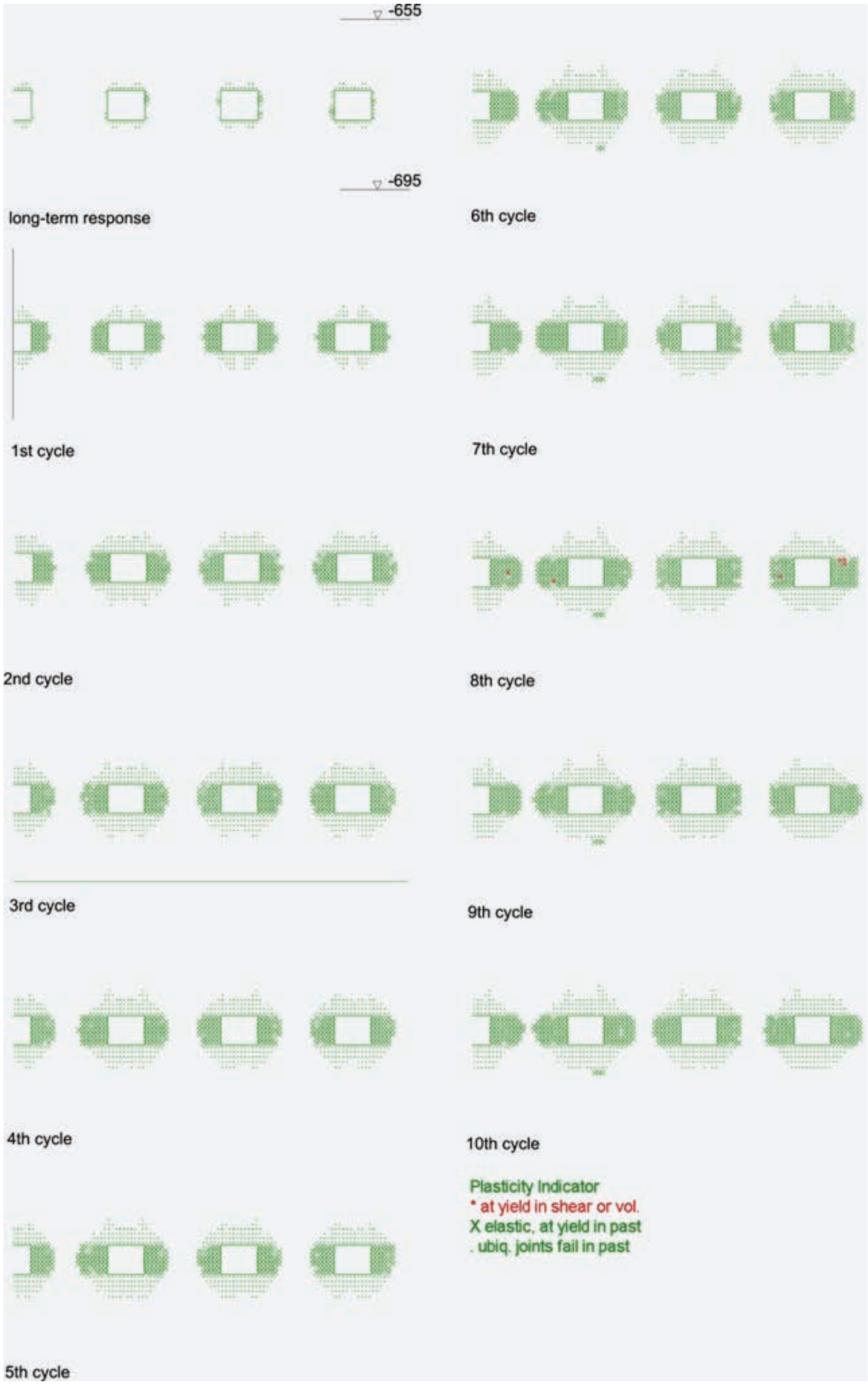

Figure 6.4: Evolution of Plasticity Around Caverns: Panel-scale Model for Long-term Strength Equal to 63 MPa (57% UCS)

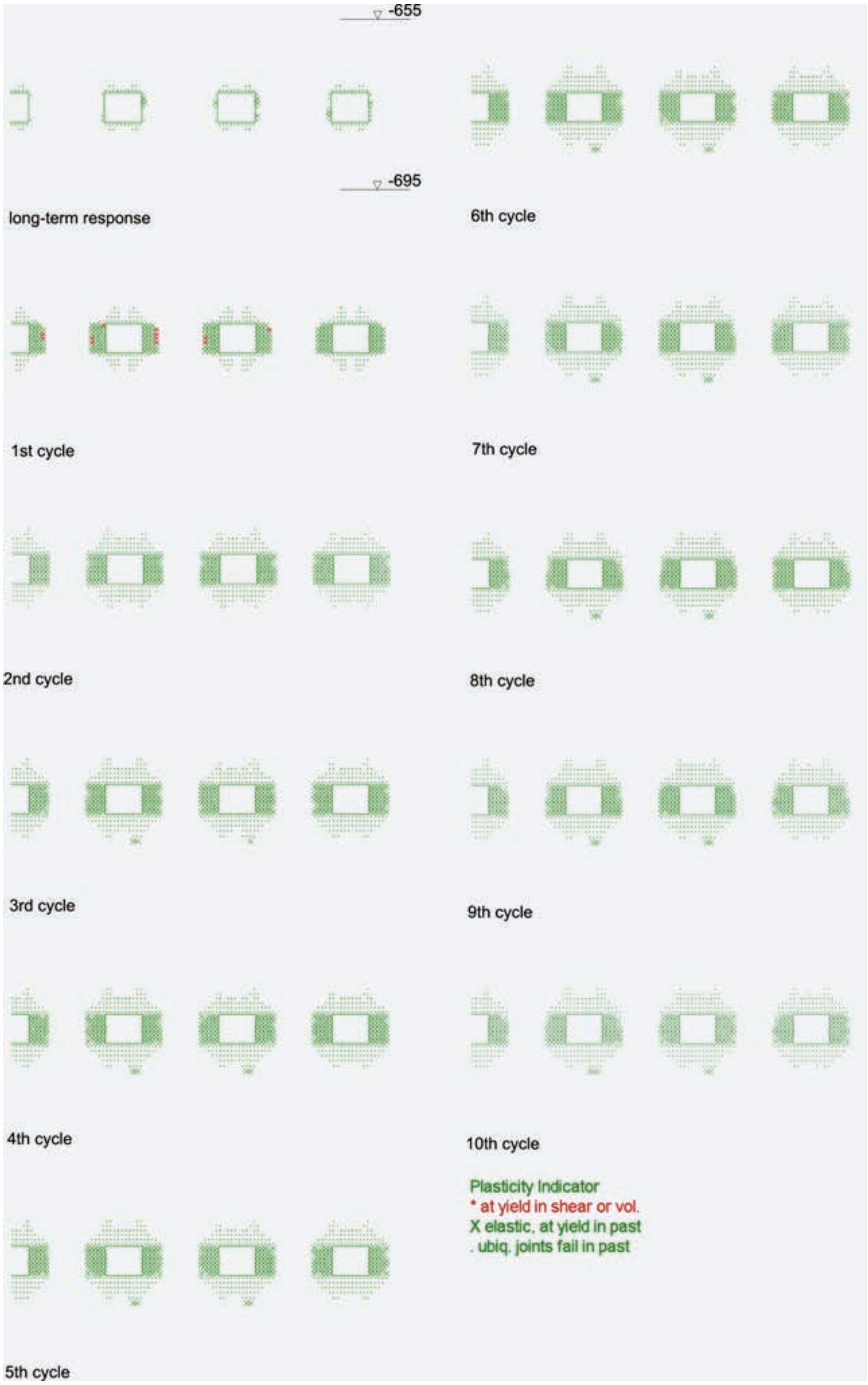

Figure 6.5: Evolution of Plasticity Around Caverns: Panel-scale Model for Long-term Strength Equal to 72 MPa (65% UCS)

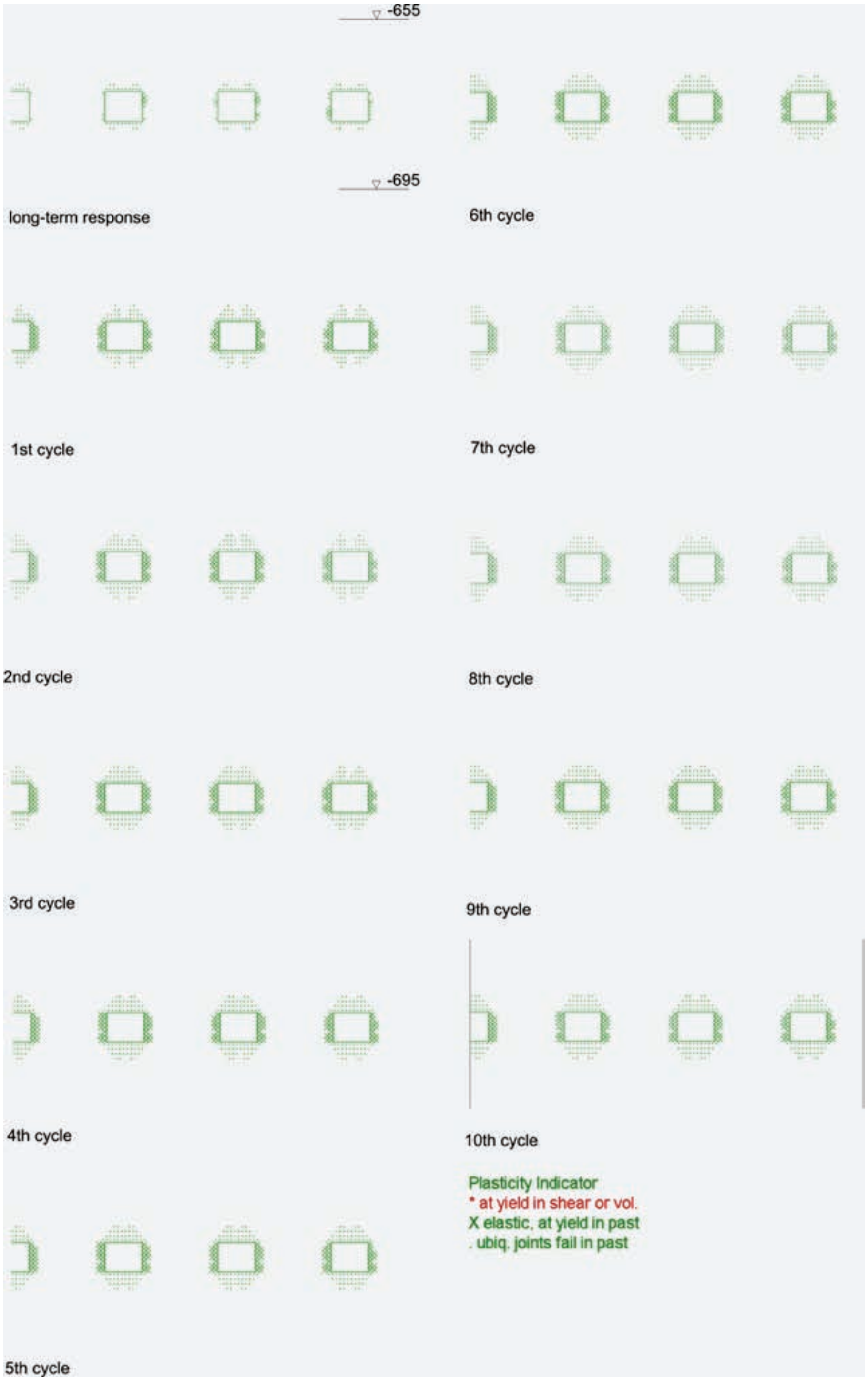

Figure 6.6: Evolution of Plasticity Around Caverns: Panel-scale Model for Long-term Strength Equal to 81 MPa (73% UCS)

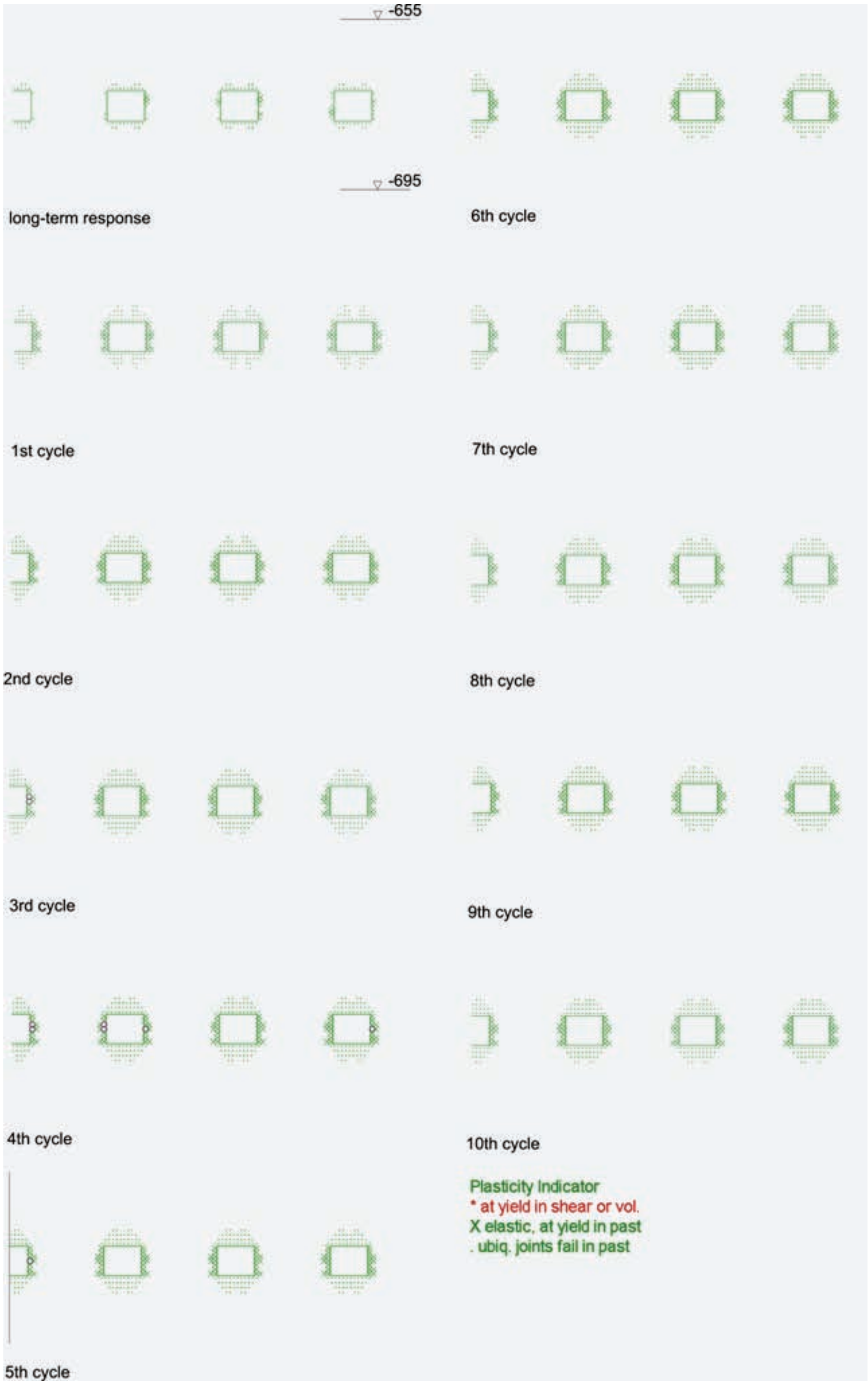

Figure 6.7: Evolution of Plasticity Around Caverns: Panel-scale Model for Long-term Strength Equal to 90 MPa (81% UCS)

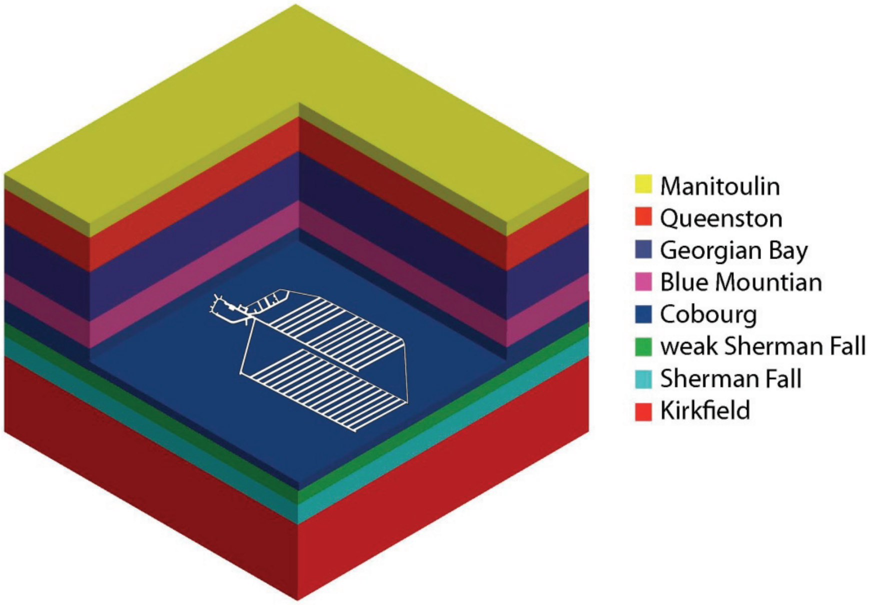

Figure 6.8: Geometry and Geological Formation Used for the Panel-scale Modelling

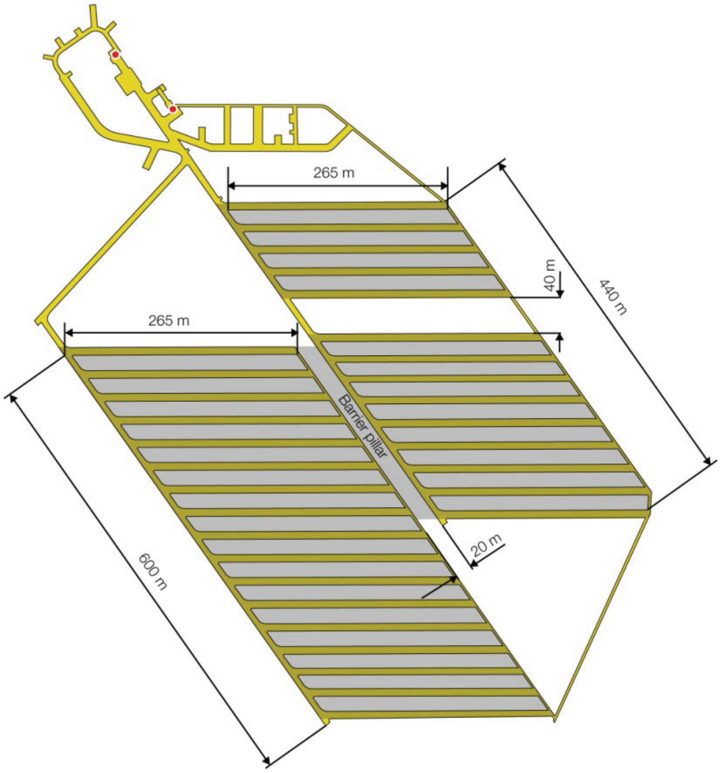

Figure 6.9: Panel Geometry in the Model (gray area) Overlain with Repository Design Layout: 20 m Wide Barrier Pillar

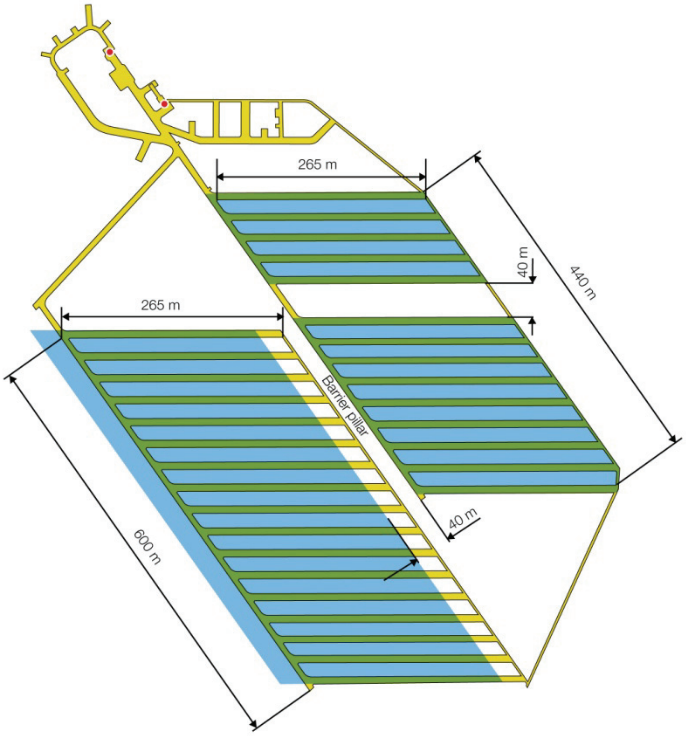

Figure 6.10: Panel Geometry in the Model (blue area) Overlain with Repository Design Layout: 40 m Wide Barrier Pillar

The stiffness, E_e, of the equivalent material within the panels after pillar collapse is estimated to be 296 MPa using the following relation:

$$E_e = \frac{H}{d_{\max}} \Delta\sigma \qquad (17)$$

where: H is the height of the equivalent material, in this case equal to 7 m repository height, $d_{\max}$ is the maximum displacement (0.85 m) from the pillar-scale models and $\Delta\sigma$ is the vertical stress increase. The vertical stress increase, which includes the additional stress due to glacial load, and the increase in the pillar stress due to excavation of the caverns under in situ stress conditions, (33% excavation ratio) is 36 MPa.

The “roller” boundary conditions are applied along the vertical and the bottom model boundaries. The stress, equal to overburden weight, is applied on the top. The vertical in situ stresses are in equilibrium with overburden weight conservatively calculated using the rock mass density of 2700 kg/m^3. The horizontal in situ stresses in the units above the Blue Mountain shale are assumed to be isotropic with magnitude equal to the minimum horizontal stress as indicated in Table 4.2. The horizontal stress ratio of 2 is assumed in the Cobourg limestone, and the units below it included in the model.

The time-dependent strength degradation for the Cobourg limestone is set to 45 MPa and is assumed to have occurred instantly from the beginning of the calculations.

The average Poisson’s ratio in the Blue Mountain shale as measured on the laboratory samples is approximately 0.1 (Table 3.1). The minimum horizontal stress ratio, k, in the Blue Mountain shale, was calculated from the FLAC3D regional in situ stress model as 0.57 (Section 4.1 and Table 4.2). The results of a simple stress change calculation (assuming uniaxial strain) for the Poisson’s ratio of 0.1 and the horizontal stress ratio of 0.57 suggest that the entire Blue Mountain shale yielded during the last glacial cycle (Figure 4.10), when the vertical stress increased to approximately 30 MPa. The cores taken from the boreholes do not reveal any evidence of yielding or damage in the Blue Mountain shale. Hence, the predicted yield using the laboratory measured Poisson’s ratio of 0.1 and the horizontal in situ stress of 0.57 does not agree with the intact quality of the Blue Mountain shales found in the site investigation program.

Simple analyses assuming uniaxial strain were carried out to assess the impact of the horizontal in situ stress ratio, and Poisson’s ratio on prediction of yielding and damage in the Blue Mountain shale. Although the laboratory test results suggest a Poisson’s ratio of 0.1, rock mass values typically range between 0.2 and 0.3. Considering that the regional in situ stress analysis neglects the effect of variation of the vertical stresses on the horizontal stresses, it is estimated that the horizontal stress ratio (k) in the Blue Mountain shale could range from 0.8 and 1.2. Sensitivity analyses were carried out for k ranging from 0.8 to 1.2 and Poisson’s ratio (ν) varying from 0.2 to 0.3. The results from those analyses, shown in Figure 6.11, suggest that in case of Poisson’s ratio equal to 0.3, the glacial loading moves the stresses in Blue Mountain shale away from the yield surface, and therefore reduces the potential of yielding.

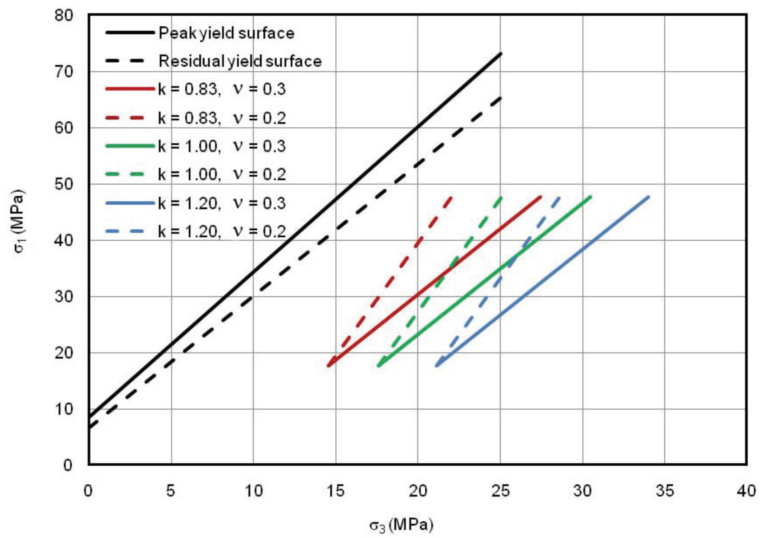

Figure 6.11: Example of the Effect of In Situ Stress and Poisson’s Ratio on Far Field Stress Paths in Blue Mountain Shale

Considering the uncertainties in the Poisson’s ratio and horizontal stress ratio, the panel-scale model was analyzed for three sets of properties (Cases 1, 2 and 3) listed in Table 6.1 that bound the range of expected conditions in the Blue Mountain shale.

Table 6.1: Three-dimensional Panel-scale Model: Analyzed Cases

Case	Poisson's Ratio	Horizontal Stress Ratio
1	0.25	0.83
2	0.3	1.0
3	0.3	1.2

6.2.2 Results

6.2.2.1 20 m Wide Barrier Pillar

The displacement contours for Case 1 are shown in a number of horizontal sections at the elevations between the geological units above the repository included in the model, but also on the top of the repository and in the vertical cross-section. The displacement contours shown in these plots are due to repository deformation and damage of the pillars. The displacements due to compaction of the far field rock subjected to the maximum glacial load are not included. Consequently, the displacements of the far field are zero. The maximum repository-induced displacement at the peak glacial load is 0.49 m for Case 1. In Cases 2 and 3, the displacement field and the maximum displacement (as illustrated in Figure 6.14 for Case 2) do not change significantly.

In Case 1, minor yielding is predicted in the regions of stress concentration above the panel abutments and above the barrier pillar within Panel 1 in the Blue Mountain shale as shown in Figure 6.13, in the plan-view at the base of the Blue Mountain shale and in the vertical cross-section. The size of the yield zone is relatively small. It extends to the middle of the Blue Mountain shale. In Cases 2 and 3, as illustrated in Figure 6.15 for Case 2, no yielding takes place in the Blue Mountain shale.

In Cases 2 and 3, no yielding or plastic deformation occurs anywhere in the model above the Cobourg limestone/Blue Mountain shale interface, even during the largest expected vertical glacial load and after complete collapse of the pillars. In the worst case, represented by Case 1 (Figure 6.13), some limited yielding, both in plan-view and vertically, is expected above the panel abutments and the barrier pillars between the panels. However, in all cases the strains in the Blue Mountain shale are relatively small (less than 0.5%) indicating that deformation, due to potential pillar collapse after multiple glacial cycles, will not change permeability of the cap rock formations significantly.

6.2.2.2 40 m Wide Barrier Pillar

The main effect of increasing barrier pillars from 20 m to 40 m is reduction in the maximum displacements from 0.49 m (Figure 6.12) to 0.44 m (Figure 6.16). However, the 40 m wide barrier pillar does not reduce the extent of yielding significantly (Figure 6.17 and Figure 6.18).

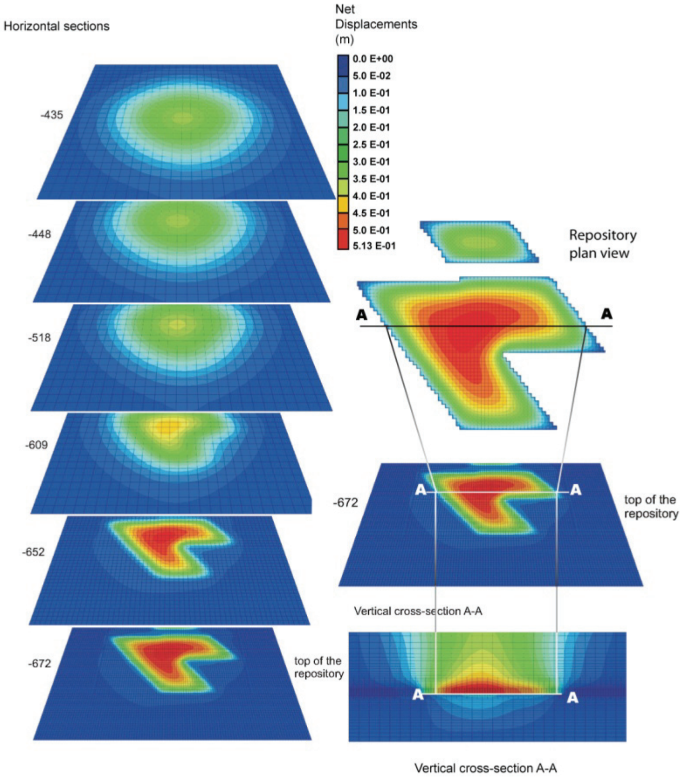

Figure 6.12: Displacements (m) at the Peak of the Glacial Load: Case 1, 20 m Wide Barrier Pillar

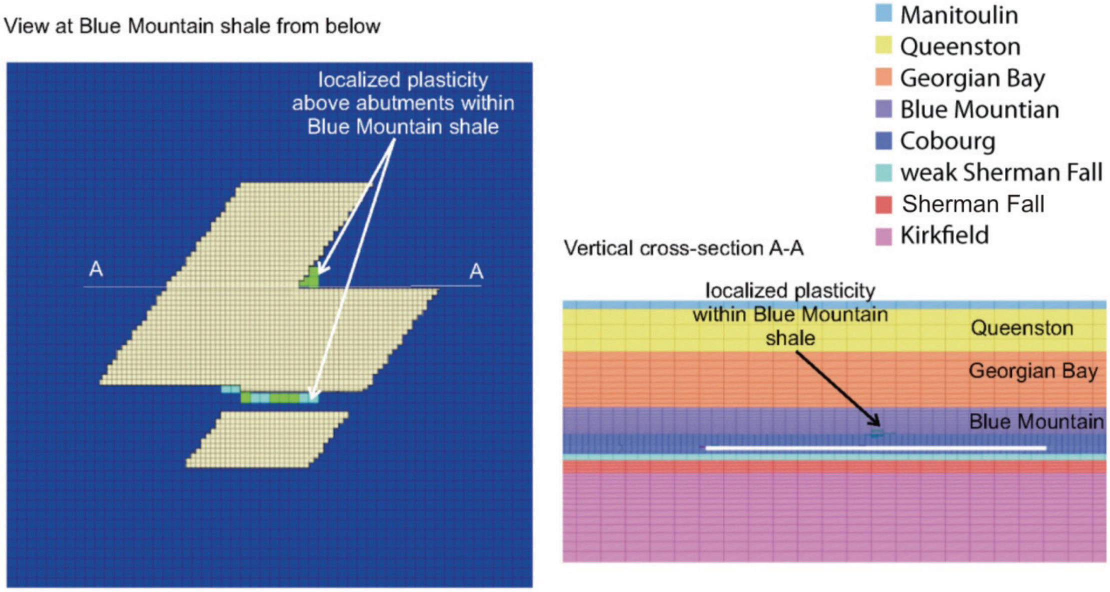

Figure 6.13: Plastic Deformation (Yielding) at the Peak of the Glacial Load: Case 1, 20 m Wide Barrier Pillar

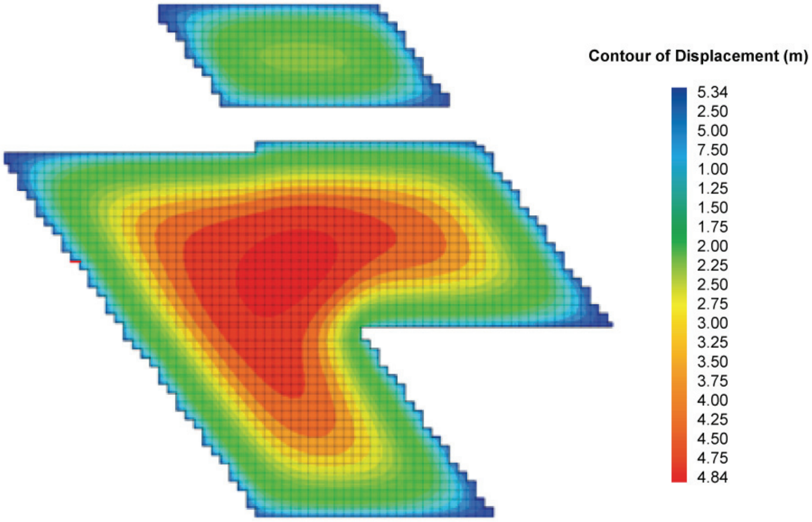

Figure 6.14: Displacements (m) of the Top of the Repository at the Peak Glacial Load: Case 2, 20 m Wide Barrier Pillar

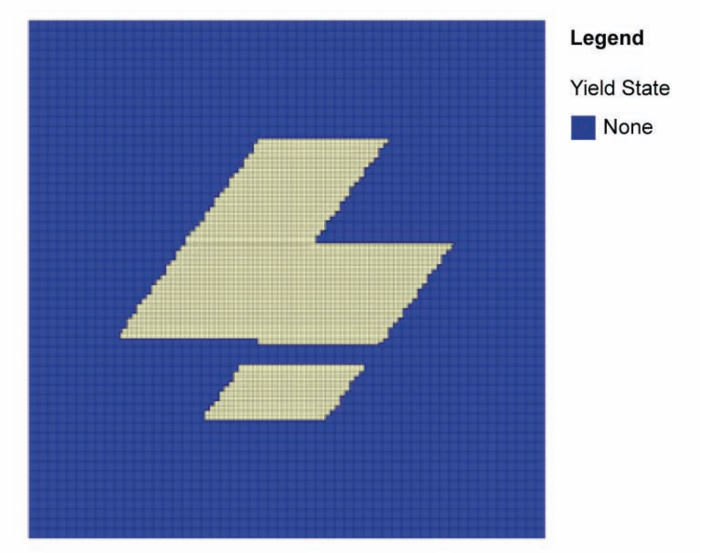

Figure 6.15: Plastic Deformation (Yielding) at the Peak of the Glacial Load: Case 2, 20 m Wide Barrier Pillar. View from Below at the Blue Mountain Shale

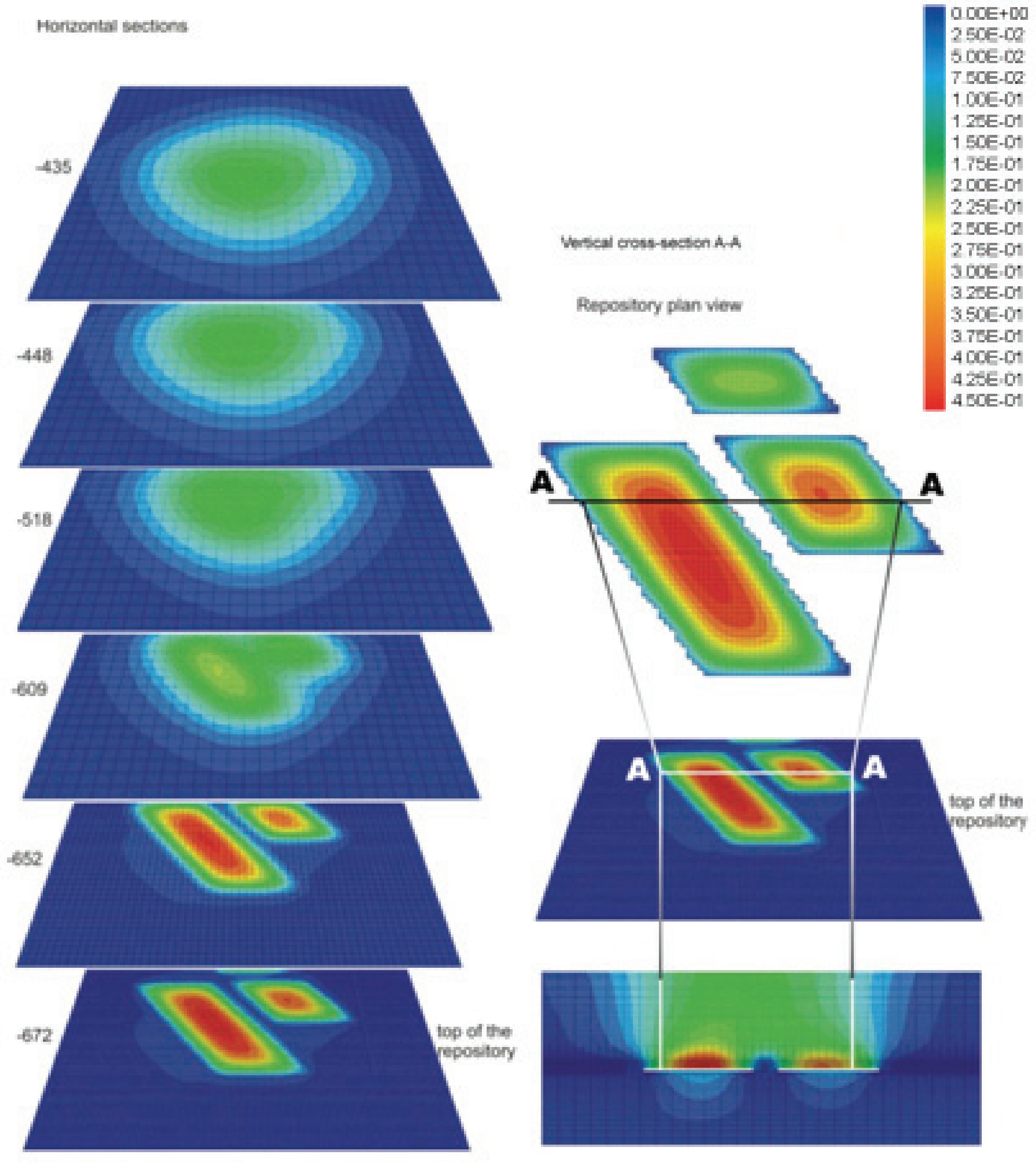

Figure 6.16: Displacements (m) at the Peak of the Glacial Load: Case 1, 40 m Wide Barrier Pillar

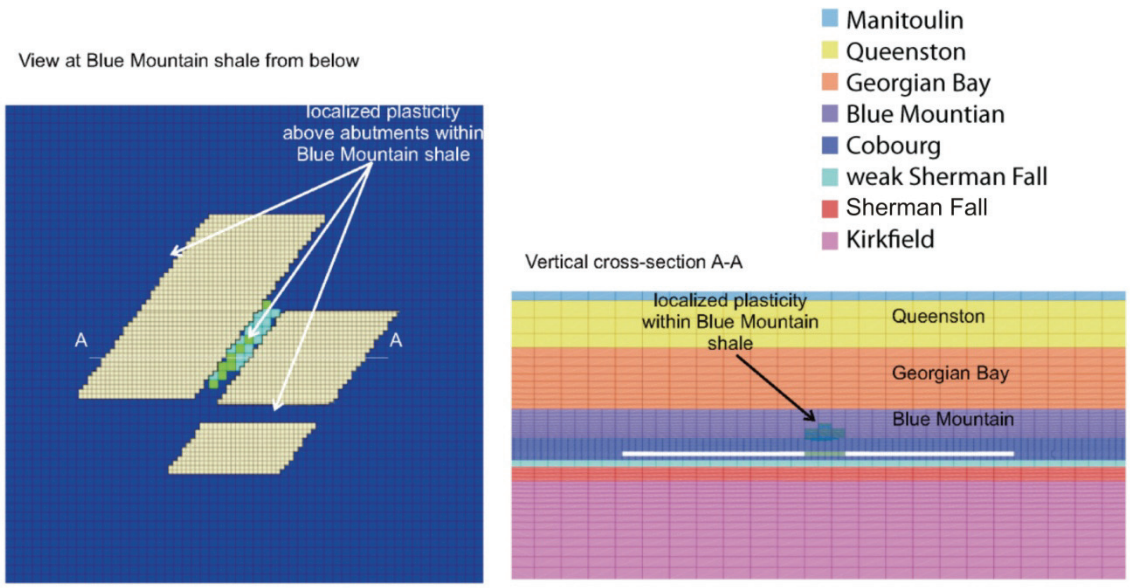

Figure 6.17: Plastic Deformation at the Peak of the Glacial Load: Case 1, 40 m Wide Barrier Pillar

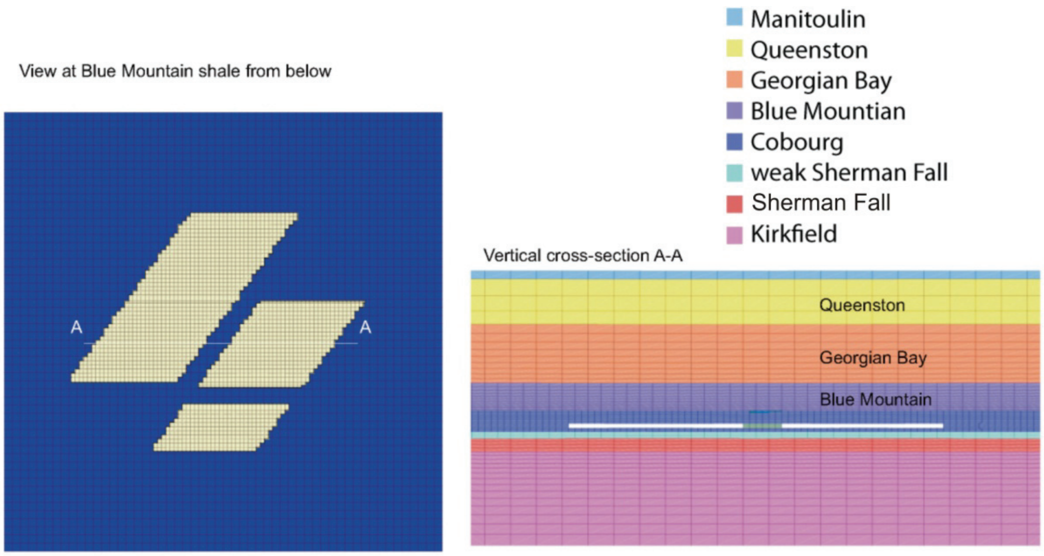

Figure 6.18: Plastic Deformation at the Peak of the Glacial Load: Case 2, 40 m Wide Barrier Pillar

6.3 Summary and Discussion

The two-dimensional pillar- and panel-scale analyses predict that for the considered material properties, geometry and loading combinations, the caverns are expected to collapse completely after three to seven glacial events, if the long-term strength is 45 MPa (approximately 40% of the short-term laboratory UCS). Even for this case, both the extent of damage and the caved region around the caverns are contained completely within the Cobourg limestone. When the long-term strength is increased to 72 MPa (65% of the short-term laboratory uniaxial strength) the pillars and caverns are stable throughout the 1 Ma time scale, because the model does not show increase in plasticity as a result of additional glacial events.

The limitations of the two-dimensional pillar-scale analyses, and the effect of potential collapse of the pillars throughout the panel on damage (yielding) in the shales overlying the Cobourg limestone, were evaluated in the three-dimensional panel-scale model. The prediction of yielding in the Blue Mountain shale in the panel-scale models was found to be sensitive to the Poisson’s ratio and horizontal in situ stress ratio in the Blue Mountain shale. The results of the analyses carried out for a range of those parameters indicate that no or very limited yielding of the Blue Mountain is anticipated above the abutments or the barrier pillars of the repository panels.

7. SHAFT ANALYSIS

A series of geomechanical numerical modelling analyses were conducted to evaluate the long-term performance of the backfill/seal design for the shafts at the proposed DGR. Prior to sealing, the shafts will be over-excavated to remove any obviously overstressed and fractured portions of the excavation damage zone (EDZ), and backfilled from the bottom up. The backfill/seal system will consist of a series of sections of compacted sand/bentonite mixture, concrete bulkheads and asphalt waterstop seals. The primary purpose of the over-excavation and backfill/seal system is to inhibit gas/fluid migration along the shaft, particularly within the region of excavation-induced damaged rock around the shaft boundary.

This chapter documents the results of the three-dimensional continuum analyses of the shaft long-term performance conducted using FLAC3D Version 3.10.474 32-bit (ITASCA 2005) for specific seal locations. The primary focus of this study is to evaluate the effect of the long-term processes on the development and evolution of the damaged zone around the shaft at the backfill/seal locations. The mechanical stress analyses included time-dependent strength degradation, glacial loading, seismic loading and gas/water pore pressure evolution over a period of 1 Ma. A total of 31 FLAC3D analyses have been carried out.

The geomechanical simulation results are based on the analysis of the seal system for the access shaft as presented in the Preliminary Safety Report (OPG 2011). A total of six seals were studied, consisting of an asphalt column and concrete bulkheads with different surrounding host rocks. The following sections cover the rock mass response in varied rock formations, specific seal behaviour (i.e., asphalt, concrete bulkhead), in situ stress environment, and pore pressure response around excavated openings. The asphalt column (S1) and the concrete bulkhead (B1) are shaft seal components (Figure 7.2) currently adopted in the Preliminary Safety Report (OPG 2011).

7.1 Overview of Shaft Backfill/Seal Design

The repository design includes the concrete lined, 6.5 m diameter main shaft and the 5 m diameter ventilation shaft. The shaft excavation and construction sequence include: (1) sinking of the shaft and initial ground support and (2) final support using a cast-in-place concrete liner. The shafts will be supported by the permanent concrete liner during the operational period. Following the closure of the repository, it is planned that the shafts will be sealed over the full depth, from the repository to the ground surface.

A key consideration in the design for the shaft sealing system is the potential formation of damage zones during shaft sinking and operation. These damage zones develop as a result of shaft excavation or mechanical changes due to stress redistribution. Typically, rock permeability increases within the damage zones, which can have a potentially significant impact on the shaft seal design.

The primary focus of this study is to evaluate the effect of long-term processes on the evolution of the damaged zones around the shaft excavations. According to FRACTURE SYSTEMS (2011), the damaged region around an underground excavation can be divided into three regions.

- The Excavation disturbed Zone (EdZ) is a zone with hydromechanical and geochemical modifications, without major changes in flow and transport properties.

- The Excavation Damaged Zone (EDZ) is a zone with hydromechanical and geochemical modifications inducing significant changes in flow and transport properties. These changes can, for example, include one or more orders of magnitude increase in flow permeability.
- Highly Damaged Zone (HDZ), where macro-scale fracturing or spalling may occur. The effective permeability of this zone is dominated by the interconnected fracture system and may be significantly greater than the matrix permeability.

These zones should be treated as “envelopes” encompassing those regions in which material property changes may occur, but also potentially including regions of unaltered rock properties (just as unaltered rock lenses may occur within a fault damage zone). The definitions are illustrated in Figure 7.1.

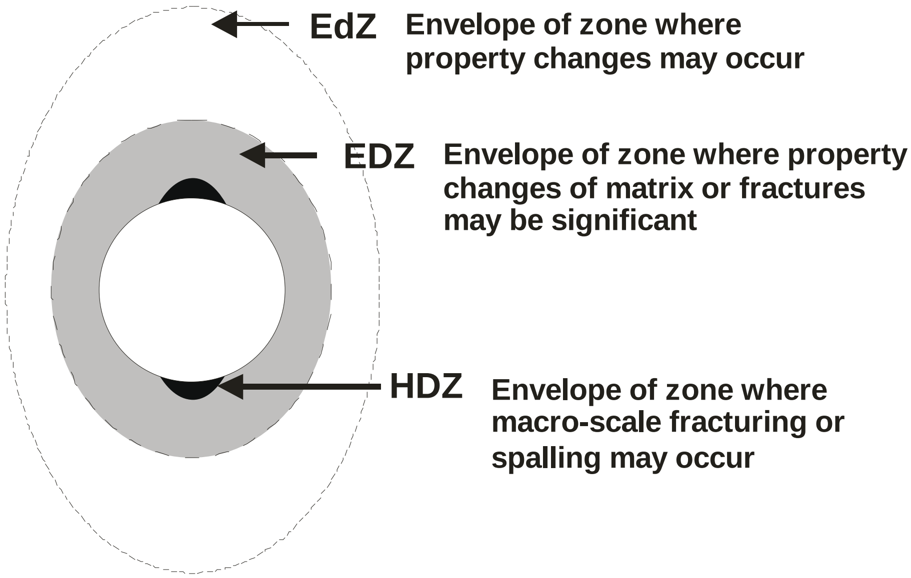

Note: For an unjointed rock in an anisotropic stress field with mechanical excavation (e.g., roadheader or TBM). Figure is from FRACTURE SYSTEMS (2011).

Figure 7.1: Schematic Illustrating Definitions of EdZ, EDZ and HDZ

During the sealing process, all infrastructure including shaft support structures and concrete liners will be removed, together with about 0.5 m of damaged rock, to ensure complete seal of the shaft column to the surrounding relatively low permeability rock. The backfill/seal construction sequence will be designed to minimize the extent of EDZ and HDZ formation around the final sealed excavation by over-excavating the HDZ around the shaft boundary in short rounds from the shaft bottom upward, while backfilling just below the over-excavation level. The removal of HDZ and shaft support structures will occur in small vertical lifts in a sequential manner, using mechanical means. Each section of removal will be followed closely by backfilling of the lift of densely compacted material. This will result in short, unsupported excavation rounds with confinement applied to the newly-excavated rock from the near-by backfill that will inhibit the formation/propagation of micro-cracks and fractures. In order to minimize the potential for groundwater flow though the EDZ, and along a preferential flow path between seal materials and the low permeability rocks, the concrete bulkheads will be keyed into surrounding rock beyond the edge of the prepared shaft and pressure grouted to intercept the portion of the EDZ. Martino et al. (2007) have shown that keying in the bulkheads is an effective means for minimizing the development of an EDZ.

Figure 7.2 shows the layout of the shaft seal arrangement. The shaft seal system consists of one asphalt column (S1), three concrete bulkheads (B1, B2, and B3) and four bentonite/sand backfill columns (OPG 2011). The three key concrete bulkheads are planned at critical horizons in the upper 4 m of the Salina unit A1, and in the Guelph Formation, which have higher permeabilities within the sedimentary sequence, and in the upper Salina unit F, below the near-surface shallow groundwater flow system. The over-excavation during repository closure includes the removal of the HDZ. Figure 7.3 illustrates currently proposed shaft seal geometries.

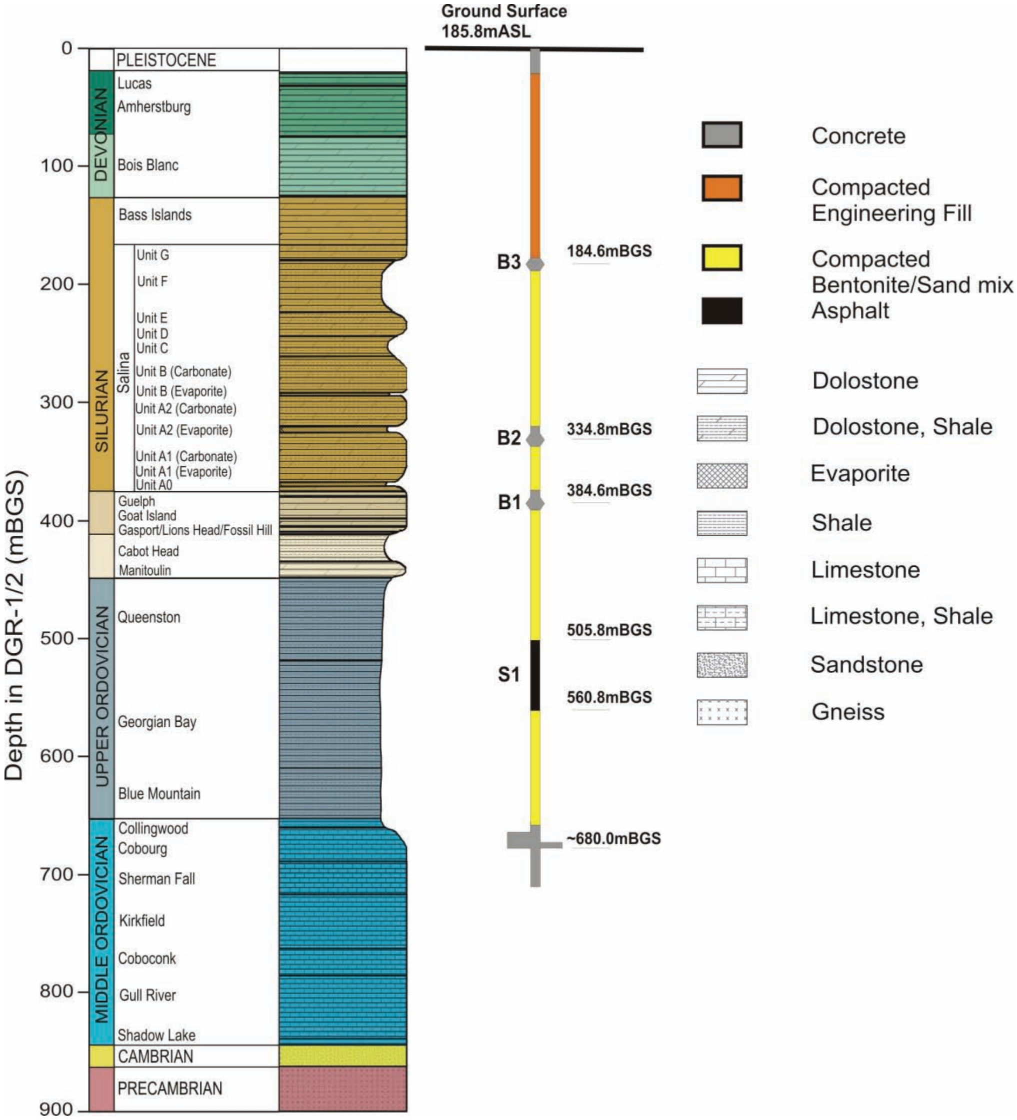

Note: Figure from OPG (2011)

Figure 7.2: Shaft Seal Arrangement for the DGR

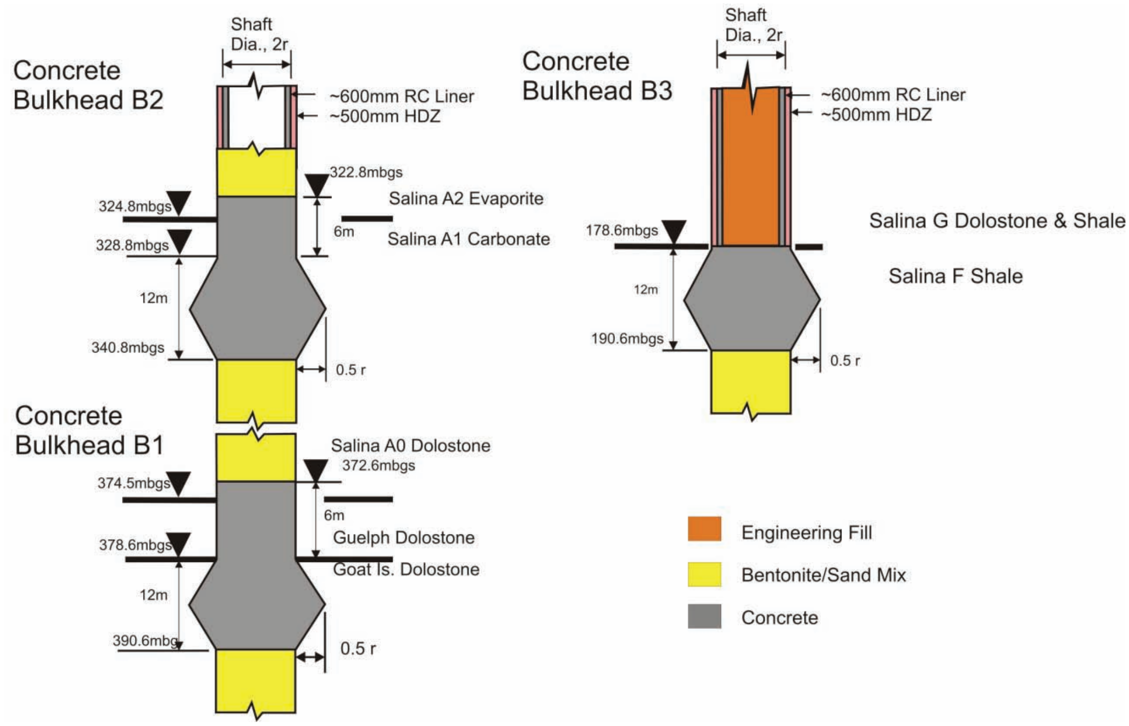

Note: Figure from OPG (2011)

Figure 7.3: Details of the Three Concrete Bulkheads Geometries

7.2 Description of Static Model

The various seal configurations have been modelled using the three-dimensional continuum numerical code FLAC3D. Seals B1 and S3 were analyzed for the combined effect of short-term mechanical behaviour, long-term strength degradation, glacial loading and gas/water pressure evolution. Seal B1 also is analyzed for seismic loading. Seal B1, the deepest concrete bulkhead, is analyzed for the following loading combinations: 1) long-term strength degradation, 2) long-term strength degradation and glacial loading, 3) long-term strength degradation, glacial loading and pore pressure, and 4) long-term strength degradation, glacial loading and seismic loading. In addition, four seals, one of which includes waterstop, were analyzed using models that accounted for short-term mechanical behaviour, long-term strength degradation and glacial loading. These concrete bulkheads are located within different surrounding host rocks. Thus, the study covers the rock mass response in varied rock formations, specific seal behaviour (i.e., waterstop, asphalt, concrete bulkhead), in situ stress environment and pore pressure response around excavated openings, beyond the current design.

7.2.1 Geometry and Model Generation

A quarter-symmetrical three-dimensional models of 80 m long shaft sections, 60 m × 60 m in plan, were created using FLAC3D. The models include the main shaft excavation, the over-excavation boundary and the seal arrangement built into the grid using actual design dimensions. A refined mesh region was included around the shaft to improve plasticity calculations near the shaft. Figure 7.4 show examples of the model geometries (grids) for seal B1, along with the seal/backfill sections and geological units.

A constant stress field was used within each geological unit in the individual models, with principal stresses based on in situ stresses for the DGR site, described in Section 4.1. Because the models of the individual shaft seal sections included only a relatively short vertical distance (80 m), a stress gradient was not included in the models.

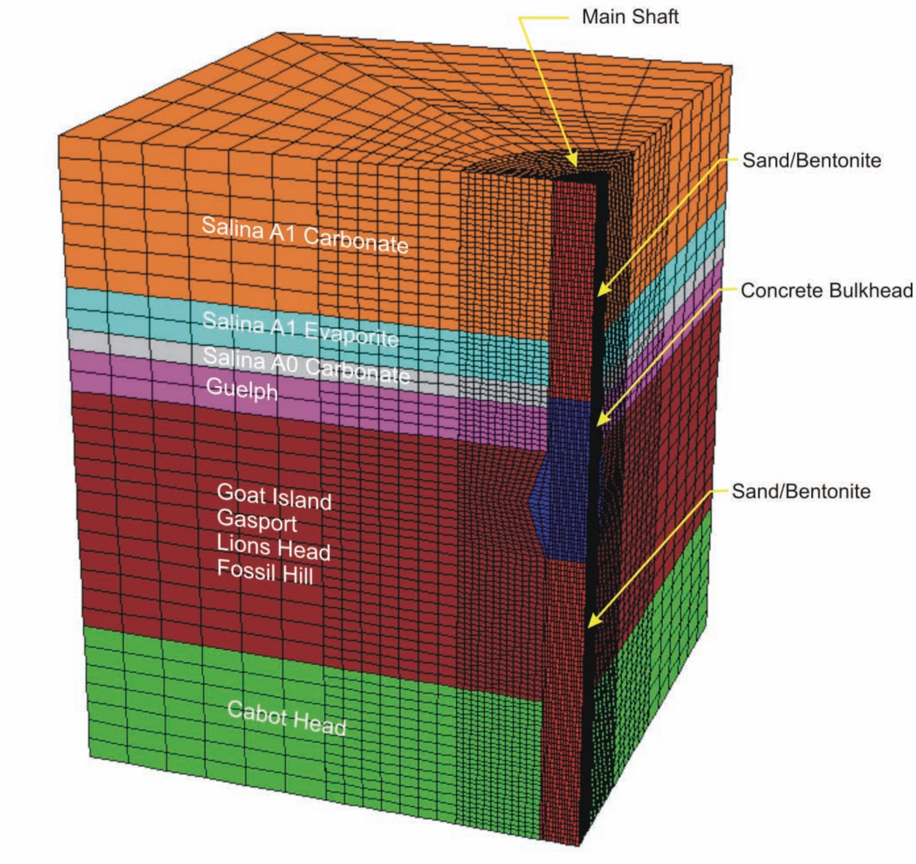

Figure 7.4: Layout of Quarter-symmetrical FLAC3D Model of Over-excavated and Backfilled Main Shaft for B1 Seal

7.2.2 Excavation Sequence

The initial shaft excavation, installation of ground support, over-excavation and shaft backfill/sealing sequence was simulated based on the excavation and backfilling sequence described by OPG (2011). The construction sequence consisted of the following steps.

- Initial excavation of shaft. Initial support was not considered. The final concrete liner was accounted for using the linear-elastic structural element logic in FLAC3D.
- Time-dependent degradation of the rock mass over the time period in which the repository is expected to be open (~100 years).
- Over-excavation of the damaged zone and backfilling with bentonite, including sequential advance of over-excavation and backfilling.
- Excavation of bulkhead regions, and replacement with concrete or asphalt, respectively.

- Time-dependent degradation of rock mass and concrete bulkhead properties for a period of 1 Ma. Model-specific long-term loading was included in this stage.

In the bottom and top portions of the models, away from the seals, the over-excavation and backfilling was done in relatively large vertical increments to increase modelling efficiency; in the vicinity of the seal, near the middle of the model, the over-excavation and backfilling was carried out in 3 m long rounds, as per design. The over-excavation for each seal (i.e., concrete bulkhead and asphalt waterstop) was carried out in one stage per seal and then backfilled in the following stage.

7.3 Description of Dynamic Model

The effect of seismic ground shaking was evaluated by incorporating ground motions directly into the model, using the dynamic option mode in FLAC3D. Three ground motions, corresponding to the seismic scenarios of: 1) M5.25 event at 10 km distance, 2) M6.25 at 25 km and 3) M7.4 at 100 km, all with 10^{-6} probability of annual exceedance, were used in the analysis. Time histories were derived for the elevation of the shaft seals (Section 4.5.1) and used in the analyses. The ground motions (two horizontal and one vertical) were applied to the model, with the horizontal component with greater PGV applied in the direction of the maximum in situ horizontal stress (σ_H). The ground motions are not consistent with the horizontal symmetry conditions assumed in the static models, therefore a full model of the shaft and seal were required for the dynamic analyses. Viscous and free-field boundary conditions were applied to the top/bottom and lateral boundaries of the model, respectively. The ground motions then were applied to the model as equivalent applied-stress boundary conditions. The analysis methodology is the same as described in Section 5.2.

7.4 Results

Based on the material properties, in situ stresses and loading conditions, all of the models indicated that the formation of an EDZ and EdZ can be anticipated around both the original shaft excavation and the over-excavated and backfilled shaft for all seal locations. The effect of specific loading conditions and load combinations are described in the following sections. For simplicity, this section will focus primarily on describing the results of the B1 seal model (deepest, with greatest stresses and pore pressures). However, the summary plot and table in Section 7.5 include the results from all simulated models. Also, the results for each analysed case, for each shaft seal and the loading case are provided in the appendices. The summary plots show yielded zones in the model, contours of the shear and the volumetric strains in the isometric view, but also in the horizontal cross-sections 22.4 m above the middle of the seal, in the middle of the seal and 22.4 m below the middle of the seal. The results are shown at the characteristic times, including: 1) time after shaft excavation, 2) 100 years (pre-closure), 3) 200 years (post-closure), 4) 100,000 years and 5) 1 Ma. All figures for seal B1 are in Appendix A; the figures for a concrete seal in Blue Mountain Formation are in Appendix B; the figures for seal S2 are in Appendix C; the figures for a concrete seal in Queenston and Manitoulin formations are in Appendix D; the figures for a waterstop seal in Saline A1 evaporate formation are in Appendix E; and, the figures for a concrete seal in Salina B and Salina C formations are in Appendix F.

7.4.1 Assessment of Damage Zones from Numerical Results

The difficulty of delineating envelopes for the HDZ, EDZ and EdZ based purely on numerical analysis results should be appreciated. The numerical models are set up with a material behaviour model (constitutive model) based on a yield criterion (e.g., Mohr-Coulomb) that can be used to evaluate the region where peak strength has been exceeded. This criterion cannot be used to predict changes in permeability within the rock mass directly. The relation between rock-mass yielding/failure and permeability is a complex issue, and the task of correlating these envelopes based on the results of geomechanics continuum-based stress analysis is challenging, and may not be achievable with suitable accuracy. Back-analysis of excavations under similar geotechnical conditions would be needed to refine our understanding of the evolution of these various damage regions. However, there are several modelling-output parameters that can be used as indicators of damage and permeability change. The following discussion is one possible interpretation of the correlation between results of analysis of stress change, and deformation around the shafts and resulting permeability change. The detailed results are provided in Appendices A through F to allow delineation of damage zones using different interpretations.

Rock mass damage due to exceeding the peak strength criterion is anticipated to result in an increase in permeability; therefore, as a starting point, the assumption can be made that the extent of the EDZ correlates with the extent of model-predicted yielded region. After exceeding the peak strength, micro-cracks that develop at lower stress levels coalesce and connect forming the flow paths that will result in change in rock mass permeability of one order of magnitude or more (FRACTURE SYSTEMS 2011).

Differentiation of the EdZ (based on the definition provided in Section 7.1) within the “elastic”, unyielded zone and the HDZ within the EDZ is speculative without corroborating field data. Theoretically, hydromechanical changes due to shaft excavation extend from the excavated shaft to infinity. Thus, it is necessary to define change thresholds to determine the outside boundary of the EdZ. The extent of the EdZ is not crucial for assessment of the shaft performance, and therefore it is not important to determine the outside boundary of the EdZ.

The HDZ is a part of the EDZ where rock mass undergoes large strains as a result of macro-scale fracturing or spalling. Typically, the HDZ will be along the excavation boundary, where confinement is small or does not exist. Although the extent of the HDZ can be determined based on the strain predictions, it is not obvious what strain thresholds define the HDZ. That strain limit is rock-dependent and should be determined from case-histories. In any case, there will be a large uncertainty in predictions of the HDZ using the continuum numerical models, because the HDZ must be determined based on large deformations which are sensitive to a choice of a constitutive model and parameters that characterize post-peak, softening behaviour, which are typically not well characterized. Furthermore, the HDZ corresponds to the regions of very large strains resulting from the opening of the fractures and/or spalling, which are modes of deformation that are not adequately represented by continuum models, because the rock ceases to behave as a continuum. Although no attempt has been made in this report to predict the extent of the HDZ based on the model predictions, the shear and volumetric strains that might be necessary for delineation of the HDZ are included.

Practically, prediction of the HDZ is not essential for assessment of the shaft and repository performance. The HDZ will be removed from the shaft wall during backfilling and is not expected to redevelop during post-closure after the shaft is backfilled. The models do not show significant increase in strains after backfilling.

7.4.2 Time-Dependent Strength Degradation Analysis

The results for seal B1 for time-dependent strength degradation are summarized in Figure 7.5 through Figure 7.7, showing plots of yielded zones, contours of shear strain and contours of volumetric strain, respectively. Concrete degradation is assumed in all simulations. The analyses for concrete seal have shown that the effect of concrete degradation on model predictions is relatively small. Although the repository certainly will be subjected to multiple glacial cycles during 1 Ma, it is of interest to look at the effect of time-dependent strength degradation independently, to be able to understand the importance of different loading conditions.

The results show that yielding is slightly more pronounced in the sequence that includes the Salina A1 evaporite and Salina A0 dolostone, where the maximum depth of failure[3] is approximately 3.27 m at the end of simulation, after 1 Ma, compared to ~2.4 m depth of failure in Salina A1 carbonate and Guelph dolostone. (The depths of failure for all units are summarized in Table 7.1 in Section 7.5.) The reason is a very small UCS of 20 MPa assumed for the Salina A1 evaporite, and relatively small thickness of the strong Salina A0 dolostone sandwiched between the relatively weak Salina A1 evaporite and Guelph dolostone. The largest yielded zone of 4.87 m is at the bottom of the model in the Cabot Head shale, which has the UCS of 12.6 MPa. The results indicate increase in the damage zone during first 200 years. Subsequently, the changes in the yielded zone are relatively small. Due to stress anisotropy, where σ_x is the maximum principal stress, the depth of the yielded zone is greater in the y-direction of the model around the shaft.

The contours of shear and volumetric strains, shown in Figure 7.6 and Figure 7.7, show that, if the threshold strains for the HDZ are assumed to be as low as 0.5%, the HDZ will develop primarily in the lower section of the shaft included in the model, in the relatively weak Cabot Head shale. In the calculation, overexcavation of the HDZ was simulated by removing predefined thickness according to the design specification (see Figure 7.3), irrespective of the model predictions. Thus, the entire regions with large strains in the Cabot Head shale predicted at the end of the pre-closure period were not removed. The results show that model does not predict significant increase in strains between 100 years and 1 Ma. Consequently, if the entire HDZ is removed during backfilling, it likely will not redevelop during the post-closure period.

7.4.3 Glacial Loading Analysis

A single glacial loading cycle, with variation in both vertical and horizontal stress components, was simulated for all seal models to evaluate its effects on the extent of yielding. The transient loading was applied to the model boundaries, along with the effects of time-dependent strength degradation. As shown in Figure 7.8, glacial loading induced very little change in the extent of yielding around the shaft near seal B1. Similar results were observed for all other modelled seals. This increase in loading due to a glacial event resulted in minimal additional yielding (compared to the effect of time-dependent strength degradation only) because glacial loading occurred after backfilling, when the rock mass around the shaft was confined completely. Although multiple glacial events will take place during 1 Ma, because the effect of a single glacial event on the yielding around the shaft is essentially negligible, additional events were not analyzed.

---

[3] Typically, the depth of failure varies over the thickness of the units, because of the effect of the adjacent units that might have different material properties (i.e., stiffness and strength). If not explicitly stated otherwise, the depth of failure for the given unit is the maximum depth of failure.

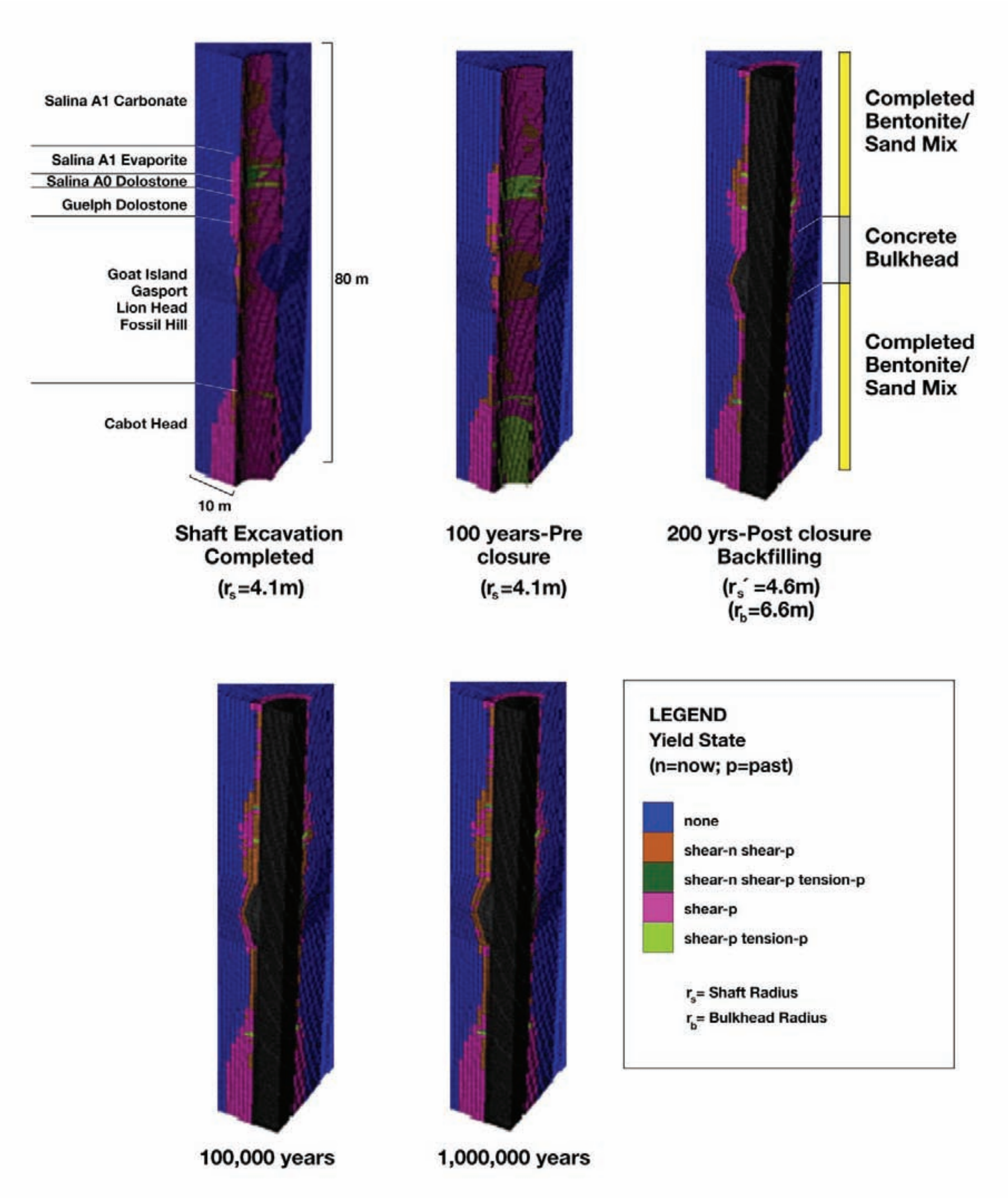

Figure 7.5: Yielding Observed Around Concrete Bulkhead B1: Time-dependent Strength Degradation

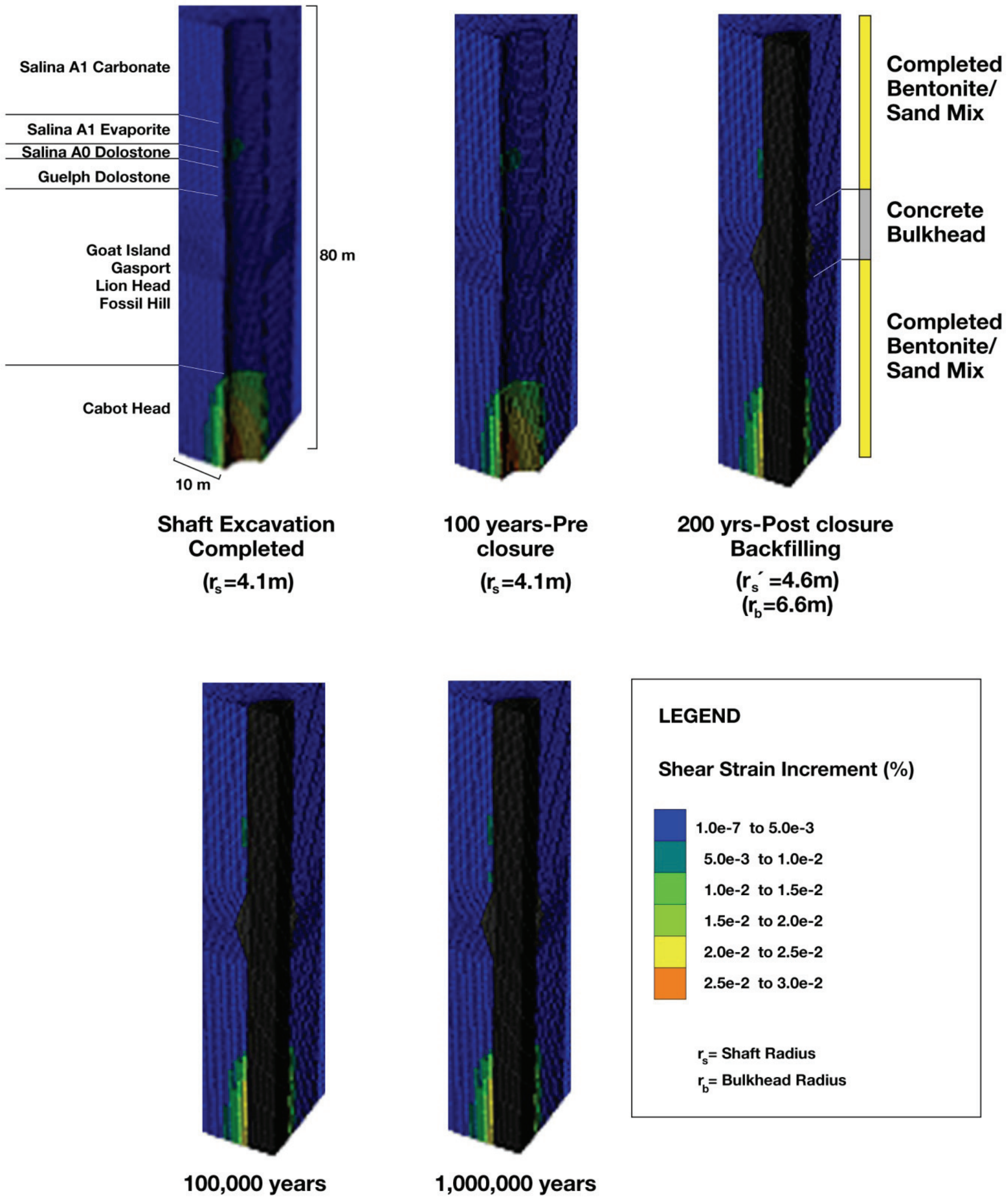

Figure 7.6: Shear Strain Observed Around Concrete Bulkhead B1: Time-dependent Strength Degradation

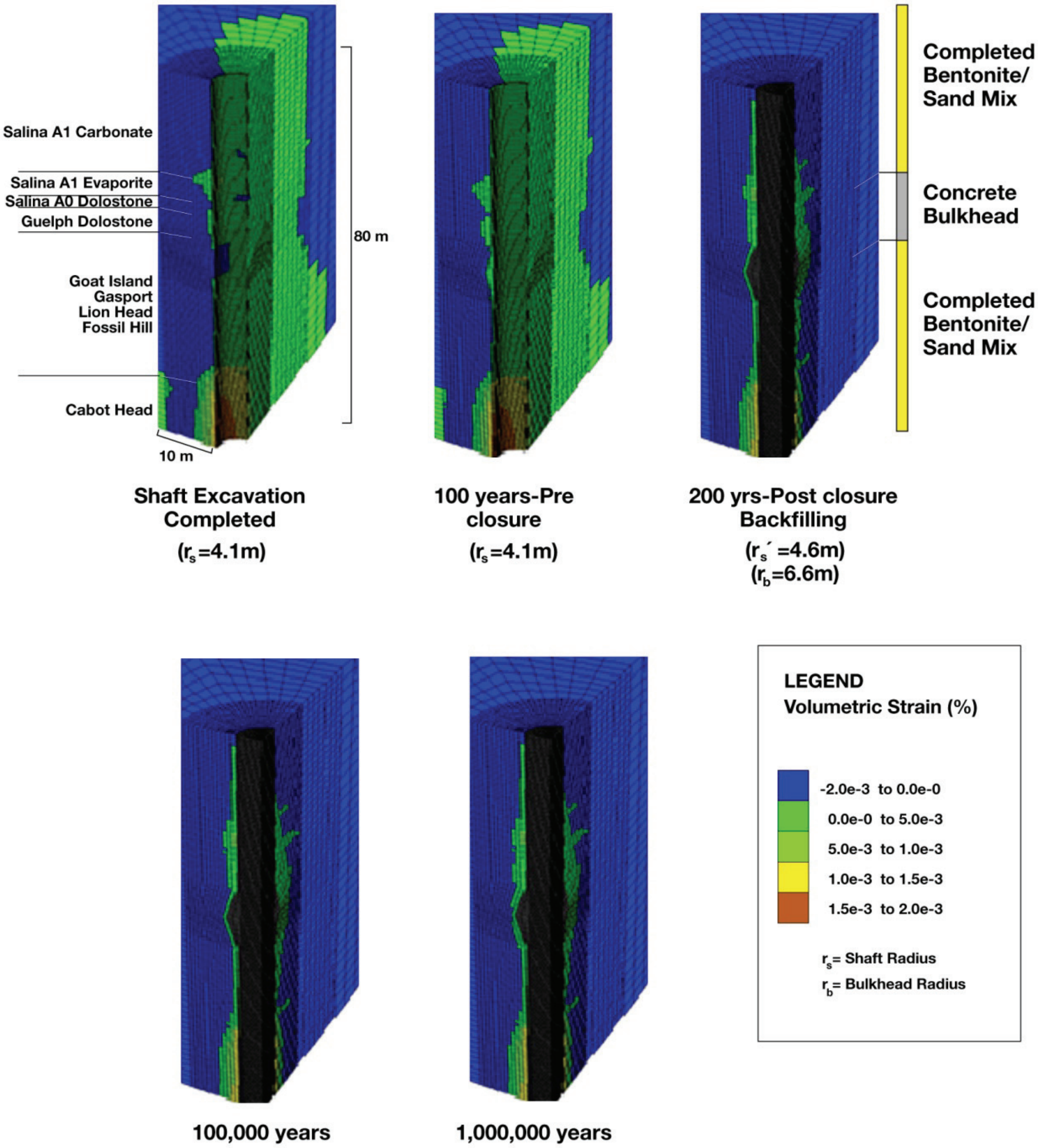

Figure 7.7: Volumetric Strain Observed Around Concrete Bulkhead B1: Time-dependent Strength Degradation

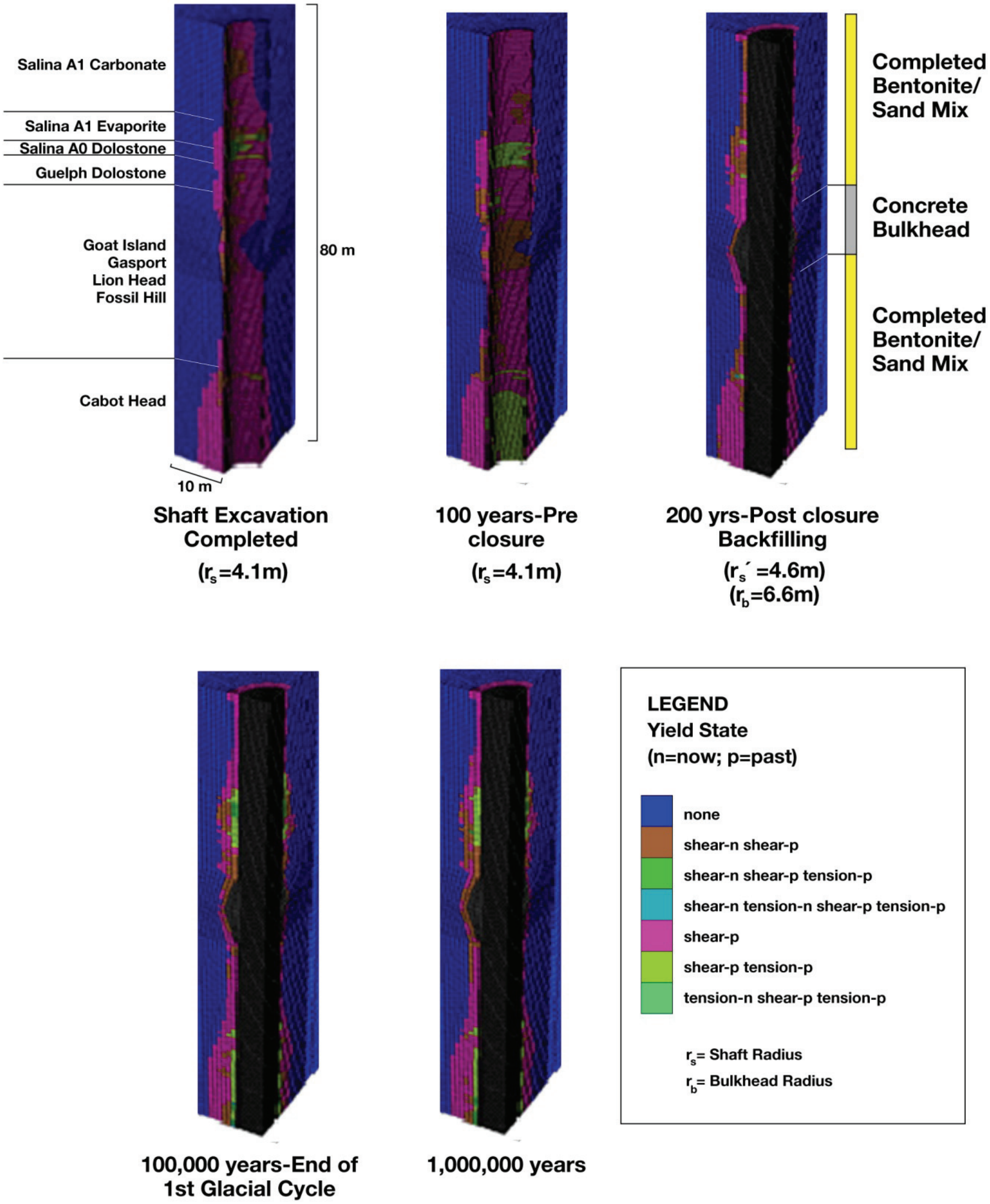

Figure 7.8: Yielding Observed Around Concrete Bulkhead B: The Time-dependent Strength Degradation + Glacial Load

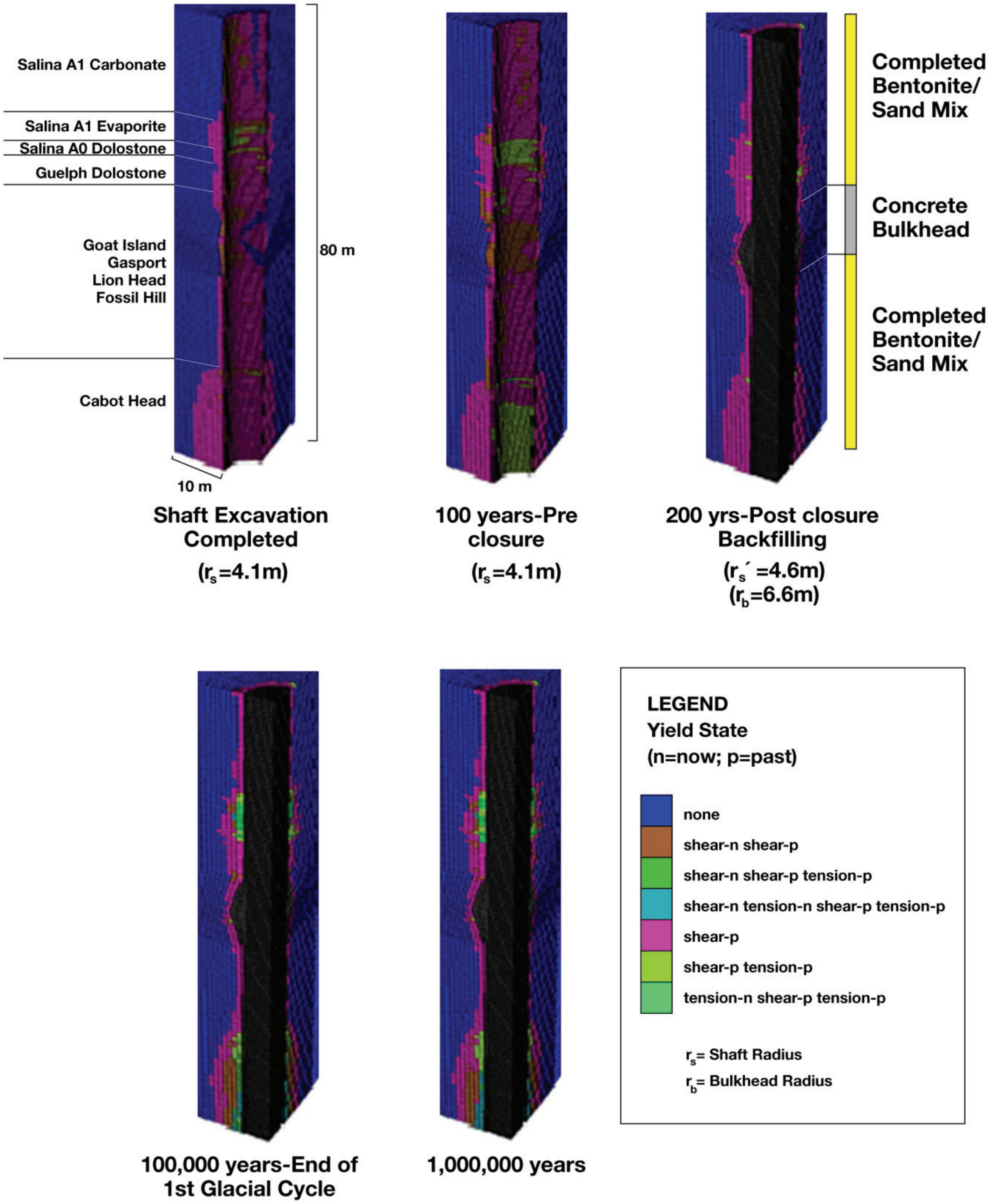

Figure 7.9: Yield State – Concrete Bulkhead B1: Time-dependent Strength Degradation + Glacial Load + Pore Pressure

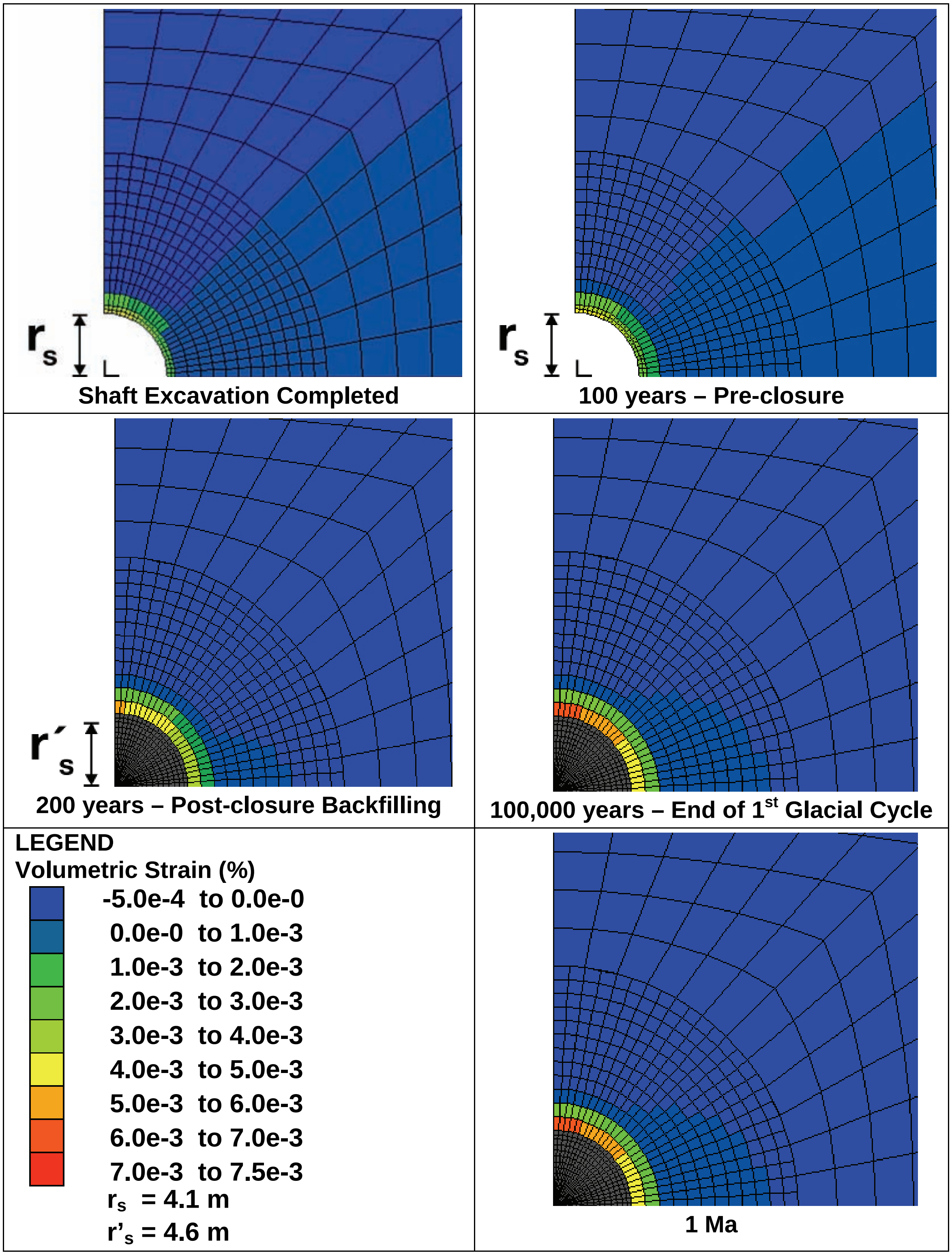

Shaft Excavation Completed

100 years – Pre-closure

200 years – Post-closure Backfilling

100,000 years – End of 1st Glacial Cycle

1 Ma

Figure 7.10: Volumetric Strain – 22.4 m Below Concrete Bulkhead B1: Time-dependent Strength Degradation + Glacial Load + Pore Pressure

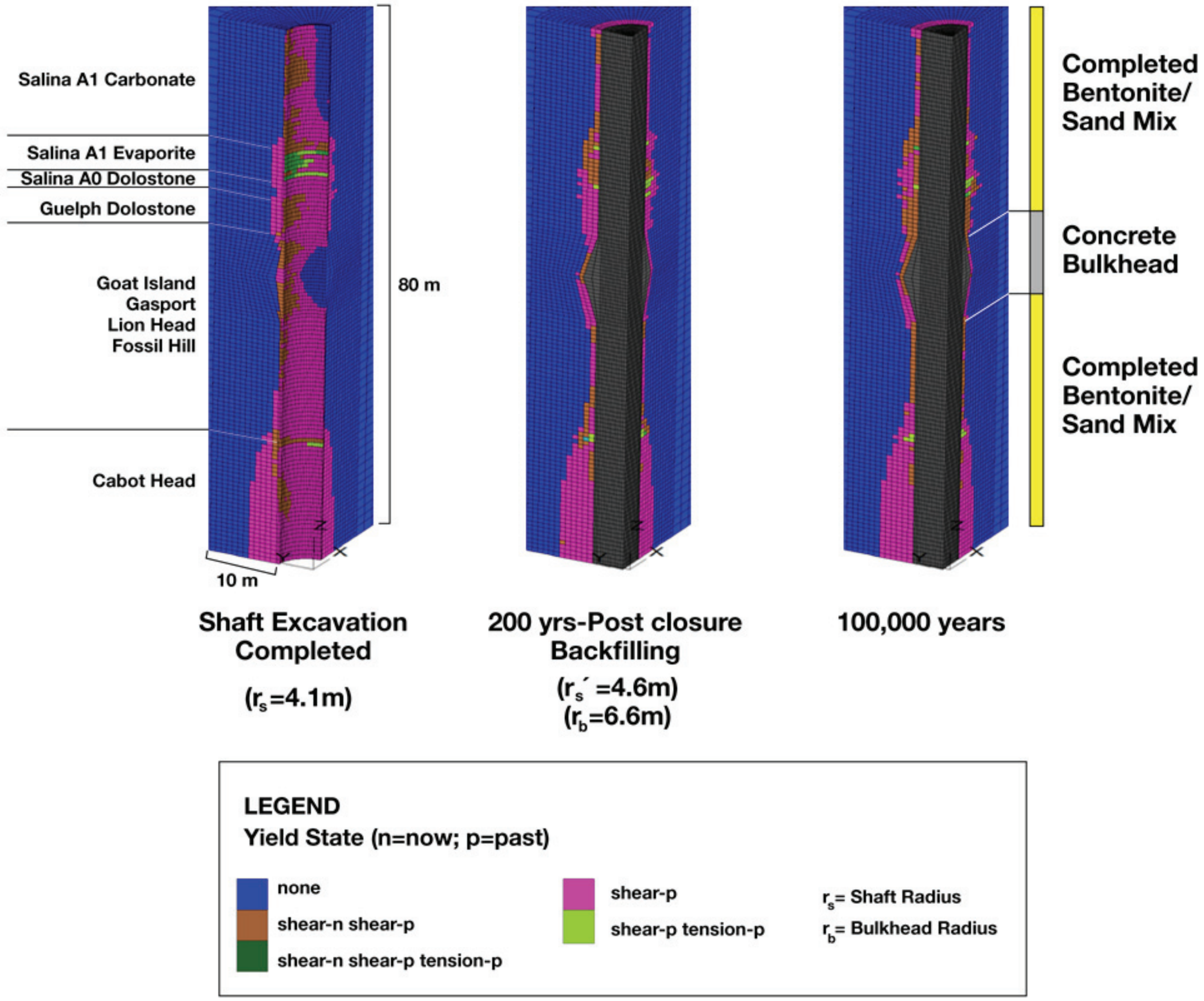

Figure 7.11: Yielded Zones Around the Shaft (Seal B1) Before and After Seismic Ground Motions Were Applied

Table 7.1: Predicted Depth of Damage Around Shaft Seals

Formation/ Unit	**Seal**	**Thick (m)**	σ_{xx} **(MPa)**	σ_{yy} **(MPa)**	$\sigma_{\max}$ [1] **(MPa)**	***UCS*** **(MPa)**	a[2] **(m)**	d_f **(m)**	$\frac{\sigma_{\max}}{UCS}$	$\frac{d_f}{a}$	**Loads Modelled**[3]
Salina C	Concrete Bulkhead	14	18.7	14.8	41.3	35	6.07	4.14	1.18	0.68	**TD_Cd**
			28.7	24.8	61.3		6.06	4.15	1.75	0.68	**TD_Cd_GL**
Salina A1 (Carbonate)	B1	41	20	16	44	116.7	4.58	2.43	0.38	0.53	**TD_Cd**
			30	26	64		4.58	3.28	0.55	0.72	**TD_Cd_GL**
			30	26	64		4.58	3.28	0.55	0.72	**TD_Cd_GL_PP**
			30	26	64		4.57	2.45	0.55	0.54	**TD_Cd_GL_DY**
	Waterstop		30	26	64		6.56	3.26	0.55	0.50	**TD_Cd**
			30	26	64		6.56	3.23	0.55	0.49	**TD_Cd_GL**
Salina A1 (Evaporite)	B1	4	20.1	16.1	44.2	20	4.58	3.27	2.21	0.71	**TD_Cd**
			30.1	26.1	64.2		4.58	3.27	3.21	0.71	**TD_Cd_GL**
			30.1	26.1	64.2		4.58	3.23	3.21	0.71	**TD_Cd_GL_PP**
			30.1	26.1	64.2		4.55	3.32	3.21	0.73	**TD_Cd_GL_DY**
	Waterstop		30.1	26.1	64.2		6.13	3.38	3.21	0.55	**TD_Cd**
			30.1	26.1	64.2		6.13	3.38	3.21	0.55	**TD_Cd_GL**
Salina A0	B1	4	20.2	16.2	44.4	197.6	4.58	3.27	0.22	0.71	**TD_Cd**
			30.2	26.2	64.4		4.58	3.27	0.33	0.71	**TD_Cd_GL**
			30.2	26.2	64.4		4.58	4.04	0.33	0.88	**TD_Cd_GL_PP**
			30.2	26.2	64.4		4.59	3.25	0.33	0.71	**TD_Cd_GL_DY**
	Waterstop		30.2	26.2	64.4		6.78	3.78	0.33	0.56	**TD_Cd**
			30.2	26.2	64.4		6.78	3.72	0.33	0.55	**TD_Cd_GL**
Guelph	B1	5	32.7	26.5	71.6	60.4	4.58	2.44	1.19	0.53	**TD_Cd**
			42.7	36.5	91.6		4.58	2.5	1.52	0.55	**TD_Cd_GL**
			42.7	36.5	91.6		4.58	2.46	1.52	0.54	**TD_CD_GL_PP**
			42.7	36.5	91.6		4.59	2.42	1.52	0.53	**TD_Cd_GL_DY**
	Waterstop		42.7	36.5	91.6		6.12	6.1	1.52	1.00	**TD_Cd**
			42.7	36.5	91.6		6.12	6.11	1.52	1.00	**TD_Cd_GL**
Goat Island Gasport Lions Head Fossil Hill	B1	31	33	26.5	72.5	148.3	4.58	1.68	0.49	0.37	**TD_Cd**
			43	36.5	92.5		4.58	1.62	0.62	0.35	**TD_Cd_GL**
			43	36.5	92.5		4.58	1.63	0.62	0.36	**TD_Cd_GL_PP**
			43	36.5	92.5		4.57	3.26	0.62	0.71	**TD_Cd_GL_DY**
Cabot Head	B1	24	14	12	30	12.6	4.58	4.87	2.38	1.06	**TD_Cd**
			24	22	50		4.58	4.87	3.97	1.06	**TD_Cd_GL**
			24	22	50		4.58	5.72	3.97	1.25	**TD_Cd_GL_PP**
			24	22	50		4.47	4.95	3.97	1.11	**TD_Cd_GL_DY**

Formation/ Unit	Seal	Thick (m)	σ_{xx} (MPa)	σ_{yy} (MPa)	σ_{max}[1] (MPa)	***UCS*** (MPa)	a[2] (m)	d_f (m)	$\frac{\sigma_{max}}{UCS}$	$\frac{d_f}{a}$	Loads Modelled[3]
Manitoulin	Concrete Bulkhead	11	14.3	11.8	31.1	70.7	6.8	2.5	0.44	0.37	**TD_Cd**
			24.3	21.8	51.1		6.8	2.5	0.72	0.37	**TD_Cd_GL**
Queenston	Concrete Bulkhead	73	15.2	12.7	32.9	48	6.11	2.74	0.69	0.45	**TD_Cd**
			25.2	22.7	52.9		6.1	2.73	1.10	0.45	**TD_Cd_GL**
	S1		15.2	12.7	32.9		6.13	2.03	0.69	0.33	**TD_Cd**
			25.2	22.7	52.9		6.12	2.04	1.10	0.33	**TD_Cd_GL**
			25.2	22.7	52.9		6.11	3.42	1.10	0.56	**TD_Cd_GL_PP**
Georgian Bay	S1	89	16.1	13.6	34.7	40.8	6.12	2.72	0.85	0.44	**TD_Cd**
			26.1	23.6	54.7		6.11	2.74	1.34	0.45	**TD_Cd_GL**
			26.1	23.6	54.7		6.12	2.73	1.34	0.45	**TD_Cd_GL_PP**
Blue Mountain	Concrete Bulkhead	44	11	10	23	21.7	6.08	4.12	1.06	0.68	**TD_Cd**
			21	20	43		6.06	4.16	1.98	0.69	**TD_Cd_GL**
			21	20	43		6.04	4.15	1.98	0.69	**TD_Cd_GL_PP**
			21	20	43		6.06	4.16	1.98	0.69	**TD_Cd_GL_DY**

Notes: Maximum depth of damage/EDZ (d_f) in each unit is reported. This is not always typical of plane strain depth of yielding for given unit properties.

1 σ_{max} is elastically calculated maximum tangential stress around a circular opening.

2 a is the radius of the excavation at the location of the measured depth of the EDZ (d_f), not the initial shaft radius.

3 Loading abbreviations: time dependent strength degradation (TD), concrete degradation (Cd), glacial loading (GL), pore pressure (PP), seismic (DY).

7.4.4 Pore Pressure Analysis

The long-term pore pressure effects on deformation and damage around the shaft were modelled in FLAC3D, along with the combined effect of time-dependent strength degradation and glacial loading. This case represents combination of all loads practically, because the analysis described in Section 7.4.5 indicates that the effect of seismic loading is negligible, and hence, was not included in the load combination. Because pore pressures and in situ stresses are greatest at depth, seal B1 was considered the most critical and was selected for the effective stress analysis. In addition to seal B1, effective stress analyses also were carried out for seals S2 and a concrete seal in Blue Mountain shale. The analyses were carried out with the base case pore pressures obtained from the analysis using numerical code T2GGM, as described in Section 4.3.3 and shown in Figure 4.7.

FLAC3D models showing the extent and modes of plastic yielding for seal B1 at various times are shown in Figure 7.9. The depth of failure due to combined loading varies significantly along the shaft (similarly as for the other load combinations), mostly due to variable rock mass strength. It can be seen by comparing Figures 7.5 and 7.9 that the pore pressure has relatively little effect on the extent of yielding for seal B1 throughout the 1 Ma. For combined loading, the largest yielded region is 5.72 m deep in the relatively weak Cabot Head shale. The increase in depth of failure due to long-term effect of pore pressure also varies along the shaft, with maximum increase of approximately 1.4 m or 40%.

The contours of volumetric strain, for combined loading including the pore pressure, in the horizontal cross-section 22.4 m below the middle of the shaft in the Lions Head unit, is shown in Figure 7.10.

7.4.5 Seismic Ground Motion Analysis

A FLAC3D dynamic analysis of the effect of seismic ground motion was carried out for seal B1 with a full-scale model (i.e., no lateral symmetries). The lateral symmetries could not be used for this load, because of two horizontal ground motions. The model was run with time-dependent strength degradation and glacial loading until 67,200 years — at which time the maximum load for the first full glacial cycle has been reached. At this state, the model was the subject to three 10^{-6} seismic event ground motions (AMEC GEOMETRIX 2011). As shown in Figure 7.11, seismic loading had no effect on the extent of failure for seal B1.

7.5 Summary and Discussion

The depths of failure (yielding) after 1 Ma for different loading conditions are provided in Table 7.1 and Figure 7.12. The table provides information on the horizontal in situ stresses, the maximum elastic stress concentrations in the shaft wall, the UCS, the maximum stress scaled to the strength, the maximum depth of failure and the depth of failure scaled to the radius for all of the units included in the numerical model, and for all considered loading conditions. The data are summarized by the geological units and by the shaft seals. Figure 7.12 shows a relative depth of failure, scaled to the shaft radius as a function of the maximum wall-stress concentrations scaled with unit strength. The figure includes only the results for the units where unit thickness is equal to or greater than the shaft diameter. The cases in which the yielding depth in relatively thin units is affected by the adjacent units are not shown in the figure, because they would affect the general trend. (An example is the Salina A0 dolostone, which is a thin and relatively strong unit sandwiched between two weak units, resulting, as can be seen from Table 7.1, in greater damage zone than could be expected based on the general trend as a function of in situ stresses and strength.) Because the maximum depths of failure are reported, the data in the figure still include the effect of interaction of the adjacent units in the cases when the maximum depth of failure occurs near the boundaries.

The table and the figure indicate that the depth of failure exceeds (by maximum of 25%) the shaft radius only in the case of the relatively weak Cabot Head shale. Otherwise, the maximum depth of failure is typically in the range of 60% to 70% of the radius (at the location, not the original shaft radius).

The results shown in Section 7.4.2 and Appendices A through F indicate that time-dependent strength degradation has an effect on the extent of predicted yielding. After 100 years, the extent of the yielded zones increases in size by 25% to 50% compared to that of the short-term condition. By comparing the condition at 200 years (100 years after over-excavation of the EDZ) and 1 Ma, it appears that most of the time-dependent yielding occurs over the initial 200-year period.

Within the accuracy of the model and discretization resolution around the shaft, the glacial loading has no effect on depth of failure. The glacial loading increases both vertical and horizontal far-field stresses, but the increase in the vertical stresses is much greater. The shaft is aligned with the vertical principal stress and is relatively insensitive to its changes. In addition, glacially induced stresses occur when the shaft is backfilled and rock mass around the shaft confined, making the damage zone around the shaft also insensitive to the glacially induced horizontal stress changes. In any case, most of damage around the shaft develops during pre-closure, while the shaft still is not backfilled.

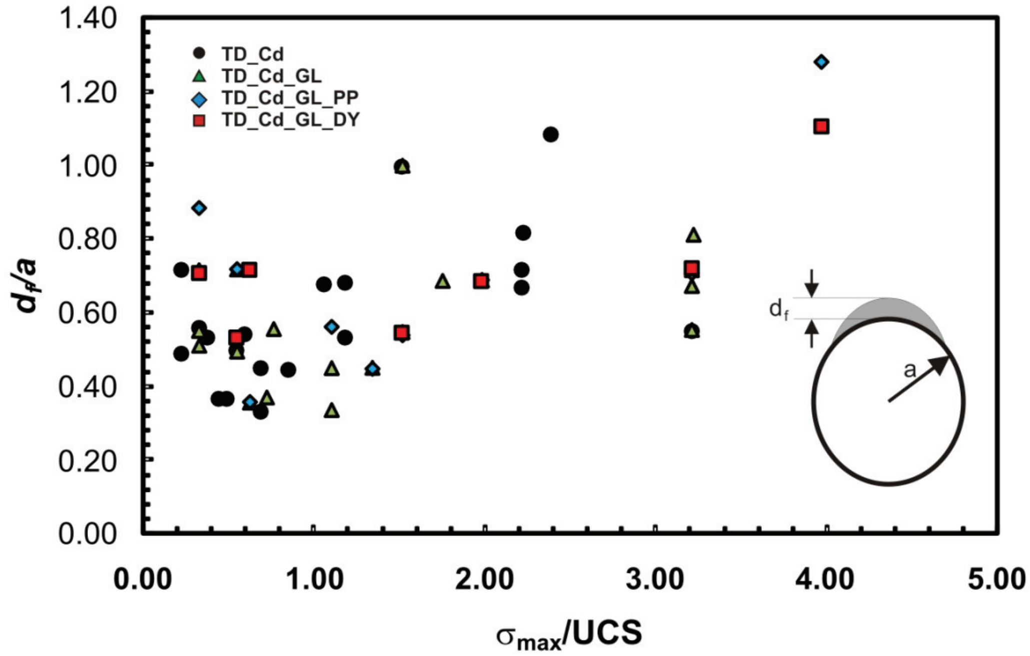

Notes: Units with thickness less than one diameter are excluded from the table. Maximum depth of yielding in each unit is reported. This is not always typical of plane-strain depth of yielding for a given unit properties. Loading abbreviations: time dependent strength degradation (TD), concrete degradation (Cd), glacial loading (GL), pore pressure (PP), dynamic loading (DY). $\sigma_{\max}$ is elastically calculated maximum tangential stress around a circular opening. Refer to Table 7.1 for loading abbreviations.

Figure 7.12: Relative Depth of Damage (Scale with Shaft Radius) Predicted by FLAC3D

In most of the units and for most of the shaft seals, the pore pressure does not have significant effect of depth of failure. The most pronounced effect can be observed in the relatively weak Cabot Head and the Queenston shales, where the pore pressure causes increase in the depth of failure to less than 1.4 m.

Seismic shaking has negligible effect on damage of rock mass around the shafts.

The shaft seals B2 and B3 from the current design were not analyzed in the numerical models. However, the depth of failure and strains around those two bulkheads certainly will be less than those predicted in the comparable units around seal B1. Seal B2 is located in the Salina A1 carbonate (Figure 7.3), which also appears in the model for seal B1. Considering the overburden depth for seal B2, the relative depth of damage, d_f / a, in the Salina A1 carbonate at the location of seal B2 is expected to be less than 0.72. It is reasonable to assume that the depth of failure roughly scales with excavation radius, particularly in the thicker units where plane-strain conditions apply and the radius provides the length scale. Using the same argument and the results for the Salina A1 evaporite from the seal B1 analysis, the relative depth of failure in the Saline A2 evaporite will be less than 0.71. Considering the relatively shallow overburden for seal B3, the depth of failure around seal B3 will not exceed the shaft radius.

In general, most of the failure occurred during initial excavation and over-excavation for all models. For most of the seals analyzed, the time-dependent strength degradation resulted in a significant increase in the extent of yielding. The additional time-dependent loading conditions had limited effect on evolution of the damaged zone around the shaft/seals, because of the stabilizing influence of confining pressure provided by the backfill-seal materials. Specifically, observations for the analysis indicated the following.

- The depth of damage exceeds (by maximum of 28%) the shaft radius only in the case of the relatively weak Cabot Head shale. Otherwise, the maximum depth of damage is typically in the range of 60% to 70% of the radius (at the location, not the original shaft radius).
- The time-dependent strength degradation resulted in a 25% to 50% increase in the extent of damage around the shaft seals, and resulted in increased damage in the failed zone as interpreted by the reduction in cohesive strength with time.
- The addition of glacial loading combined with strength degradation had only minimal effect on the extent of damaged rock.
- Effective stress analyses indicated that long-term pore pressure evolution (combined with strength degradation and glacial loading) could increase the extent of yielding by at most 1.4 m.
- Seismic ground motions had a negligible effect on the extent of damage.

The long-term evolution of the EDZ, as defined by FRACTURE SYSTEMS (2011) in terms of change in rock mass permeability, was correlated preliminarily to failure of the rock mass according to the peak strength criterion. Based on these criteria and the assumed loading conditions, the model-predicted extent of the EDZ is estimated to increase by approximately 25% to 50% over 1 Ma reaching the maximum depth typically in the range of 60% to 70% of the radius. It should be emphasized that the FLAC3D analyses cannot predict changes in rock mass permeability directly, and hence these numerical results can be used as indirect evidence of permeability changes only.

8. CONCLUSIONS

For long-term stability the quality of the rock mass containing the DGR must remain adequate such that the functionality of the DGR is not compromised. Numerical analyses with conservative assumptions have been used to assess the potential changes to the rock mass surrounding the repository. The evolution of the Excavation Damage Zone (EDZ) is investigated around the emplacement caverns and the shafts. Also, the effect of potential degradation of the caverns and the pillars between the caverns on stability of the panels and the cap shales is investigated. The analyses were carried out considering in situ stresses, time-dependent strength degradation, gas and pore pressures, glacial loading and seismic shaking. Several other conservative assumptions were used. The main objective of the analyses was to assess how the long-term deformation and damage of the rock mass, where the emplacement caverns and the shafts are located, will affect containment of gases and fluids.

The Voronoi block model was used to simulate the micro-cracking and time-dependent behaviour of the rocks and potential degradation and unravelling of rock around the emplacement caverns, considering the strength degradation in combination with the influence of gas pressure, seismic and glacial loading. Independent continuum studies were used to investigate the sensitivity of the predictions to assumption about the long-term rock strength. The effect of potential pillar collapse after multiple glacial cycles on stability of the cap shales is analyzed in the 3D continuum model. The shaft stability and damage were analyzed for different long-term loading conditions for critical shaft seals. The long-term stability analysis undertaken in the present study provides an overall assessment of the effects of the considered loading scenarios in 1,000,000 year time frame. The conclusions drawn from the analyses are summarized below.

a) Caverns:

- Time-dependent strength degradation under in situ stress conditions and assuming a long-term strength of 31.5 MPa (28% UCS) and deleting all loose blocks results in approximately 2 m of damage in the cavern wall and 6 m breakout from the cavern roof. If the long-term strength is assumed to be 45 MPa (40% UCS), no breakouts are predicted with yielding along the bedding planes in the roof and the floor limited to a depth of approximately 2 m.
- Gas and pore pressure variations within the caverns do not have significant effect on damage around the caverns or the breakout depth. The preferential direction for potential hydraulic fracturing is horizontal, along the bedding planes, perpendicular to the vertical minor principal stress. Under the assumption of doubling the predicted gas generating rate (to 15 MPa), bedding-parallel fractures may propagate up to 5 m beyond the cavern walls. However, the gas pressures, in all analyzed cases, will not generate hydraulic fractures that can result in gas release into the biosphere.
- Multiple glacial events and associated loading/unloading cycles are expected to cause failure of the pillars between the caverns and cavern collapse eventually. The number of glacial cycles that will cause pillar collapse and the timing of the pillar collapse depend on the long-term strength of the Cobourg limestone. Even using a conservative assessment for the Cobourg limestone long-term strength of 45 MPa, the caverns will stay open for at least 100,000 years. For a realistic assumption of the long-term strength of the Cobourg limestone using 72 MPa (65% UCS), the pillars and the caverns are expected to remain stable even after 1 Ma.
- Under the assumption of the lower bound long term strength (45 MPa), rubble that accumulates inside the caverns as a result of collapses during multiple loading/unloading cycles will eventually arrest further propagation of the caved region due to volume increase.

A steady state is reached when glacial cycles cause no further expansion of the damaged or caved regions. Importantly, the models predict that the steady state is reached prior to propagation of the caving related damage into the Blue Mountain shale, the lowest unit of the shale cap rock. Therefore, all damage remains contained within the Cobourg Formation under all loading conditions.

- The 3D panel-scale analysis shows that deformation of the cap rock due to potential complete pillar collapse, when assuming a lower-bound long-term strength of 45 MPa (40% UCS) for the Cobourg Limestone, will cause no or insignificant damage in the cap shales including the Blue Mountain shale. Thus, the repository-induced damage remains contained within the Cobourg limestone under all loading conditions.
- The analyses show that the effect of the six seismic scenarios on cavern stability, three for each the 10^{-6} and 10^{-5} probabilities of annual exceedance, is relatively small. The seismic ground shaking causes some additional unravelling of already fractured rock mass, but no new damage is predicted irrespective of the probability level of the seismic events.

b) Shafts:

- The shafts will be backfilled at the end of the operational period. Consequently, the long-term shaft stability will not be an issue. Instead, the focus of the shaft analysis is the evolution of the EDZ around the shafts. The depth of damage (HDZ and EDZ) for all load combinations after 1 Ma exceeds (by maximum of 28%) the shaft radius only in the case of the very weak Cabot Head Formation. Otherwise, the maximum depth of damage is typically in the range of 60% to 70% of the shaft radius or less.
- Time-dependent strength degradation typically causes an increase of 25% to 50% in the damage zone around the shaft seals.
- Effective stresses analyses indicated that long-term pore pressure evolution (combined with strength degradation and glacial loading) could increase the extent of damage locally by at most 40% in Seal B1.
- Seismic shaking and glacial loading are practically inconsequential for the EDZ and performance of the shafts.

In summary, the single most important parameter used in the numerical analyses is the long-term strength of the rock mass. Several model iterations are used to bound the range of possible outcomes, because one cannot measure the rock mass strength around a cavern over 1 Ma directly. As mentioned above, if the projected long-term rock strength is 65% UCS, a value commonly used for brittle materials, there is essentially no damage to the DGR and to the overlying shale cap rocks regardless of the loading conditions. If a more conservative estimate of 40% UCS is employed for long-term rock strength (i.e., the onset of cracking in brittle materials), the DGR caverns will collapse after approximately 100,000 years. In all cases, the overlying shale cap rocks will remain intact regardless of the imposed loading conditions. The EDZ along the shafts, with potential increased permeability, is predicted to be typically 70% or less of the shaft radius along almost the entire shaft length.

9. REFERENCES

Adams, J. and J.S. Bell. 1991. Crustal stresses in Canada. In: Neotectonics of North America. Slemmons, D.B., E. R. Engdahl, M. D. Zoback and D. D. Blackwell (Eds.). Geological Society of America, Decade Map Volume 1, 367-386.

Akgun, H., M.K. Kockar and O. Akturk. 2006. Evaluation of a compacted bentonite/sand seal for underground waste repository isolation. Environmental Geology 50, 331-337.

AMEC GEOMATRIX. 2011. Seismic Hazard Assessment. AMEC Geomatrix, Inc. report for the Nuclear Waste Management Organization NWMO DGR-TR-2011-20 R000. Toronto, Canada.

Arjang, B. 2001. Database on Canadian in situ ground stresses, Technical Note, Canada Centre for Mineral and Energy Technology – Mining and Mineral Sciences Laboratories. Division Report MMSL 01-029 (TR). Ottawa, Canada.

Barton, N. 2007. Rock Quality, Seismic Velocity, Attenuation and Anisotropy. Taylor and Francis. London, United Kingdom.

Bauer, S.J., D.E. Munson, M.P. Hardy, J. Barrix and B. McGunegle. 2005. In situ measurements and their implications in a deep Ohio mine. In: Chen, G. et al. (Eds.). Alaska Rocks 2005 — Rock Mechanics for Energy, Mineral and Infrastructure Development in the Northern Regions. Paper ARMA/USRMS 05-804. ARMA, University of Alaska-Fairbanks, USA.

Brady, B.H.G. and E.T. Brown. 2004. Rock Mechanics for Underground Mining. Kluwer Academic Publishers, Dordrecht/Boston/London.

BSC. 2004a. Drift Degradation Analysis. Yucca Mountain Project Report ANL-EBS-MD-000027 REV 03. Las Vegas,USA.

BSC. 2004b. Development of Earthquake Ground Motion Input for Preclosure Seismic Design and Postclosure Performance Assessment of a Geologic Repository at Yucca Mountain, NV. Yucca Mountain Project Report MDL-MGR-GS-000003 REV 01. Las Vegas, U.S.

Cartwright, P.B. 1997. A review of recent in situ stress measurements in United Kingdom coal measures strata. In Sugawara K, Y. Obara (Eds.). Proceedings International Symposium on Rock Stress, Kumamoto. A. A. Balkema, Rotterdam, Netherlands.

Clifton, J. R., J. M. Pommersheim and K. Snyder. 1995. Long-term Performance of Engineered Concrete Barriers. Building and Fire Research Laboratory, National Institute of Standards and Technology Technical Report NISTIR 5690. Gaithersburg, MD.

Cook, J. 1999. The effects of pore pressure on the mechanical and physical properties of shale. Oil and Gas Science Technology 54, 695-701.

Damjanac, B., M. Board, M. Lin, D. Kicker and J. Leem. 2007. Mechanical degradation of emplacement drifts at Yucca Mountain – A modeling case study. Part II: Lithophysal Rock. International Journal of Rock Mechanics and Mineral Science 44, 368-399.

Damjanac, B. and C. Fairhurst. 2010. Evidence for a long-term strength threshold in crystalline rock. Rock Mechanics and Rock Engineering 43(5), 1-19.

Detournay, E. and A.H.-D. Cheng. 1993. Fundamentals of poroelasticity. In: Hudson, J., E.T. Brown, C. Fairhurst and E. Hoek (Eds.). Comprehensive Rock Engineering 2.

Diederichs, M.S. 2007. The 2003 Canadian Geotechnical Colloquium: mechanistic interpretation and practical application of damage and spalling prediction criteria for deep tunnelling. Canadian Geotechnical Journal 44, 1082-1116.

FRACTURE SYSTEMS. 2011. Excavation Damaged Zones Assessment. Fracture Systems Ltd. report for the Nuclear Waste Management Organization NWMO DGR-TR-2011-21 R000. Toronto, Canada.

Gorski, B., T. Anderson and B. Conlon. 2009a. Laboratory Geomechanical Strength Testing of DGR-1 & DGR-2 Core. Intera Engineering Ltd. Report TR-07-03 Rev.3. CANMET Mining and Mineral Sciences Laboratories. Ottawa, Canada.

Gorski, B., T. Anderson and B. Conlon. 2009b. Long-Term Strength Degradation Testing of DGR-2 Core. Intera Engineering Ltd. Report TR-08-11 Rev.0. CANMET Mining and Mineral Sciences Laboratories. Ottawa, Canada.

Gorski, B., T. Anderson and B. Conlon. 2010a. Laboratory Geomechanical Strength Testing of DGR-3 & DGR-4 Core. Intera Engineering Ltd. Report TR-08-24 Rev.1. CANMET Mining and Mineral Sciences Laboratories. Ottawa, Canada.

Gorski, B., T. Anderson and B. Conlon. 2010b. Long-Term Strength Degredation Testing of DGR-3 & DGR-4 Core. Intera Engineering Ltd. Report TR-08-36 Rev.1. CANMET Mining and Mineral Sciences Laboratories. Ottawa, Canada.

Gorski, B., T. Anderson and D. Rogers. 2010c. Supplementary Uniaxial Compressive Strength Testing of DGR-3 and DGR-4 Core. Intera Engineering Ltd. Report TR-08-39 Rev.1. CANMET Mining and Mineral Sciences Laboratories. Ottawa, Canada.

Hoek, E. and E.T. Brown. 1980. Underground Excavations in Rock. The Institution of Mining and Metallurgy, London, United Kingdom.

Hoek, E., C. Carranza-Torres and B. Corkum. 2002. Hoek-Brown Failure Criterion — 2002 Edition. In: Hammah, R. et al. (Eds.). Proceedings of NARMS-TAC 2002: Mining and Tunnelling Innovation and Opportunity 1, 267-273. University of Toronto Press, Toronto, Canada.

Hoek, E. and M.S. Diederichs. 2006. Empirical estimation of rock mass modulus. International Journal of Rock Mechanics and Mining Science 43, 203–215.

Huber, G.A. and D.S. Decker. 1995. Engineering Properties of Asphalt Mixtures and the Relationship to Their Performance. American Society for Testing and Materials Special Technical Publications 1265.

Wigston, A. and D. Heagle. 2009. Bedrock Formations in DGR-1, DGR-2, DGR-3 and DGR-4. Intera Engineering Ltd. Report TR-08-12 Rev.1. Ottawa, Canada.

INTERA. 2011. Descriptive Geosphere Site Model. Intera Engineering Ltd. report for the Nuclear Waste Management Organization NWMO DGR-TR-2011-24 R000. Toronto, Canada.

INTERA and QUINTESSA. 2011. Postclosure Safety Assessment: Gas Modelling. Intera Engineering Ltd. and Quintessa Ltd. report for the Nuclear Waste Management Organization NWMO DGR-TR-2011-31 R000. Toronto, Canada.

ITASCA. 1999. PFC2D (Particle Flow Code in 2 Dimensions) Version 2.0. Itasca Consulting Group Inc. Minneapolis, USA.

ITASCA. 2005. FLAC3D (Fast Lagrangian Analysis of Continua in 3 Dimensions) Version 3.1. Itasca Consulting Group Inc. Minneapolis, USA.

ITASCA. 2006. Universal Distinct Element Code (UDEC) Version 4.00. Itasca Consulting Group Inc. Minneapolis, USA.

ITASCA. 2008. FLAC (Fast Lagrangian Analysis of Continua) Version 6.0. Itasca Consulting Group Inc. Minneapolis, USA.

ITASCA. 2009. FLAC3D (Fast Lagrangian Analysis of Continua in 3 Dimensions) Version 4.0. Itasca Consulting Group Inc. Minneapolis, USA.

Jaeger, J.C. and N.G.W. Cook. 1979. Fundamentals of Rock Mechanics. 3rd Edition. Chapman and Hall, New York, USA.

Kaiser, P.K., and S. Maloney. 2005. Review of Ground Stress Database for the Canadian Shield, Ontario Power Generation Report No. 06819-REP-01300-10107-R00.

Lau, J.S.O., B. Gorski, B. Conlon and T. Anderson. 2000. Long-term Loading Tests on Saturated Granite and Granodiorite. Ontario Power Generation Report 06819-REP-01300-10016 R00. Toronto, Canada.

Lewis, R.W. and B.A. Schrefler. 1998. The Finite Element Method in the Static and Dynamic Deformation and Consolidation of Porous Media. John Wiley and Sons, New York, USA.

Lund, B., P. Schmidt, and C. Hieronymus. 2009. Stress Evolution and Fault Stability During the Weichselian Glacial Cycle. SKB Technical Report TR-09-15. Svensk Kärnbränslehantering AB, Stockholm, Sweden.

Martin, C.D. 1997. Seventeenth Canadian Geotechnical Colloquium: The effect of cohesion loss and stress path on brittle rock strength. Canadian Geotechnical Journal 34, 698-725.

Martin, C.D., and N.A. Chandler. 1994. The progressive fracture of Lac du Bonnet Granite. International Journal of Rock Mechanics and Mining Science 31, 643-659.

Martin, C.D., P.K. Kaiser and D.R. McCreath. 1999. Hoek-Brown parameters for predicting the depth of brittle failure around tunnels. Canadian Geotechnical Journal 36, 136-151.

Martino, J.B., D.A. Dixon, E.T. Kozak, M. Gascoyne, B. Vignal, Y. Sugita, T. Fujita and K. Masumoto. 2007. The tunnel sealing experiment: An international study of full-scale seals. Physics and Chemistry of the Earth 32, 93-107

NWMO and AECOM Canada Ltd. 2011. Regional Geomechanics – Southern Ontario. Nuclear Waste Management Organization Report NWMO DGR-TR-2011-13 R000. Toronto, Canada.

OPG. 2011. Deep Geologic Repository for Low and Intermediate Level Waste – Preliminary Safety Report, Ontario Power Generation Report 00216-SR-01320-00001 R000. Toronto, Canada.

Peltier, W.R. 2011. Long-Term Climate Change. Nuclear Waste Management Organization Report NWMO DGR-TR-2011-14 R000. Toronto, Canada.

Pruess, K. 1991. TOUGH2 – A General Purpose Numerical Simulator for Multiphase Fluid and Heat Flow. Lawrence Berkely Laboratory LBL-29400.

QUINTESSA and INTERA. 2011. Postclosure Safety Assessment: Data. Quintessa Ltd. and Intera Engineering Ltd. report for the Nuclear Waste Management Organization NWMO DGR-TR-2011-32 R000. Toronto, Canada.

ROCSCIENCE. 2007. RocLab Version 1.031. Available at Rocscience Inc. www.rocscience.com.

Schmidtke, R.H. and E.Z. Lajtai. 1985. The long-term strength of Lac du Bonnet Granite. International Journal of Rock Mechanics and Mining Science 22, 461-465.

Souley, M., G. Armand, K. Su and Y. Wileveau. 2007. Modelling of the hydromechanical response of a shaft sinking in a deep claystone. In: 10th nternational Symposium of Numerical Models Geomechanics (NUMOG X), 25–27 April 2007. Rhodes, Greece.

Tepfers, R. and T. Kutti. 1979. Fatigue strength of plain, ordinary, and lightweight concrete. Proceedings American Concrete Institute Journal 76, 635–652.

Tsang, C.F., F. Bernier and C. Davies. 2005. Geohydromechanical processes in the excavation damaged zone in crystalline rock, rock salt, and indurated and plastic clays—in the context of radioactive waste disposal. International Journal of Rock Mechanics and Mining Science 42, 109-125.

Valley, B. and S. Maloney. 2010. Analyses of DGR-1 and DGR-2 Borehole Images for Stress Characterization TR-08-35. MIRARCO.

Vermeer, P.A. and R. de Borst 1984. Non-associated plasticity for soils, concrete and rock. Heron 29(3), 3-64.

10. ABBREVIATIONS, ACRONYMS AND UNITS

CI	Crack Initiation
CD	Crack Damage
σ_n	Confining Stress
DISL	Damage Initiation and Spalling Limit
DGR	Deep Geologic Repository
E	Elastic Modulus
EDZ	Excavation Damage Zone
EdZ	Excavation Disturbed Zone
GGM	Gas-Generation Model
GSI	Geological Strength Index
GPa	Giga Pascal
HDZ	Highly Damaged Zone
kPa	kilo Pascal
L&ILW	Low and Intermediate Level Waste
mBGS	metres Below Ground Surface
M	Earthquake Magnitude
MS	Mechanostratigraphic Unit
MPa	megapascal
Ma	million years
NWMO	Nuclear Waste Management Organization
OPG	Ontario Power Generation Inc.
PGAs	Peak Ground Accelerations
PGVs	Peak Ground Velocities
ν	Poisson’s Ratio
TBM	Tunnel Boring Machine
3D	three-dimensional
UCS	Unconfined Compressive Strength
UofT GSM	University of Toronto Glacial Systems Model

THIS PAGE HAS BEEN LEFT BLANK INTENTIONALLY

APPENDICES

THIS PAGE HAS BEEN LEFT BLANK INTENTIONALLY

APPENDIX A: FLAC3D RESULTS FOR BULKHEAD B1

APPENDIX B: SUPPLEMENTAL FLAC3D RESULTS FOR CONCRETE BULKHEAD IN BLUE MOUNTAIN SHALE

APPENDIX C: FLAC3D RESULTS FOR ASPHALT SEAL S2

APPENDIX D: SUPPLEMENTAL FLAC3D RESULTS FOR BULKHEAD IN QUEENSTON AND MANITOULIN FORMATIONS

APPENDIX E: SUPPLEMENTAL FLAC3D RESULTS FOR WATERSTOP BULKHEAD

APPENDIX F: SUPPLEMENTAL FLAC3D RESULTS FOR BULKHEAD IN SALINA C FORMATION

(Note: All appendices are provided on the enclosed CD.)